

RL-TR-97-51  
Final Technical Report  
July 1997



# ULTRA-HIGH SPEED OPTICAL COMMUNICATION AND SWITCHING VIA NOVEL QUANTUM DEVICES

Northwestern University

Sponsored by  
Advanced Research Projects Agency  
ARPA Order No. B510

19971007 237

*APPROVED FOR PUBLIC RELEASE; DISTRIBUTION UNLIMITED.*

*THIS COPY IS UNCLASSIFIED*

The views and conclusions contained in this document are those of the authors and should not be interpreted as necessarily representing the official policies, either expressed or implied, of the Advanced Research Projects Agency or the U.S. Government.

Rome Laboratory  
Air Force Materiel Command  
Rome, New York

This report has been reviewed by the Rome Laboratory Public Affairs Office (PA) and is releasable to the National Technical Information Service (NTIS). At NTIS it will be releasable to the general public, including foreign nations.

RL-TR-97-51 has been reviewed and is approved for publication.

APPROVED: *Robert L. Kaminski*

ROBERT L. KAMINSKI  
Project Engineer

FOR THE COMMANDER:

*John A. Graniere*

JOHN A. GRANIERO, Chief Scientist  
Command, Control & Communications Directorate

If your address has changed or if you wish to be removed from the Rome Laboratory mailing list, or if the addressee is no longer employed by your organization, please notify RL/C3BC, 525 Brooks Rd, Rome, NY 13441-4505. This will assist us in maintaining a current mailing list.

Do not return copies of this report unless contractual obligations or notices on a specific document require that it be returned.

ULTRA-HIGH SPEED OPTICAL COMMUNICATION AND SWITCHING VIA  
NOVEL QUANTUM DEVICES

Contractor: Northwestern University

Contract Number: F30602-94-1-0003

Effective Date of Contract: 12 July 1994

Contract Expiration Date: 31 August 1996

Short Title of Work: Ultra-High Speed Optical Communication and  
Switching via Novel Quantum Devices

Period of Work Covered: Jul 94 - Aug 96

Principal Investigator: Seng-Tiong Ho  
Phone: (708) 491-7103

RL Project Engineer: Robert L. Kaminski  
Phone: (315) 330-1886

Approved for public release; distribution unlimited.

This research was supported by the Advanced Research Projects  
Agency of the Department of Defense and was monitored by  
Robert L. Kaminski, Rome Laboratory/C3BC, 525 Brooks Road,  
Rome, NY 13441-4505.

REPORT DOCUMENTATION PAGE			Form Approved OMB No. 0704-0188
<p>Public reporting burden for this collection of information is estimated to average 1 hour per response, including the time for reviewing instructions, searching existing data sources, gathering and maintaining the data needed, and completing and reviewing the collection of information. Send comments regarding this burden estimate or any other aspect of this collection of information, including suggestions for reducing this burden, to Washington Headquarters Services, Directorate for Information Operations and Reports, 1215 Jefferson Davis Highway, Suite 1204, Arlington, VA 22202-4302, and to the Office of Management and Budget, Paperwork Reduction Project (0704-0188), Washington, DC 20503.</p>			
1. AGENCY USE ONLY (Leave blank)	2. REPORT DATE	3. REPORT TYPE AND DATES COVERED	
	July 1997	Final Jul 94 - Aug 96	
4. TITLE AND SUBTITLE		5. FUNDING NUMBERS	
ULTRA-HIGH SPEED OPTICAL COMMUNICATION AND SWITCHING VIA NOVEL QUANTUM DEVICES		C - F30602-94-1-0003 PE - 63226E PR - B510 TA - 00 WU - 01	
6. AUTHOR(S)		8. PERFORMING ORGANIZATION REPORT NUMBER	
Seng-Tiong Ho, Prem Kumar, and Horace P. Yuen		N/A	
7. PERFORMING ORGANIZATION NAME(S) AND ADDRESS(ES)		10. SPONSORING/MONITORING AGENCY REPORT NUMBER	
Department of Electrical and Computer Engineering Northwestern University 2145 Sheridan Road Evanston IL 60208		RL-TR-97-51	
9. SPONSORING/MONITORING AGENCY NAME(S) AND ADDRESS(ES)		11. SUPPLEMENTARY NOTES	
Advanced Research Projects Agency 3701 North Fairfax Drive Arlington VA 22203-1714		Rome Laboratory Project Engineer: Robert L. Kaminski/C3BC/(315) 330-1886	
Rome Laboratory/C3BC 525 Brooks Road Rome NY 13441-4505		12a. DISTRIBUTION AVAILABILITY STATEMENT	
		12b. DISTRIBUTION CODE	
		Approved for public release; distribution unlimited.	
13. ABSTRACT (Maximum 200 words)		<p>This project is a continuation of a joint theoretical-experimental research program which was undertaken to initiate the development of novel quantum devices for greatly improved optical communications and switching in both local network and long haul applications. In this final report we present the results obtained in the various efforts undertaken by each of the principal investigators. Specifically, we describe the demonstration of the first photonic-wire semiconductor laser and the lasers with directional light output and the investigation of novel microcavity semiconductor laser structure; we also present the results of our investigation on the implementation of nondegenerate parametric amplifier in fiber lines that support communication rates of ten's of gigabits per second, together with the results of our modeling and experimental efforts for our proposed long-term storage of soliton bit streams in fiber/PSA rings. We also present the progress on the theoretical investigation to determine the ultimate quantum limit on optical switching.</p>	
14. SUBJECT TERMS		15. NUMBER OF PAGES	
Optical Communication, Quantum Optics, Nonlinear Optics, Optical Switch, Semiconductor Lasers		104	
		16. PRICE CODE	
17. SECURITY CLASSIFICATION OF REPORT	18. SECURITY CLASSIFICATION OF THIS PAGE	19. SECURITY CLASSIFICATION OF ABSTRACT	20. LIMITATION OF ABSTRACT
UNCLASSIFIED	UNCLASSIFIED	UNCLASSIFIED	UL

# Ultra-High Speed Optical Communication and Switching via Novel Quantum Devices

## Final Report

July 12, 1994 – Aug. 31, 1996

*Seng-Tiong Ho, Horace P. Yuen, and Prem Kumar*

Department of Electrical and Computer Engineering

Northwestern University, Evanston, IL 60208-3118

Contact: Seng-Tiong Ho, [sth@eecs.nwu.edu](mailto:sth@eecs.nwu.edu)

Phone: (847) 491-7103; Fax: (847) 491-4455

## Abstract

This project is a continuation of a joint theoretical-experimental research program which was undertaken to initiate the development of novel quantum devices for greatly improved optical communications and switching in both local network and long haul applications. In this final report we present the results obtained in the various efforts undertaken by each of the principal investigators. Specifically, we describe the demonstration of the first photonic-wire semiconductor laser and the lasers with directional light output and the investigation of novel microcavity semiconductor laser structure; we also present the results of our investigation on the implementation of nondegenerate parametric amplifier in fiber lines that support communication rates of ten's of gigabits per second, together with the results of our modeling and experimental efforts for our proposed long-term storage of soliton bit streams in fiber/PSA rings. We also present the progress on the theoretical investigation to determine the ultimate quantum limit on optical switching.

# Contents

<b>1</b>	<b>Introduction</b>	<b>8</b>
<b>2</b>	<b>Proposed Goals and Summary of Research Performed</b>	<b>12</b>
2.A	Soliton Photon Number Amplifiers, Improved Ultrafast All-Optical Switches, and Novel Microcavity Lasers for Optical Communications . . . . .	12
2.A.1	The following was accomplished: . . . . .	12
2.B	Dispersion Compensation, Stable Soliton Propagation and Regeneration, and Pulse Shaping . . . . .	14
2.B.1	Dispersion Compensation Experiments . . . . .	14
2.B.2	Stable Soliton Propagation . . . . .	15
2.B.3	Soliton Regeneration . . . . .	16
2.B.4	Pulse Shaping with PSA's . . . . .	17
2.C	Analysis of Device and System Performance . . . . .	17
<b>3</b>	<b>Methods, Procedures, and Outcomes</b>	<b>18</b>
3.A	Soliton Photon Number Amplifiers, Improved Ultrafast All-Optical Switches, and Novel Microcavity Lasers for Optical Communications . . . . .	18
3.A.1	Demonstration of the first photonic-wire semiconductor laser . . . . .	18
3.A.2	Demonstration of the first directional light output from the microcavity semiconductor laser . . . . .	21
3.A.3	Investigation of novel microcavity semiconductor laser structure . . . . .	23
3.A.4	Characterization of Novel Microcavity Semiconductor Lasers . . . . .	28
3.A.5	Fabrication of Micro-Resonator Structure . . . . .	29
3.A.6	Degenerate Optical Parametric Amplification in $\chi^{(3)}$ Waveguide . . . . .	31
3.A.7	Development of a new method to measure third-order optical nonlinearities in waveguides . . . . .	37
3.B	Dispersion Compensation, Stable Soliton Propagation and Regeneration, and Pulse Shaping . . . . .	50
3.B.1	Dispersion Compensation Experiments . . . . .	50

3.B.2	Stable Soliton Propagation: Compensation of Soliton Self-Frequency Shift with PSA's . . . . .	51
3.B.3	Stable Soliton Propagation: Periodic Amplification and Conjugation of Solitons . . . . .	55
3.B.4	Long-Term Storage of a Soliton Bit Stream using PSA's: Effects of Soliton-Soliton Interactions and Quantum Noise . . . . .	59
3.B.5	Stable Soliton Propagation: Storage Experiments . . . . .	65
3.B.6	Soliton Regeneration . . . . .	72
3.B.7	Pulse Shaping with PSA's . . . . .	77
3.C	Analysis of Device and System Performance . . . . .	81
3.C.1	Analysis of Device and System Performace . . . . .	81
<b>4</b>	<b>Conclusions</b>	<b>83</b>
<b>5</b>	<b>References</b>	<b>84</b>
<b>6</b>	<b>List of Publications Resulting from this contract</b>	<b>90</b>
<b>7</b>	<b>List of Abbreviations</b>	<b>92</b>

# List of Figures

1	SEM image of a 4.5 diameter photonic-wire ring laser with $0.45\mu\text{m}$ waveguide. . . . .	19
2	Spectra of photonic wire ring lasers with $4.5\mu\text{m}$ diameter. The solid line and dash line were measured above (1.5 threshold) and near threshold, respectively. Inset shows the measured power as a function of peak pump power. . . . .	20
3	SEM images of the fabricated $10\mu\text{m}$ diameter photonic-wire laser with waveguide output coupling. . . . .	21
4	The infrared image of a $10\mu\text{m}$ micro-ring laser. The lasing whispering-gallery mode and the bright emitting spots at the ends of waveguide can be seen clearly. . . . .	22
5	Schematic diagram of a microcylinder laser coupled with output waveguide. . . . .	23
6	Spectra of a microcylinder laser with $10\mu\text{m}$ diameter. . . . .	24
7	Infra-red image showing the output of a microcylinder laser coupled with waveguide. . . . .	24
8	Schematic diagram of the suspended photonic-wire mirror and micro-cavity. Holes were etched in the photonic wire to from a one-dimensional photonic-bandgap structure. . . . .	25
9	(a) Calculated reflection spectrum of a $0.3\mu\text{m}$ photonic-wire mirror with six rectangle holes. (b) Calculated reflection spectrum of a $0.3\mu\text{m}$ photonic-wire cavity with six rectangle holes . . . . .	25
10	Geometry and field distribution in a $0.3\mu\text{m}$ photonic-wire microcavity. The cavity length is $0.775\mu\text{m}$ , and six ( $0.225 \times 0.1\mu\text{m}^2$ ) holes are on either side to from a Fabry-Perot cavity. . . . .	26
11	(a) SEM image of a micro-cavity before selective etching. (b) SEM image of a micro-cavity after selective etching . . . . .	27
12	Experimental setup of a microcavity semiconductor laser characterization. . . . .	28
13	Scanning Electron Microscope (SEM) image of a microcavity resonator with 5 micron diameter. . . . .	30
14	NMZI scheme for a $\chi^3$ -based degenerate OPA. . . . .	31
15	Novel pulse-delayed DOPA scheme. . . . .	32
16	Experimental setup to demonstrate the pulse-delay DOPA, using AlGaAs waveguide. . . . .	35
17	(a) Normalized output signal for the case when the pump is on and off: $I_p = 1.16\text{GW}/\text{cm}^2$ and $I_s = 0.35\text{GW}/\text{cm}^2$ ; (b) interference between pump and signal as a function of the pump-signal phase mismatch. . . . .	36
18	Normalized degenerate OPA gain of the input signal as function of pump intensity inside the AlGaAs waveguide. . . . .	37
19	Schematic of the balanced Mach-Zehnder interferometer, with Signal and LO pulse at frequency $w_s$ , and pump pulse at frequency $w_p$ . . . . .	38
20	Illustration of Interference between Signal and LO as displayed by an oscilloscope for the cases when: (a) the pump is on (long dash) and off (tiny dash), and (b) the pump is chopped at a rate faster than the PZT ramping. . . . .	39
21	Schematic of the experimental set up to measure $n^{(2)}$ and $\alpha^{(2)}$ for the case when the pump and Signal beams have the same polarization. . . . .	40
22	Nonlinear phase shift and nonlinear absorption data obtained in AlGaAs waveguide using this technique. The data is fitted with two sine envelopes for the cases where the pump is on (solid) and off (dashed). Measurement was made at an RF frequency of 200 kHz. . . . .	42

23	The upper trace show the interferometer output signal as function of time, while the lower trace indicates the PZT voltage as function of time. The arrows indicate the direction in which the interference signal shifts as the pump is turned on for the cases of positive and negative $n_{elec}^{(2)}$ . . . . .	45
24	Trace of the direct measurement of nonlinear absorption for the case when the pump and PSig have orthogonal polarizations. . . . .	46
25	Schematic of the experimental setup to perform four-wave mixing measurement. . . . .	47
26	(a)Optical frequency spectrum of the various beams involved in the four-wave mixing experiment, indicating the frequency shift of the LO, PSIG, and PConj signals with respect to the pump beam; (b) the expected RF beat spectrum in the FWM experiment, with the beating components indicated above each arrow. . . . .	48
27	RF beat signal spectrum resulting from the four-wave mixing experiment in AlGaAs waveguide using 430 fs pulses at $\lambda=1.6\mu\text{m}$ . . . . .	49
28	Block diagram of the stabilization system for the Nd:YLF laser. It differs from the Pound-Drever-Hall technique insofar as the light is transmitted through the reference cavity rather than reflected off of it. . . . .	51
29	Amplified error signal. The cavity was scanned at a rate of approximately 40 MHz/ms and the bipolar error signal created by one laser mode observed on an oscilloscope. The symmetry point corresponds to the cavity resonance. Horizontal: 0.2 ms/div; Vertical: 0.1 V/div. . . . .	52
30	Propagation of a 1 ps pulse, including the effects of higher-order dispersion, in a line with periodic (a) EDFA's and (b) PSA's. . . . .	54
31	The effect of the Raman self-frequency shift on a 1 ps pulse in a line with periodic (a) EDFA's and (b) PSA's. . . . .	54
32	Frequency shift induced on a 1 ps pulse with periodically spaced (a) EDFA's and (b) PSA's. . . . .	54
33	Propagation of a 0.5 ps pulse, including the effects of Raman scattering, in a lossless line with periodic phase-conjugating amplifiers showing the effect of (a) third-order dispersion and (b) nonlinear dispersion. . . . .	57
34	Propagation of a 0.5 ps pulse, including the effects of higher-order dispersion and Raman scattering, in a line with periodic phase-conjugating amplifiers. The third-order and nonlinear dispersion have been balanced so that $\beta_{nl} = 2\beta_3$ . (a) Lossless line. (b) Linear loss of 0.15 dB/km. . . . .	58
35	A physically realizable optical storage ring using a fiber PSA [69], WDM = wavelength dependent coupler. . . . .	61
36	Numerical solution of the two-soliton interaction for different amplifier configurations, showing the normalized position of one of the two solitons as a function of distance (measured in dispersion lengths). The results are given for PIA's, PSA's, PSA's + added lumped loss, and PSA's + lumped loss and gain modulation. The initial pulsedwidth was $\tau_0 = 2$ ps. For the PIA case the gain was chosen to exactly compensate the loss. For PSA's + added loss, the field was attenuated by $\exp(-0.5)$ before each amplifier. For PSA's + gain modulation, the same extra loss factor was used, but the gain was modulated sinusoidally (10 ps period, 10% modulation). The left (right) plot is for in-phase (out-of-phase) interaction. . . . .	62

37	Left — Graph showing the pulse timing-jitter variance as a function of distance (in units of dispersion lengths) obtained by numerically solving the NLS equation with lumped PSA's and with added noise. The timing variance has been scaled in the computations by the initial pulse width $\tau_0$ (here = 2 ps). Right — Graph showing the pulse photon-number variance as a function of distance (in units of dispersion lengths) obtained by numerically solving the NLS equation with either PIA's or PSA's. The photon-number variance is scaled in the computations by the reference photon number $n_0$ ( $= 4.2 \times 10^5$ ). . . . . .	63
38	Graph showing the saturation of the pulse photon-number variance with distance when GAWBS phase noise is included. The GAWBS noise parameter was taken from the published data of Shelby <i>et al.</i> [67] and the random phase fluctuation was introduced just before each amplification. . . . .	64
39	Plot of the input (dotted line) and output (solid line) in-phase quadrature for a single computational run of a 3.5 ps soliton bit stream at 100 Gb/s forming the eight-bit pattern '11101100' in a fiber storage ring. The input pulses have been purposely seeded with random variations in their soliton parameters to show the stability of one's and zero's, and the output stream is shown after approximately 3000 km of propagation. . . . .	65
40	Experimental configuration of a linear storage line using a PSA to compensate for the linear loss. The storage line plus the PSA fiber can store 32-bits at 29 MHz. . . . .	66
41	Autocorrelation traces of the input pump and signal pulses, the reflected pump pulse, and the output signal pulse from the fiber PSA. SPM induced pulse narrowing of the pump pulse (with no input signal pulse) during passage through the PSA fiber accounted for most of the pulse narrowing of the amplified signal pulse. Further narrowing of the signal pulse was a result of intensity dependent gain. . . . .	67
42	Experimental (symbols) and theoretical gain data (solid curves) plotted versus pump average power for four signal average powers. . . . .	69
43	Autocorrelation traces of the reflected pump pulses from the PSA with (dotted line) and without (dashed line) DOPO action. Note that the reflected pump narrowed to 1.1 ps from 1.5 ps when the DOPO was oscillating, due to depletion of the pump. The autocorrelation trace of the DOPO pulse (solid line) has the same width as the depleted pump pulse, as expected. . . . .	70
44	Output of the storage line. The top trace in (a) shows the input packet (loaded 8 times to ensure buildup in the storage line); the bottom trace shows storage for 128 round trips of the loaded packet. The trace in (b) shows a close-up view from 75 to 95 $\mu$ s of the data in (a). A single packet is noted. Trace (c) shows the photodiode response recovered by looking at 3 packets in (a). For comparison an 8 one/24 zero packet has been overlaid onto the photodiode response. Note that the evidence for the presence of bits matches well with the overlaid packets. . . . .	71
45	Photocurrent spectrum in the vicinity of the beat frequency that results when the laser output is direct detected with a fast photodetector. . . . .	74
46	Optical spectrum (Left) and autocorrelation trace (Right) of the dual-frequency Er/Yb glass laser. . . . .	75
47	Experimental setup. The phase modulator was driven at 100 MHz. . . . .	75
48	Comb-like DTF design showing the distance dependence of the dispersion and non-linear coefficients. The lengths of the DSF segments were 2, 1.2, and 0.4 km, respectively; and those of the STF segments were 0.6, 0.1, and 0.1 km, respectively. . . . .	77

49	Optical spectrum (Left) and autocorrelation trace (Right) of the pulse train at the output of the DTF. In (b), the dashed curve is a theoretical fit and the time scale on the abscissa is normalized to the pulse repetition period of 17.1 ps. Also in (b) the thin solid curve is the theoretical autocorrelation trace for a two-frequency laser source. . . . .	78
50	Pulse magnitude after one and two passes through the self-phase modulator and amplifier combination for an initial Gaussian profile. Here $\beta = 1.836$ and $G = 5.0$ . . . . .	79
51	Pulse phase after one and two passes through the self-phase modulator and amplifier combination. Parameters are as in Fig. 1. . . . .	80

# 1 Introduction

Long-haul fiber optical communication is presently limited by loss and dispersion, while the ultimate limit from quantum effects and quantum communication theory has only been partially assessed [1]. To combat the effect of loss for minimizing repeater spacing, optical amplifiers can be used. The recent development of the erbium-doped fiber amplifier is a major advance, which operates close to the ideal noise limit of a *phase insensitive linear quantum amplifier* (PIA). For ordinary coherent-state laser sources, an ideal PIA introduces a 3 dB degradation in the signal-to-noise ratio (SNR) for both homodyne and direct detection [2]. With the use of *phase-sensitive linear amplifiers* (PSA), which are parametric amplifiers employed for single-field-quadrature amplification, there is no signal-to-noise degradation at all for homodyne detection[2]. They are also 3 dB better than PIA for direct detection, and are in fact ideal for any source quantum state if phase coherence at the amplifier input is maintained [3]. Such amplifiers in bulk and fiber-optic form have been recently developed at Northwestern University [4, 5]. The advantage of PSA over PIA is actually much more significant than the 3 dB improvement indicated above. In an amplifier-attenuator chain such as a long-distance fiber-amplifier line, the direct-detection SNR of a PSA system can be up to a factor of 8 better than that of a PIA line [3]. When the effect of gain saturation is taken into account, many more PSA's can be used in a single line compare to PIA's because in a PSA, the total added quantum noise power is only one-fourth that of a PIA [3]. Solitons continue to be developed for long-haul communications. A virtually error-free soliton erbium-amplifier line at 20 Gbits/s has been demonstrated for over 13,000 km [6]. In such a system, the fiber nonlinearity and *amplifier spontaneous emission* (ASE) noise interact to produce a major limitation on the system. It has been estimated, for example, that a four-fold decrease in ASE noise per unit length could enable a doubling of the system length or repeater spacing [7]. It turns out that the total amplified noise in a PSA amplifier-attenuator chain is also just one-fourth that of a PIA chain [3]. A PIA soliton line suffers from the Gordon-Haus limitation [8] due to the accumulation of soliton timing error, which is strongly suppressed in a PSA line by a factor of  $2G^2$  in a single amplifier, where  $G$  is the amplifier power gain[3]. In a PSA soliton amplifier-attenuator chain, the timing error is reduced from that of a PIA line by a factor of  $\alpha = \frac{3}{8(\Gamma L)^2} l \left( \frac{\ln G}{G-1} \right)^2$ , where  $L$  is the total

line length and  $\Gamma$  the fiber loss coefficient per unit length [9]. For  $G \sim 10$ , this effectively suppresses the timing error altogether. Furthermore, the soliton evolution is greatly extended in a PSA chain; the dispersive radiation generated during amplification and decay is strongly suppressed [51]. These significant theoretical results were obtained by our previous effort and we propose to continue their experimental investigations.

If photon-number amplifiers (PNA) are used, there is no degradation for direct detection, independently of the nature and the phase coherence of the source [11]. In particular, an ideal PNA introduces *no* additive noise into the system, a very desirable characteristic from both a theoretical and a practical point of view. In an amplifier-attenuator chain, we have found that a long PNA line can greatly out perform a PIA line in terms of bit error rate (BER) for on-off keying (OOK). In addition to the electronic-optical realization of PNA we have also found new all-optical realizations including one simple scheme specifically adopted for OOK or binary PPM.

These novel quantum amplifiers are also useful in a local network environment. The number of waveguide taps that a passive optical fiber can accommodate is typically quite low, say fewer than 20. One way to increase this number is to employ optical amplifiers. The use of PIA is beset with the problems of ASE and gain saturation [12]. The novel PSA and PNA are again significant in this regard. Furthermore, a waveguide tap has also been proposed on the basis of such amplifiers [13], which is however still limited by noise accumulation and the amount of gain one can employ so that the power in the main line remains below a threshold level. New device concepts, a *photon-number duplicator* (PND), and similarly a *single-quadrature duplicator* (SQD), have been described via nonlinear optical processes [14]. In particular, they can be used to realize the so-called *quantum nondemolition detection* (QND). The utilization of such duplicators could lead to a *transparent local network* with an indefinitely large number of users, which is impossible with amplifiers [13, 14]. We may observe that no optical local network is presently in operation, and the duplicator may provide the key element that makes such networks competitive.

Dispersion is not a problem for local networks except at ultra-high speeds. However, it is still important to integrate the soliton propagation property with the amplifiers PSA and PNA for long-haul applications. Eventually, soliton PNA and duplicators would also be needed for ultra-high speed local networks. All the above discussions presume the use of

ordinary coherent-state sources. Finally, intensity and quadrature squeezed sources may be employed to further enhance performance if loss is not significant as in many local networks. For squeezed sources, only PSA and PNA ( or PND and SQD) can be used because PIA destroys the squeezing [2].

A novel device concept that has emerged from our work on PSAs is that of the soliton regenerator which can be an alternative device to an inline optical amplifier. Basically, an optical regenerator replaces the attenuated solitons (dirty one bits in the OOK format) with locally generated solitons (clean one bits); such a device is thus an optical analog of the electronic repeater. Since the devices we consider are based on the nonlinear refractive index of the fiber which is instantaneous, such devices are ideally suited for the ultra-high speed (100 gigabits and beyond) TDM system. Moreover, optical regenerators can be designed in such a way that the bit stream at one wavelength affects the bitstream at another wavelength. Thus such devices can also be useful in ultra-high speed hybrid TDM/WDM systems.

The capability of a communication network is limited by the switching speed. It is therefore important to consider an all-optic mode of operation including both communication and switching. For example, when picosecond pulses are used in a 100 Gbits/s system, the switching rate would also have to be in the picosecond range. High speed optical switching is of course also crucial in the realization of fast *all-optical computers*. The main difficulty to realize an ultrafast all-optical switch via optical nonlinearity is that very few fast-response materials can achieve a  $\pi$  phase shift in less than one absorption length [15]. Optical fiber turns out to be one such material, and all-optical soliton switching with fibers has been experimentally demonstrated [16]. However, a very long fiber length ( $\sim 1$  km) is required due to the small fiber nonlinearity, which renders the device impractical and noisy.

The bit rates of optical communication networks is currently limited to tens of Gbits/s partly because of the modulation speed limit of the present semiconductor laser light sources. It was shown theoretically that by using microcavity structures, it would be possible to realize semiconductor lasers with a modulation bandwidth up to 1THz because of the much higher stimulated emission rates in microcavities [18]. Recently, Ho et. al. showed that good microcavity semiconductor laser structures can be realized using microscopic photonic structures consisting of strongly-guided waveguides and 1-D photonic bandgap structures [19, 17]. We fabricated the proposed microcavity semiconductor laser structures and investigate

the properties of these new type of lasers. The microcavity structures will enable us to realize future ultrafast semiconductor lasers that will help push forward the capability of optical communication networks to beyond 100Gbits/s.

## **2 Proposed Goals and Summary of Research Performed**

The research program consisted of the following three parts:

- A) Analysis of Device and System Performance**
- B) Soliton Photon Number Amplifiers, Improved Ultrafast All-Optical Switches, and Novel Microcavity Lasers for Optical Communications.**
- C) Dispersion Compensation, Pulse Shaping, Stable Soliton Propagation, and Duplication.**

Below we summarize the proposed goals and the research performed in each of the above areas. A detailed account of the work performed is given in Sec. 3.

### **2.A Soliton Photon Number Amplifiers, Improved Ultrafast All-Optical Switches, and Novel Microcavity Lasers for Optical Communications**

The goals of this part of the research were:

1. to study a prototype realization of photon number amplifier proposed by Yuen and demonstrate that it can be used for amplifying soliton pulses without spontaneous emission noise,
2. to demonstrate that the performance of all-optical switches and nonlinear optical device can be substantially improved via nanofabrication techniques,
3. to study the use of gap solitons in optical communications, and
4. to investigate an experimental realization of microcavity laser structures involving the use of microscopic photonic structures and 1-D photonic-bandgap structures.

#### **2.A.1 The following was accomplished:**

During the past two years of the grant we made significant progress on the theoretical investigation of novel microcavity semiconductor laser and on the experimental demonstration of the first photonic-wire semiconductor laser and all-optical switching using low peak power. Specifically:

- We have achieved lasing in a strongly-guided semiconductor waveguide with mode area as small as  $0.02\mu\text{m}^2$  ( $\lambda = 1.4\mu\text{m}$ ). The lasing action takes advantage of the large enhancement of stimulated emission in the waveguide and its suppression of unwanted dipole emission. We call the waveguide a photonic wire. The laser cavity is a high-Q microcavity ring resonator formed by the photonic wire and has a small cavity mode volume of  $0.27\mu\text{m}^3$ . The laser realized will allow us to study spontaneous emission and lasing in nanofabricated waveguide structures.
- We have successfully demonstrated photonic wire lasers and micro-disk lasers coupled with a output waveguide, and obtained directional light output from the micro-cavity lasers via resonant waveguide coupling. The output was achieved by fabricating  $0.45\mu\text{m}$  wide U-shape waveguide next to a  $10\mu\text{m}$  diameter microcavity ring laser. The output efficiency can be controlled carefully by choosing the spacing between the laser cavity and the waveguide.
- Strongly-guided 1-D waveguide called photonic wire has high spontaneous emission coupling efficiency, enabling one to realize low threshold lasers. The use of 1-D photonic bandgap structure consisting of a 1-D array of holes along a photonic wire may lead to novel photonic-wire micro-cavity lasers. We investigated the fabrication of a 1-D photonic-bandgap structure for  $1.5\mu\text{m}$  wavelength along a InGaAsP photonic wire using nanofabrication techniques and numerical simulation for the structure. However, this structure did not lase, which is needed to optimise to reduce diffraction loss.
- We have fabricated resonator structures and began charaterization. The resonator structures are disks or rings with two adjacent waveguides separated by 0.1 to 0.4 microns. The fabricated ring and disk microcavity resonator diameters range from 5 to 40 microns and they were patterned and etched in two different semiconductor (*InP/InGaAsP* and *GaAs/AlGaAs*) material systems.
- We demonstrated a novel pulse-delayed scheme to realize degenerate optical parametric amplification in  $\chi^{(3)}$  planar waveguides. The scheme utilizes two identical birefringent plates placed before and after a  $\chi^{(3)}$  planar waveguide to implement a single-arm, pulse-multiplexed nonlinear Mach-Zehnder interferometer. Using this scheme, we demonstrate ultrafast degenerate optical parametric amplification in AlGa-As waveguides.

- We have demonstrated all-optical switching with low peak power in a microfabricated AlGaAs waveguide operating at  $1.6\text{ }\mu\text{m}$ . We showed that by using a 1 cm long micro-fabricated strongly-guided waveguide with  $0.8\text{ }\mu\text{m}$  by  $0.9\text{ }\mu\text{m}$  mode cross sectional area, switching is achieved with an average power of 1.2 mW for 82 MHz mode-locked 430 fs pulses. The estimated peak pump power and pulse energy inside the microfabricated waveguide were  $\sim 30\text{ W}$  and  $\sim 14.6\text{ pJ}$ , respectively, which is 5-10 times lower than the values needed with conventional waveguides.
- We have developed an experimental technique that allows the simultaneous measurement of the nonlinear refractive index  $n^{(2)}$  and the nonlinear absorption coefficient  $\alpha^{(2)}$  in waveguides. With minor modifications in the experimental setup, the four-wave mixing gain coefficient can also be measured. Measurements are demonstrated in AlGaAs waveguides.

## 2.B Dispersion Compensation, Stable Soliton Propagation and Regeneration, and Pulse Shaping

The goals of this part of the research were:

1. To demonstrate the bit-rate/distance product improvement achievable with dispersion compensation,
2. To demonstrate that solitons can propagate over ultralong distances without generating dispersive radiation,
3. To demonstrate soliton regenerators as alternatives to optical amplifiers, and
4. To demonstrate optical pulse shaping for improved switching performance.

Below we summarize the research performed towards achieving the above goals. Along the way we also discovered some new properties of PSA's, such as their use in soliton storage rings.

### 2.B.1 Dispersion Compensation Experiments

We proposed a novel approach to combating the pulse broadening effect of group-velocity dispersion (GVD) in a fiber-optic communication link, which relies on the use of phase-sensitive

amplifiers (PSA's) to amplify and shape the short pulses propagating in the fiber [13]. Experiments to demonstrate the dispersion compensation property of PSA's were not conclusive due to the excessive phase noise in the setup, despite our implementation of the Pound-Drever-Hall technique to phase stabilize the laser.

### 2.B.2 Stable Soliton Propagation

- We analyzed the effects of Raman scattering and nonlinear and cubic dispersions on the propagation of short (1 ps) soliton pulses in a nonlinear optical fiber line in which loss is balanced by a periodic chain of PSA's. We showed that in such a fiber line, the Raman effect does not induce a continuously increasing frequency downshift of the propagating soliton, but only a small, finite frequency downshift. In contrast, in a fiber line with erbium-doped fiber amplifiers (EDFA's) the soliton frequency is continuously downshifted by the Raman scattering [14].
- We investigated the implementation of nondegenerate parametric amplifiers in fiber lines that support communication rates of ten's of gigabits per second. The main advantage of such amplifiers is that they are *insensitive* to optical phase, which may make the degenerate amplifiers, i.e., PSA's, difficult to implement in field-deployable systems. Moreover, the nondegenerate amplifiers are WDM compatible. An additional property of these amplifiers is that they also produce an amplified and conjugated replica of the input signal. We showed that if the soliton propagation is alternated between the signal and the conjugate channels, then the effects of second-order dispersion, self-phase modulation, Gordon-Haus timing jitter, and soliton self-frequency shift are all automatically compensated [15]. In addition, if the third-order and nonlinear dispersions balance, then soliton-like pulses are able to propagate with sub-picosecond pulsewidths over distances that are much longer (many hundred times) than the dispersion length.
- We modelled, in finer detail, our proposal for the long-term storage of soliton bit streams in fiber/PSA rings. Such fiber-ring storage devices will be useful as interchange and routing buffers and will be compatible with WDM all-optical soliton networks. Memory elements can be designed that will hold over 1 Mbit of data for almost an indefinite period of time with access times as short as 1  $\mu$ s. Our analysis and numerical

computations now include the effects of soliton-soliton interactions, pulse timing and amplitude fluctuations induced by the quantum noise, and phase noise caused by the guided acoustic-wave Brillouin scattering [16]. We have shown that a PSA significantly enhances the storage ring's stability properties, as compared to the case when a phase-insensitive amplifier (PIA), such as an erbium-doped fiber amplifier (EDFA), is used. The one's (the soliton pulses) are asymptotically stable and that the noise on the zero's of the bit stream (i.e., where solitons are absent) is bounded. The soliton-soliton interactions and quantum-noise-induced pulse timing jitter are substantially reduced by phase-sensitive amplification. We have also demonstrated that by adding a relatively small amount of modulation to the pump pulses that drive the amplifiers, it is possible to eliminate all of the residual pulse interactions and timing jitter.

- Experimentally we have concentrated on the demonstration of the long-term storage of a soliton bit stream in a fiber/PSA line. We have *accomplished* all-optical storage of a picosecond-pulse packet of 1's and 0's in a fiber buffer in which loss is compensated by phase-sensitive amplification. An all-fiber PSA regenerates the stored pulses on each round trip. Storage for periods of time up to 0.4 ms has been observed. Data packets of 10's of kilobits can be stored in this device with use of a higher repetition-rate pump-pulse source [17].

### 2.B.3 Soliton Regeneration

Since soliton regeneration experiments using PSA's require pulsed laser sources with extreme stability, we have, in collaboration with ATx Telecom Systems, Inc. of Naperville, Illinois, developed a highly-stable soliton source by compressing the sinusoidal modulation in the output of a short-cavity Er/Yb bulk phosphate-glass laser operating simultaneously at two frequencies. The 58.55 GHz modulation was converted into a train of 3.2 ps pulses by means of soliton pulse compression in a comb-like dispersion-tailored fiber [18]. By spectrum analysis of the direct-detection photocurrent, the short-term stability of the repetition rate was shown to be less than 10 kHz. A patent disclosure, jointly with ATx, on this invention has been filed.

#### **2.B.4 Pulse Shaping with PSA's**

We investigated two simple methods for producing the non-uniform phase chirp and the resulting pulse-shaping when amplified with a PSA. The self-phase modulation method due to the  $\chi^{(3)}$  nonlinearity of an optical fiber was found to be more efficient than the method of imparting linear dispersion with an optical fiber [47].

### **2.C Analysis of Device and System Performance**

The goals of this part of the research were:

1. To determine the ultimate quantum limit on optical switching by utilizing the quantum state space approach similar in spirit to the suggestion of PNA.

**The following was accomplished:**

- We investigated a squeezed light homodyne detection scheme which, with present-day technology, leads to more than two orders of magnitude data rate improvement over other current experimental systems for moderate loss.

### **3 Methods, Procedures, and Outcomes**

The research program comprised of three main parts, each directed by one of the three co-principal investigators. Below we describe in detail the research performed under this contract. A separate section is devoted to each of the three main parts.

#### **3.A Soliton Photon Number Amplifiers, Improved Ultrafast All-Optical Switches, and Novel Microcavity Lasers for Optical Communications**

The goals of this part of the research were:

1. to study a prototype realization of photon number amplifier proposed by Yuen and demonstrate that it can be used for amplifying soliton pulses without spontaneous emission noise,
2. to demonstrate that the performance of all-optical switches and nonlinear optical device can be substantially improved via nanofabrication techniques,
3. to study the use of gap solitons in optical communications, and
4. to investigate an experimental realization of microcavity laser structures involving the use of microscopic photonic structures and 1-D photonic-bandgap structures.

Below we describe in detail the research towards achieving the above goals.

##### **3.A.1 Demonstration of the first photonic-wire semiconductor laser**

We have demonstrated lasing action in a strongly-guided semiconductor waveguide, which we call photonic wire, with mode area as small as  $0.02\mu\text{m}^2$ , which is small compared to the emission wavelength of  $1.4\mu\text{m}$ . Theory shows that such a strongly-guided one-dimensional waveguide can modify the emission property of the active material significantly [18, 19]. The lasing action takes advantage of the large enhancement of stimulated emission in such a waveguide and its suppression of unwanted dipole emission [20, 21, 22]. The cavities of the lasers realized are high-Q microcavity ring resonators with ring diameter of around  $4.5\mu\text{m}$  formed by the strongly-guided waveguides. The lasing behaviors are in agreement with a theory on the enhancement of spontaneous emission coupling factors in such waveguides.



Figure 1: SEM image of a 4.5 diameter photonic-wire ring laser with  $0.45\mu\text{m}$  waveguide.

Directional outputs from these lasers via resonance photon tunnelling to adjacent nanofabricated waveguides are also demonstrated. The details of the photonic-wire laser fabrication and experimental results are described below.

*InGaAsP/InGaAs* epitaxial layers grown by molecular beam epitaxy on *InP* substrate were used to realize the photonic-wire lasers. The epitaxial layers on top of the *InP* substrate is consisted of a  $0.19\mu\text{m}$  thick *InGaAsP/InGaAs* laser structure. Within the structure, three  $100\text{ \AA}$  thick quantum wells ( $\text{In}_{0.53}\text{Ga}_{0.47}\text{As}$ ) were separated by  $100\text{ \AA}$  thick barriers ( $\text{In}_{0.84}\text{Ga}_{0.16}\text{As}_{0.33}\text{P}_{0.67}$ ). They were sandwiched by two  $700\text{ \AA}$  thick  $\text{In}_{0.84}\text{Ga}_{0.16}\text{As}_{0.33}\text{P}_{0.67}$  layers on both sides.

Nanofabrication techniques, involving electron-beam (E-beam) lithography and reactive ion etching (RIE), were used to fabricate the photonic wire ring semiconductor lasers. A wafer bonding and etching technique we developed was used to transfer the thin ring on top of the low-index  $\text{SiO}_2$  cladding on  $\text{GaAs}$  substrate. First,  $800\text{ \AA}$  thick  $\text{SiO}_2$  was deposited on the wafer via plasma enhanced chemical vapor deposition (PECVD). Electron-beam lithography was used to write photonic wire ring laser patterns on PMMA coated on top of the  $\text{SiO}_2$  layer. The pattern is transferred down to the  $\text{SiO}_2$  layer by etching away the unmasked region using RIE with  $\text{O}_2$  as the etchant gas and then the PMMA was removed. The pattern on  $\text{SiO}_2$  then forms the mask for subsequent etching of the  $\text{InGaAsP}$  layer. RIE was again used to etch the rings down vertically through the  $0.19\mu\text{m}$  *InGaAsP/InGaAs* epitaxial layer into the *InP* substrate. In this step we used a gas mixture of methane, hydrogen, and argon

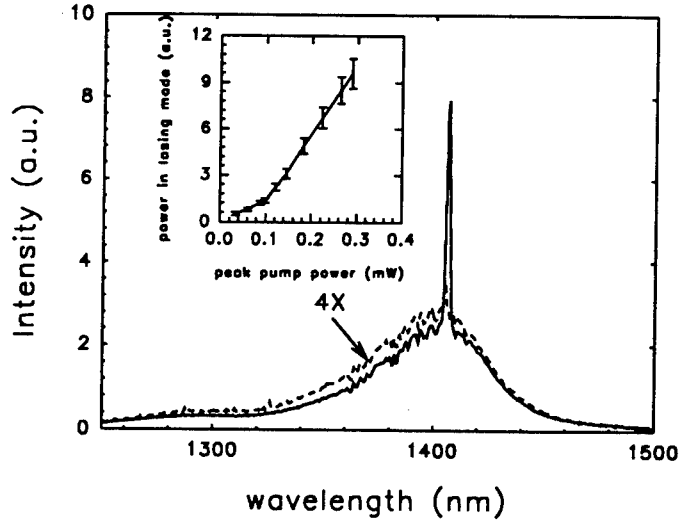


Figure 2: Spectra of photonic wire ring lasers with  $4.5 \mu m$  diameter. The solid line and dash line were measured above (1.5 threshold) and near threshold, respectively. Inset shows the measured power as a function of peak pump power.

with a ratio of 10 : 34 : 10 under the pressure of  $45m\tau$  with 90 W plasma power.

In order to place the thin photonic wire ring laser structure on a low-index material, the substrate was removed via the following technique. The RIE etched sample was deposited with  $0.75 \mu m$  thick  $SiO_2$  using PECVD. A piece of  $GaAs$  substrate covered with  $0.75 \mu m$  thick  $SiO_2$  deposited via PECVD was then prepared. The two samples were  $SiO_2$  face-to-face bonded together using acrylic. Finally, a highly selective  $HCl$  etchant ( $HCl + HPO_4$ , 1 : 1) was used to remove the  $InP$  substrate, leaving the photonic-wire ring laser structure on  $1.5 \mu m$  thick  $SiO_2$  above the  $GaAs$  substrate. Figure 1 shows the scanning electron microscope (SEM) image of a photonic wire ring laser with  $4.5 \mu m$  diameter and  $0.4 \mu m$  ring width.

In the experiments, photonic wire ring lasers with  $4.5 \mu m$  and  $9 \mu m$  diameter and ring widths of  $0.4 \mu m$  were fabricated. The typical measured emission spectra of a  $4.5-\mu m$  photonic wire ring lasers are shown in Figure 2, indicating lasing at  $1403 nm$ . The dashed curve in Figure 2 is the spectrum of the  $4.5 \mu m$  ring laser running near threshold where the peak pump power incident on the ring lasers is approximately  $98 \mu W$ , while the average power was  $0.98 \mu W$ . Power in lasing mode as a function of the peak pump power is shown in the inset of Figure 2 for the  $4.5-\mu m$  photonic wire ring laser.

The enhanced photoluminescence below threshold near the cavity resonance wavelength

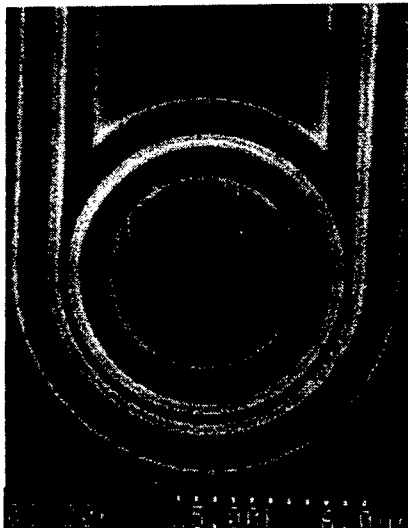


Figure 3: SEM images of the fabricated  $10 \mu\text{m}$  diameter photonic-wire laser with waveguide output coupling.

can be used to measure the cold cavity  $Q$  value, equal to  $\lambda_0/\delta\lambda_0$ , where  $\lambda_0$  is the center frequency of the resonance line and  $\delta\lambda_0$  is the full width at half-maximum. In our case  $\delta\lambda_0$  was measured to be  $5 \text{ nm}$  for the  $9 \mu\text{m}$  ring laser, therefore, the cold cavity  $Q$  value is around 300 comparable to that of microdisk. The spectral linewidth of a  $4.5 \mu\text{m}$  diameter photonic wire laser was measured to be about  $0.5 \text{ nm}$ .

### 3.A.2 Demonstration of the first directional light output from the microcavity semiconductor laser

We have successfully demonstrated photonic wire ring laser and microcylinder semiconductor laser coupled with a output waveguide, and obtained directed light output from the waveguides. Because of strong circular optical waveguide structure emission light is trapped inside the micro-resonators. For application it is necessary to obtain directed light output from the micro-lasers.

In order to obtain light output from the photonic-wire laser we have also demonstrated photonic-wire lasers with waveguide output coupling. A waveguide adjacant to the ring laser encircle it for half a circle as shown by the dotted line in Figure 3. The amount of coupling can be adjusted via choosing the gap size between the laser and waveguide. Waveguide coupled output light of a micro-disk laser was imaged using an infrared camera as shown in Figure 4. In front of the camera two silicon filters were used to block the pumping light (@



Figure 4: The infrared image of a  $10 \mu m$  micro-ring laser. The lasing whispering-gallery mode and the bright emitting spots at the ends of waveguide can be seen clearly.

514 nm) to make sure the image was actually formed by lasing light. From the image we see the lasing whispering-gallery mode around the edge of the disk as well as two bright end-emitting spots at the ends of waveguide. On the monitor screen these two spots change from dim to bright when the pump light increased. This image clearly shows that the waveguide directs the lasing light out from the micro-cavity lasers. Similar images were observed for the micro-ring lasers.

The basic structure of the waveguide coupled microcylinder laser with cleaved waveguide facets is shown in Fig. 5. A microcylinder, with  $10 \mu m$  in diameter, is half surrounded by a waveguide. The width of the waveguide is chosen to match the mode size of the fundamental mode in the cylinder cavity. In this way resonant optical tunneling between the cylinder cavity and waveguide can be reached. The amount of coupling can be controlled by chosen gap spacing between the cylinder cavity and waveguide. In our initial experiments the structure with two different gap spacing, 0.5, and  $0.3 \mu m$ , were fabricated. The estimated coupling efficiency is around 1%. The low coupling efficiency is chosen to maintain a high Q value for the cylinder resonator.

The layer waveguide structure used in our experiments is grown by molecular beam

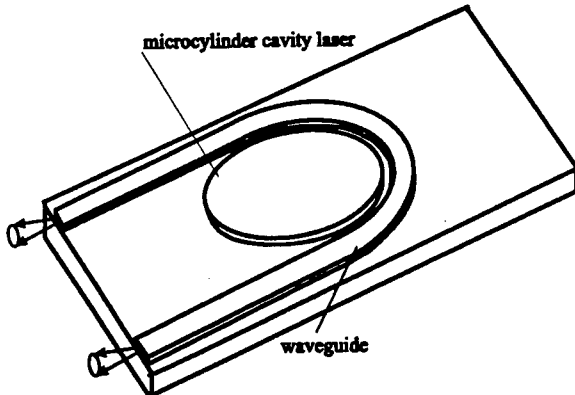


Figure 5: Schematic diagram of a microcylinder laser coupled with output waveguide.

epitaxy (MBE) with the  $InGaAs/InGaAsP$  material system. A  $0.2 \mu\text{m}$   $InP$  buffer layer is grown on the top of the semi-insulating (100)  $InP$  substrate. Fifteen (100 /AA)  $In_xGa_{1-x}As$  quantum wells are then sandwiched by (100 /AA)  $In_xGa_{1-x}As_yP_{1-y}$  barrier layers. The total thickness of the MQW layer structure is  $0.6 \mu\text{m}$ .

The typical emission spectra of a  $10 \mu\text{m}$  microcylinder lasers is shown in Fig. 6, indicating lasing at  $1490 \text{ nm}$ . In our initial experiments the laser has a high threshold pump power. We think this is due to fifteen quantum wells and poor wafer quality (too many defects). Directed emission light from the cleaved waveguide facets are obtained. The infra-red imaging of the laser light output from the cleaved waveguide facets is shown in Fig. 7.

### 3.A.3 Investigation of novel microcavity semiconductor laser structure

We have investigated novel microcavity semiconductor laser structure. The theoretical studies was done in collaboration with Prof. Allen Taflove at Northwestern University, who is an expert in linear and nonlinear computational electromagnetics.

1-D photonic-bandgap stuctures [23, 24, 25] are investigated. The 1-D photonic-bandgap is similar to Bragg reflector used in the vertical cavity surface-emitting lasers and distributed feedback lasers, but differs in the geometrical realization. It is consisted of an array of holes etched into a high refractive-index dielectric. An example is shown in Figure 8, where six holes were etched periodically in a photonic-wire waveguide to form a photonic-bandgap reflector. Figure 8 also shows a microcavity formed by two arrays of six holes at each end of the photonic wire.

We have developed two-dimensional numerical models for photonic-bandgap structures.

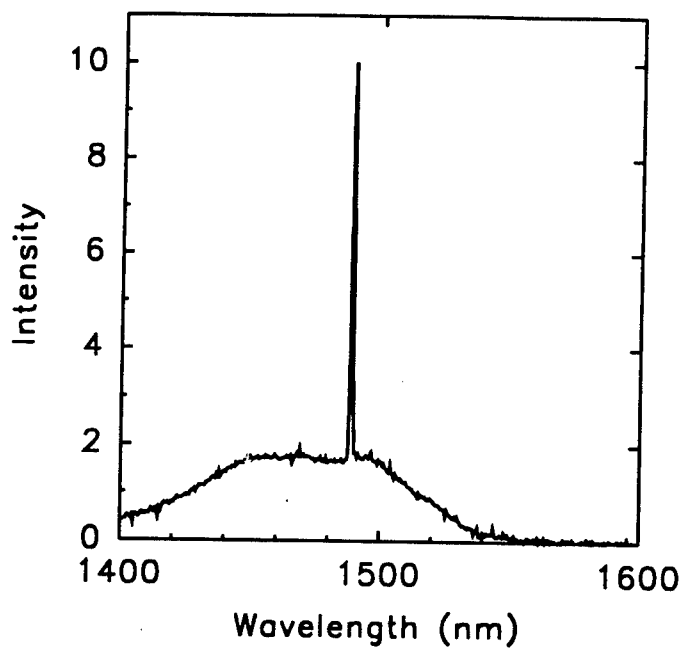


Figure 6: Spectra of a microcylinder laser with  $10 \mu\text{m}$  diameter.



Figure 7: Infra-red image showing the output of a microcylinder laser coupled with waveguide.

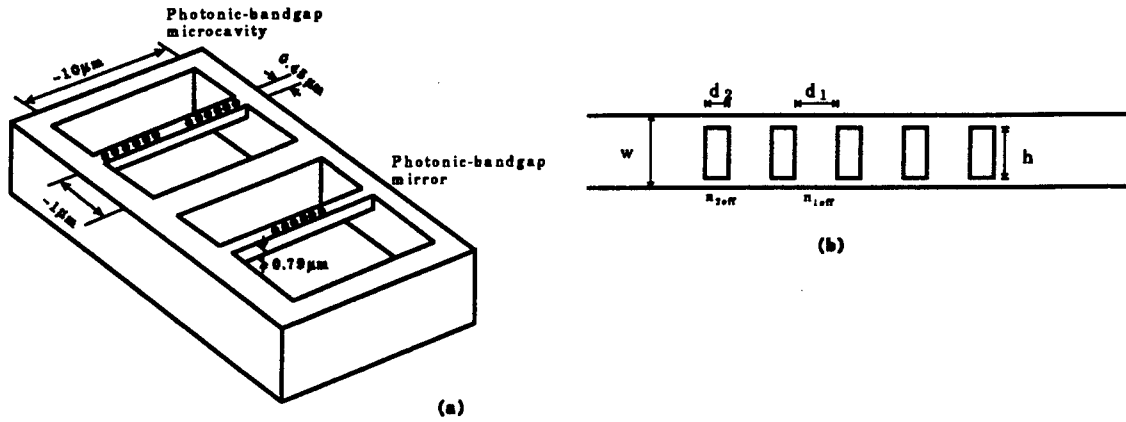


Figure 8: Schematic diagram of the suspended photonic-wire mirror and micro-cavity. Holes were etched in the photonic wire to from a one-dimensional photonic-bandgap structure.

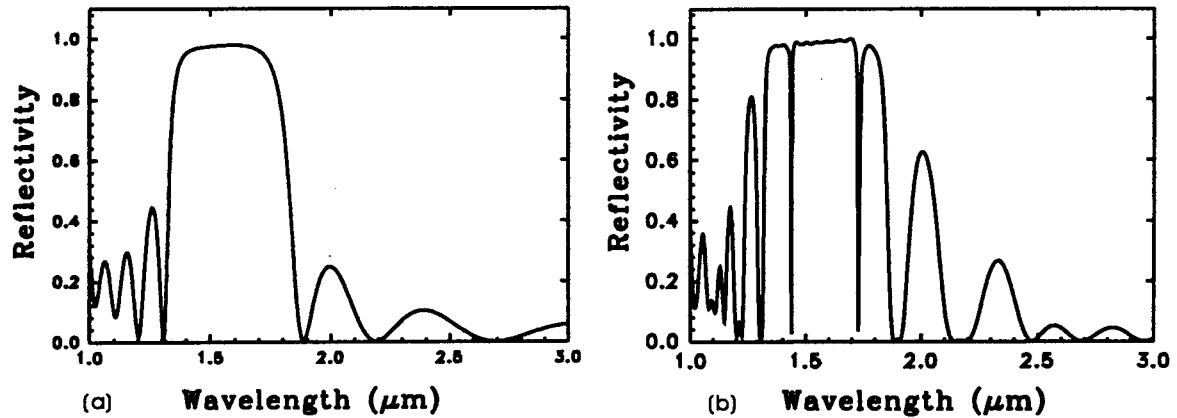


Figure 9: (a) Calculated reflection spectrum of a  $0.3 \mu m$  photonic-wire mirror with six rectangle holes. (b) Calculated reflection spectrum of a  $0.3 \mu m$  photonic-wire caivity with six rectangle holes .

using the finite-difference time-domain (FD-TD) method [26] to solve for the electric field propagation of broadband femtosecond pulses. A  $0.3 \mu m$  wide photonic wire with six rectangular holes is modeled with a uniform spatial resolution of  $0.0125 \mu m$ . The holes are  $0.25 \times 0.1 \mu m^2$ , and the spacing between them is  $0.225 \mu m$ . This initial 2-D model assumes no spatial variation in the direction perpendicular to the simulation plane, so the height of the holes is assumed to be unbounded. Reflection spectra can be obtained from the time-domain data via discrete Fourier transform.

Figure 9(a) shows the reflectivity of the photonic-bandgap mirror as a function of the wavelength. We see that the photonic bandgap mirror is a broadband reflector with about



Figure 10: Geometry and field distribution in a  $0.3 \mu\text{m}$  photonic-wire microcavity. The cavity length is  $0.775 \mu\text{m}$ , and six ( $0.225 \times 0.1 \mu\text{m}^2$ ) holes are on either side to form a Fabry-Perot cavity.

450 nm bandwidth. With six holes the photonic-wire mirror's reflectivity can be as high as 0.98 compared with the multilayer distributed Bragg reflector (DBR) used in vertical cavity surface emitting lasers in which more than twenty pairs of Bragg reflectors are needed.

Figure 9(b) shows the calculated reflectivity spectrum for a  $0.3\mu\text{m}$  suspended photonic-wire micro-cavity illustrated in Figure 8. The reflectors consist of six holes on either side with the parameters the same as those used in Figure 9(a). The physical cavity length, the distance between the holes on either side of the cavity, is  $0.775\mu\text{m}$ . From Figure 9(b) we estimate the Q-value is around 500, which agrees approximately with Q estimated from cavity intensity decay time. By varying the parameters, we can adjust the number of resonant modes in the gap, the center frequency of the gap, and gap bandwidth. In our simulations we assume the operation wavelength is  $1.5\mu\text{m}$  and the material is *InGaAs/InGaAsP* system. Figure 10(c) shows the calculated electric field of the resonant mode.

As a step towards the realization of the photonic-wire micro-cavity lasers, we have successfully fabricated suspended photonic-wire structure with multiquantum well *InGaAsP/InGaAs* material system, which was grown by molecular beam epitaxy (MBE) technique. Such suspended structure can be etched via selective etch analogous to the suspended bridge-like microcavity structure fabricated by Ho et. al. with *AlGaAs/GaAs* material system. A  $0.2\mu\text{m}$  thick *InP* buffer layer was grown on the *InP* substrate. The waveguide layer is comprised of eight  $100\text{\AA}$  quantum wells separated by  $100\text{\AA}$  barriers and sandwiched by two  $0.32\mu\text{m}$  thick *InGaAsP* cladding. The total waveguide layer thickness is  $0.79\mu\text{m}$ .

Nano-fabrication techniques were used in the fabrication process. First, a  $800\text{\AA}$  thick *SiO<sub>2</sub>* was deposited on the *InGaAsP/InGaAs* wafer using plasma enhanced chemical vapor deposition (PECVD). PMMA was then spun on top of the *SiO<sub>2</sub>* to act as an electron-beam resist. The micro-cavity pattern was written in the PMMA with the JEOL JBX 5DII

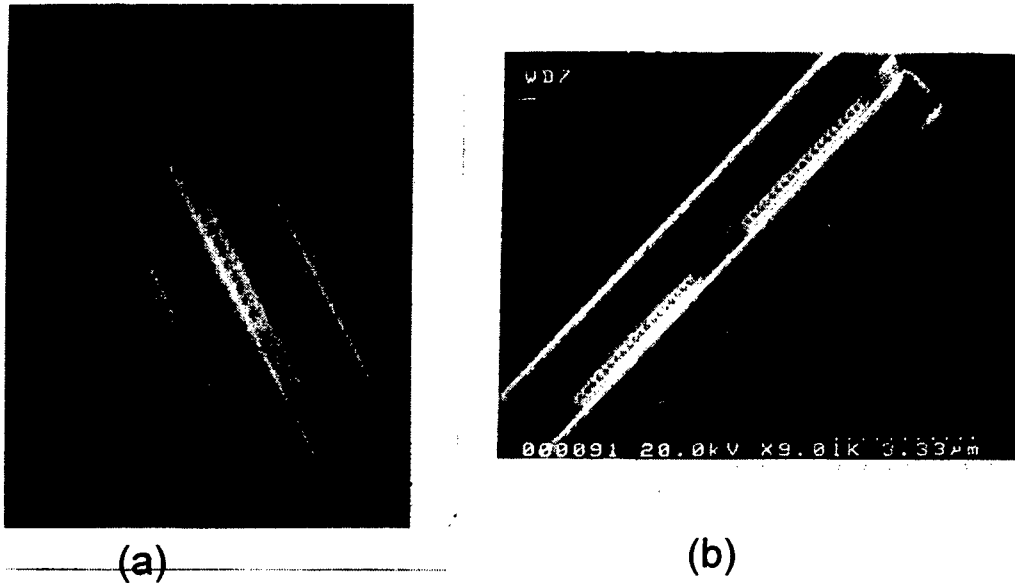


Figure 11: (a) SEM image of a micro-cavity before selective etching. (b) SEM image of a micro-cavity after selective etching

electron-beam (E-Beam) writer. After that the pattern was transferred down to the  $SiO_2$  layer using reactive ion etching (RIE). The RIE was performed with  $CHF_3$  as the etchant gas under  $31\text{ mtorr}$  pressure and  $60\text{ W}$  plasma power. The PMMA was then removed. The pattern on  $SiO_2$  formed the mask for subsequent etching of the  $InGaAsP$  layer. RIE was again used to etch the photonic wire and holes down vertically through the  $0.79\mu\text{m}$  thick epitaxial layer into the  $InP$  substrate. In this RIE step we used a gas mixture of methane, hydrogen, and argon with a ratio of 10:34:10 under  $45\text{ mtorr}$  pressure and  $90\text{ W}$  plasma power. Finally the suspended structures were formed using highly selective  $HCl$  etchant to remove the  $InP$  material beneath the epitaxial layer.

Figure 11(a) and Figure 11(b) shows the scanning electron microscope (SEM) photos of the suspended photonic-wire microcavities. Figure 11(a) is the SEM photo before selective etching and the bottom can be seen clearly. After selective etching the material under the microcavity was removed as shown in Figure 11(b). The suspended micro-cavity is  $11\ \mu\text{m}$  in length,  $0.45\ \mu\text{m}$  in width, and  $0.79\ \mu\text{m}$  in thickness. In order to reach high reflectivity, 20 holes were etched in the photonic wire. The successful fabrication of the suspended structure is an important step towards the realization microcavity lasers based on photonic-bandgap structure.

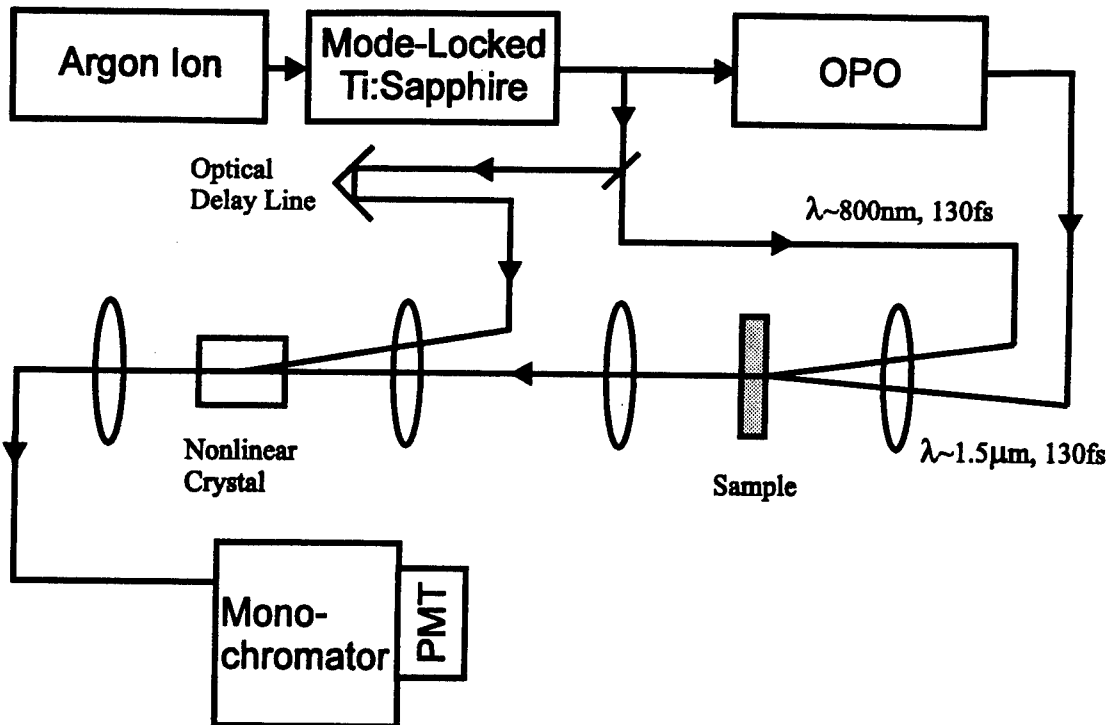


Figure 12: Experimental setup of a microcavity semiconductor laser characterization.

### 3.A.4 Characterization of Novel Microcavity Semiconductor Lasers

Preparations for experiments to study some predicted ultrafast phenomena associated with microcavity lasers are now in progress. We will use femtosecond laser pulses to optically pump our samples, the resultant emission will be upconverted using frequency summation with another femtosecond laser beam in a nonlinear optical crystal, and then fed into a monochromator to select out the desired signal, which will be detected by a photon counting system. The experimental setup is illustrated in Fig. 12.

A key part of these experiments, the tunable femtosecond laser sources, has already been set up and tested. An all-lines argon ion laser is the pump source for a mode-locked titanium sapphire laser. The Ti:Sapphire laser provides us ultrashort pulses of about 130fs in duration, and over 20nJ of energy per pulse. The wide wavelength tuning range in the near-infrared part of the spectrum gives us the flexibility to select the photon energies for the pumping of our samples. Furthermore, there is also an optical parametric oscillator (OPO) pumped by the mode-locked Ti:Sapphire, its signal output can cover the wavelength range from about  $1.3\mu m$  to  $1.6\mu m$ . With the OPO, we have the option of pumping our microlasers very close to its lasing wavelength for the study of their intrinsic dynamical properties. Over all, the

versatility of the laser system makes it an ideal tool for our planned investigation.

We will use a large numerical aperture microscope objective lens to collect the light emission from our samples. The signal will then be focused into a BBO crystal, which will also be pumped with a femtosecond laser beam. Because the pump pulses are very short compared with the signal pulse, they will also serve as time gates that allows us to trace out the time history of the signal by varying the relative time delay between the two pulse trains. This will permit us to study the microcavity dynamics with femtosecond time resolution.

The upconverted signal will be in the visible range, and can be separated from other light fields with bandpass filters and by passing the beam through a monochromator. Since the expected signal will be quite weak, we are going to use a photo-multiplier tube (PMT) at the output of the monochromator as the detector. A fast photon counter will be employed to process the signal from the PMT. The detection system will be sensitive down to a few photons per second. Data acquisition will be accomplished with a computer, which will also be used to control the optical delay for synchronization.

At the present time, most of the equipment necessary for the experiments are already in place, and shortly the whole setup will be put together and tested. Initial experimental data can be expected within a few month.

### **3.A.5 Fabrication of Micro-Resonator Structure**

The disk or ring microcavity resonator is a potentially low-power, integrable, electro-optically controlled device, and can be used as a wavelength multiplexer/demultiplexer, switch or modulator. Since semiconductors have a high refractive index, there is strong waveguide confinement and the semiconductor disk resonator can be of micron dimensions. This small disk size results in a high finesse and gives a small minimum resolvable bandwidth and high channel capacity. Since the free-spectral range of the resonator is inversely proportional to the disk diameter, the disk resonators could have a wide free-spectral range.

During this budge periode we have made resonator structures and began charaterization. The resonator structures are disks or rings with two adjacent waveguides separated by 0.1 to 0.4 microns. The fabricated ring and disk microcavity resonator diameters range from 5 to 40 microns and they were patterned and etched in two different semiconductor (*InP/InGaAsP* and *GaAs/AlGaAs*) material systems.



Figure 13: Scanning Electron Microscope (SEM) image of a microcavity resonator with 5 micron diameter.

There were two types of layered semiconductor materials that were used in making the microcavity resonator devices. The first (called NUMBE) was passive and composed of a buffer layer of AlGaAs ( $x = .4$ ) which was  $2 \mu\text{m}$  thick, followed by a  $0.45\text{-}\mu\text{m}$ -thick guiding layer of GaAs with a  $0.25\text{-}\mu\text{m}$ -thick layer of AlGaAs( $x=.4$ ) on top to serve as additional cladding. The top layer creates a symmetric waveguide and allows confinement of the wave even when guided in an extremely thin layer. The second material (called InP15QW) was an active InP/In GaAsP sample that contained 15 quantum wells. The microcavity resonator devices on this sample could be used either as passive modulators and switches (if the signal wavelength is far enough away from the quantum well bandgap) or, if pumped, they could double as active laser devices.

For our critical submicron design parameters, we require nanofabrication processes with a highly directional etching process. The resonator devices were fabricated by using electron beam lithography in conjunction with reactive ion etching and chemically-assisted ion beam etching. Upon SEM inspection, we observed smooth, straight sidewalls and high definition of all features as shown in Fig. 13.

We have observed enhanced cavity modes microcavity structures fabricated from InP/In GaAsP with 15 quantum wells. A second material that we patterned and etched was a passive GaAs/AlGaAs sample. We have observed waveguiding and resonant peaks in these

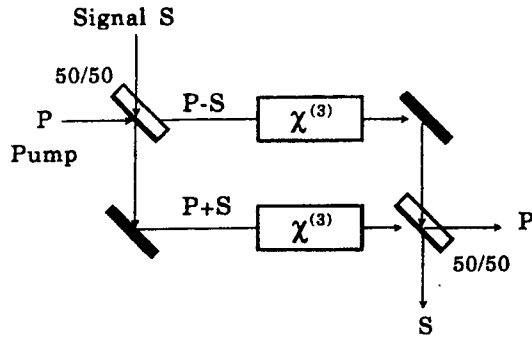


Figure 14: NMZI scheme for a  $\chi^3$ -based degenerate OPA.

structures and are currently characterizing the resonance behavior.

### 3.A.6 Degenerate Optical Parametric Amplification in $\chi^{(3)}$ Waveguide

As part of the previous contract degenerate optical parametric amplification in  $\chi^{(3)}$  waveguide with pulse-delayed scheme was demonstrated in AlGaAs waveguides. Planar waveguide optical parametric amplifiers (OPA's) are potentially attractive for realizing compact phase-sensitive optical amplifiers. Nondegenerate OPA's have been demonstrated in  $\chi^{(2)}$  Ti-difussed  $LiNbO_3$  waveguides, for which phase matching of the pump and the signal is achieved by temperature tuning. Degenerate OPA's (DOPA's) utilizing the  $\chi^{(3)}$  nonlinearity can be more desirable, as in this case the phase-matching condition is automatically satisfied because the pump and the signal are at the same wavelength. The main obstacle in realizing DOPA's in  $\chi^{(3)}$  planar waveguides has been the difficulty in separating the pump beam from the signal beam at the waveguide output because both beams have the same polarization.

Recently Shirasaki and Haus proposed a nonlinear Mach-Zehnder interferometer (NMZI) DOPA scheme in which an identical  $\chi^{(3)}$  waveguide is placed in each arm of the interferometer, as shown in Fig. 14. In this scheme pump P and signal S enter the interferometer from opposite sides of an input 50/50 beam splitter. After the signal is amplified by the pump by a parametric process in the nonlinear waveguides, the pump is separated from the amplified signal at the output 50/50 beam splitter. The NMZI DOPA scheme was demonstrated in optical fibers with a nonlinear loop mirror configuration. In principle, this scheme can also be realized with two identical  $\chi^{(3)}$  planar waveguides and active stabilization of the interferometer. However, the difficulty in fabricating two identical waveguides and the complexity

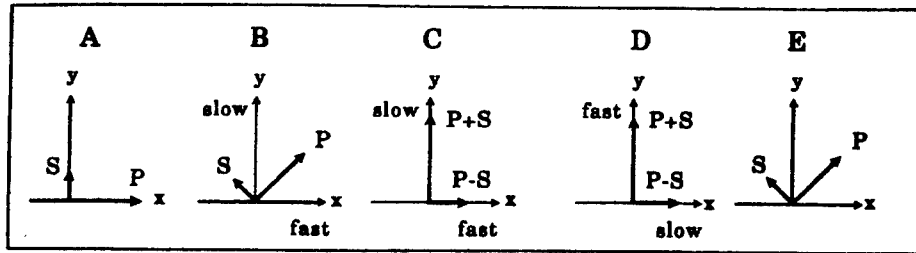


Figure 15: Novel pulse-delayed DOPA scheme.

of active stabilization make this scheme less attractive for future device realization.

We demonstrated a novel pulse-delayed scheme for realizing DOPA's in  $\chi^{(3)}$  planar waveguides. The scheme utilizes two identical birefringent plates, one placed before and one after a  $\chi^{(3)}$  planar waveguide, to implement a single-arm, pulse-delayed NMZI. The key element in the scheme is the birefringent plates that are used as polarization-sensitive optical pulse delay lines. Our scheme is equivalent to the two-arm NMZI DOPA scheme but differs in that it replaces the spatial separation of pulses in the two arms with a time separation in a single arm.

Fig. 15 is a schematic diagram of our DOPA scheme; the polarizations of the pulses at positions A-E are shown in the inset. A linearly polarized pump pulse P and an orthogonally polarized signal pulse S are combined at polarization beam splitter cube PBS2. Their polarizations at position A are shown in the inset where the signal is polarized along the y axis and the pump is polarized along the x axis. Using half-wave plate HP3, we rotate the polarization of both the pump and the signal pulses by 45°. The pump and the signal pulses are then sent through birefringent plate BP1, which has its fast and slow axes aligned with the x and the y axes, respectively, as shown in the inset at B. The pump and the signal pulses interfere at BP1, resulting in a P + S pulse polarized along the slow axis (y axis) and in a P - S pulse polarized along the fast axis (x axis), as shown in the inset at C. Because of the difference in propagation velocities between the fast and slow axes of BP1, the P + S

pulse becomes delayed in time by an amount  $T$  with respect to the P - S pulse at the output of BP1. This time delay is given by  $T = d\delta n/c$ , where  $d$  is the thickness of the plate,  $\delta n$  is the refractive-index difference between the fast and the slow axes, and  $c$  is the speed of light in vacuum. The time delay  $T$  must be such that the leading P - S pulse and the trailing P + S pulse are completely separated in time. Otherwise, an elliptically polarized component will be generated that will degrade the performance of the DOPA.

After going through BP1, the P - S and the P + S pulses are coupled into the  $\chi^{(3)}$  waveguide, exciting a TE and a TM mode, respectively. In the  $\chi^{(3)}$  waveguide the signal components of P - S and P + S pulses are either amplified or deamplified (depending on the signal-pump phase mismatch) by their respective pump components by means of the parametric process. Because the parametric gain as a function of the signal-pump phase mismatch has a  $\pi$  periodicity, both signal components are amplified or deamplified simultaneously. We can see this by noting that, if the pump and the signal fields in the P + S pulse are in phase, then the pump and the signal fields in the P - S pulse will be out of phase by  $\pi$ . The amplification of the signal pulse will be maximum when the signal-pump phase mismatch is either 0 or  $\pi$ . After going through the waveguide, the leading P - S pulse and the trailing P + S pulse pass through a second birefringent plate, BP2, which is identical to BP1 but with its slow and fast axes rotated by  $90^\circ$ , as shown in the inset at D. At BP2 the trailing P + S pulse overlaps the leading P + S pulse in time, and the two interfere, resulting in a pump pulse P orthogonally polarized to an amplified signal pulse S, as shown in the inset at E. We spatially separate the pump pulse from the amplified signal pulse by rotating the polarization of both the pump and the signal by  $-45^\circ$ , using half-wave plate HWP1 and passing the beams through a polarization beam splitter cube (PBS3). Two important requirements must be satisfied to ensure maximum DOPA gain and minimum pump leakage into the amplified signal at the output of the DOPA: (a) the waveguide material must be isotropic so the signal components in P + S and P - S experience the same gain and (b) the two birefringent plates must be identical to allow the P + S and P - S pulses to overlap completely in time and to interfere at the second birefringent plate.

A schematic of the experimental setup to demonstrate our DOPA scheme is shown in Fig. 16, where the DOPA section is denoted by the dashed box. The laser source was an additive-pulse mode-locked color-center laser (NaCl:OH), generating 220-fs pulses at a  $\lambda$

MHz repetition rate. We obtained a strong pump beam and a weak orthogonally polarized signal beam by splitting the output of the laser using half-wave plate HP1 and polarization beam splitter PBS1. We varied the pump beam intensity by using a combination of half-wave plate HP2 and polarizer P1. The pump and the signal beams were combined at polarization beam splitter PBS2 (i.e., the pulses spatially and temporally overlap but are still orthogonally polarized) and passed through half-wave plate HP3 and 4-mm-thick calcite birefringent plate BP1, generating the P + S and P - S pulses separated in time by 2 ps. The optical phase of the signal pulses with respect to the pump pulses was adjusted with a piezoelectric transducer. The P - S and P + S pulses were end-fire coupled into a 2.2-cm-long strip-loaded AlGaAs waveguide by 40X microscope objective lens. The AlGaAs waveguide comprised a 1.0- $\mu\text{m}$ -wide by 1.5- $\mu\text{m}$ -thick  $\text{Al}_{0.27}\text{Ga}_{0.73}\text{As}$  stripe, a 1.5- $\mu\text{m}$ -thick  $\text{Al}_{0.23}\text{Ga}_{0.77}\text{As}$  guiding layer, and a 3.5- $\mu\text{m}$ -thick  $\text{Al}_{0.27}\text{Ga}_{0.73}\text{As}$  lower cladding layer, all grown on top of a semi-insulating GaAs substrate. The waveguide had an estimated mode cross-sectional area of 5  $\mu\text{m}^2$ . After going through the waveguide, the pulses were recollimated and passed through a second 4-mm-thick calcite plate (BP2), where the P - S and P + S pulses overlapped in time and interfered to yield orthogonally polarized pump and amplified signal pulses. The separation of the pump from the signal was accomplished by the combination of half-wave plate HP4 and polarizing beam splitter cube PBS3. The amplified signal was detected by photodiode PD1.

Fig. 17 shows typical data traces obtained in our experiments. Fig. 17 shows the output signal for the cases when the pump is on and off as a function of the signal-pump phase mismatch, normalized to the output signal level when the pump is off. We varied the signal-pump phase mismatch by varying the phase of the input signal at 100 Hz with a piezoelectric transducer. As can be seen from Fig. 17(a), when the pump is on the signal experiences both parametric amplification and parametric deamplification as the phase of the input signal is varied. A maximum signal parametric gain of 3.3 was obtained when the signal-pump phase mismatch was 0 or  $\pi$ , whereas the maximum parametric deamplification was 0.5 when the signal-pump phase mismatch was  $\pi/2$  or  $3\pi/2$ . Note that adjacent deamplification maxima have unequal magnitude; we attribute the fact to the expansion (less than a full wavelength) of the piezoelectric transducer. For this case the pump and the signal intensities inside the waveguide were estimated to be 1. 16 and 0.35  $\text{GW}/\text{cm}^2$ , respectively. Fig. 17(b) shows the

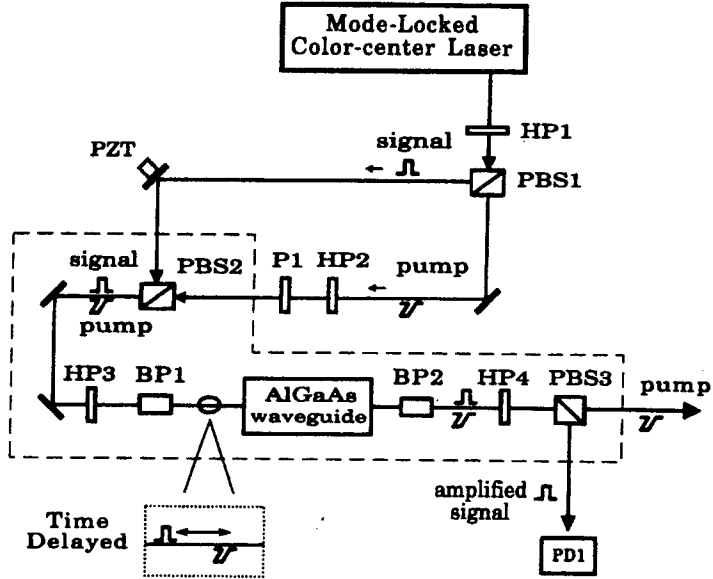


Figure 16: Experimental setup to demonstrate the pulse-delay DOPA, using AlGaAs waveguide.

interference between the pump and the signal pulses that we obtained by splitting off a small percentage of the beam after PBS2. A comparison between Figs. 17(a) and 17(b) shows that the amplification maxima of the signal have a period that is twice that of the interference maxima, which confirms that the signal amplification results from a parametric process. As mentioned above, it is important to minimize the amount of pump leakage into the amplified signal. In the experiments the amount of pump leakage was found to be 5% of the input pump, and we determined it by blocking the input signal beam. In all the parametric gain measurements the pump leakage was subtracted from the amplified signal trace.

Fig. 18 shows the normalized DOPA gain of the signal as a function of pump intensity in the AlGaAs waveguide for the case when the signal intensity was  $I_s = 0.35 \text{ GW/cm}^2$  and the signal-pump phase mismatch was zero. As the figure shows, when the pump intensity  $I_p$  was low, in the range  $0.2\text{--}0.7 \text{ GW/cm}^2$ , there was a modest signal parametric gain. However, as the pump intensity was increased to the maximum available level of  $1.4 \text{ GW/cm}^2$ , the parametric gain increased substantially. The behavior of the parametric gain can be understood from the equation  $I_s^{norm} = (I_p/I_s) \sin^2(\phi_{nl}) + \cos^2(\phi_{nl})$ , where  $\phi_{nl} = (2\pi/\lambda)n^{(2)}L(I_p I_s)^{1/2}$ , is the nonlinear phase shift. Here  $I_s^{norm}$  is the amplified signal normalized by the input signal,  $\lambda$  is the wavelength of light in free space,  $n_{(2)} = 3.2 \times 10^{-14} \text{ cm}^2/\text{W}$  is the intensity-dependent refractive index of AlGaAs,  $L$  is the waveguide length,  $I_p$  is the pump intensity, and  $I_s$  is

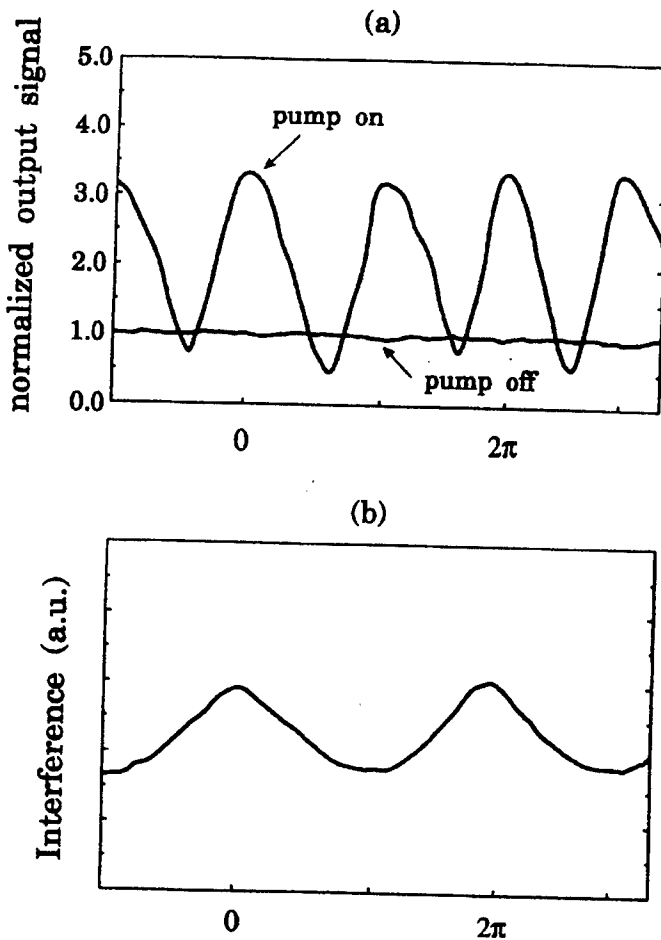


Figure 17: (a) Normalized output signal for the case when the pump is on and off:  $I_p = 1.16\text{GW}/\text{cm}^2$  and  $I_s = 0.35\text{GW}/\text{cm}^2$ ; (b) interference between pump and signal as a function of the pump-signal phase mismatch.

the signal intensity. In the low pump intensity regime,  $\phi_{nl}$  is less than  $0.5\pi$ , which from the above equation shows that the gain is proportional to  $I_s^{\text{norm}} = (I_p/I_s)\sin(\phi_{nl})^2$ . Because the pump intensity is approximately twice the signal intensity, the maximum normalized gain will be limited to less than 2. As the pump intensity increases, the normalized signal gain is proportional to  $I_s^{\text{norm}} = I_p/I_s$ , because the sinusoidal component  $\sin(\phi_{nl})^2 \leq 1$ . For the maximum available pump intensity of  $I_p = 1.4\text{GW}/\text{cm}^2$  the normalized gain is 4, in agreement with the experimental data. In general, the gain of the DOPA is limited by the ratio of the pump-to-signal intensity. In our experiments, the gain was limited to about 4 (6 dB) because of the 5% pump leakage, which sets the lower limit on the input signal intensity.

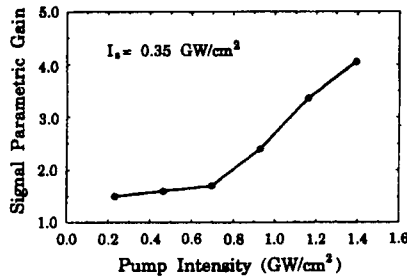


Figure 18: Normalized degenerate OPA gain of the input signal as function of pump intensity inside the AlGaAs waveguide.

### 3.A.7 Development of a new method to measure third-order optical nonlinearities in waveguides

In the process of realizing the compact ultra-fast all-optical switch, we developed a single-beam method that allows the simultaneous measurement of the nonlinear refractive index  $n^{(2)}$  and the nonlinear absorption coefficient  $\alpha^{(2)}$  in waveguides. Several techniques have been used to investigate the nonlinear refractive index  $n^{(2)}$  and the nonlinear absorption coefficient  $\alpha^{(2)}$  of materials. The Z-scan technique [32] based on beam self-focusing has been used to measure  $n^{(2)}$  and  $\alpha^{(2)}$  in samples of glass and semiconductors. Although this technique is simple and sensitive, it is not applicable to waveguides. In waveguides, both fringe-shift interferometry [33, 34] and pulsed-modulated interferometry [35] have been used to directly measure  $n^{(2)}$  and  $\alpha^{(2)}$ , while time division interferometry [36] and heterodyne pump-probe [37] have been used to measure the dynamics of  $n^{(2)}$  and  $\alpha^{(2)}$  in devices such as laser diodes and laser amplifiers. In this report we describe a method that also allows separate measurement of the fast electronic  $n^{(2)}$  and the slow thermal  $n^{(2)}$ . Furthermore, the four wave-mixing gain coefficient can also be measured with minor modifications in the experimental setup. We first present an overview of the basic ideas behind the measurement scheme and discuss the detection techniques required to measure the parallel and perpendicular components of  $n^{(2)}$  and  $\alpha^{(2)}$ . The details of the actual experimental set up for measuring  $n^{(2)}$  and  $\alpha^{(2)}$  in AlGaAs semiconductor waveguides are presented later on in the text. The measurement scheme is based on a balanced Mach-Zehnder interferometer shown in Fig.19, where the nonlinear waveguide is located in one arm of the interferometer. An input beam of frequency  $\omega_s$  is split at the beam splitter BS1 into two beams, a signal beam and a local oscillator (LO) beam. In the absence of the pump beam, the signal beam traverses the arm

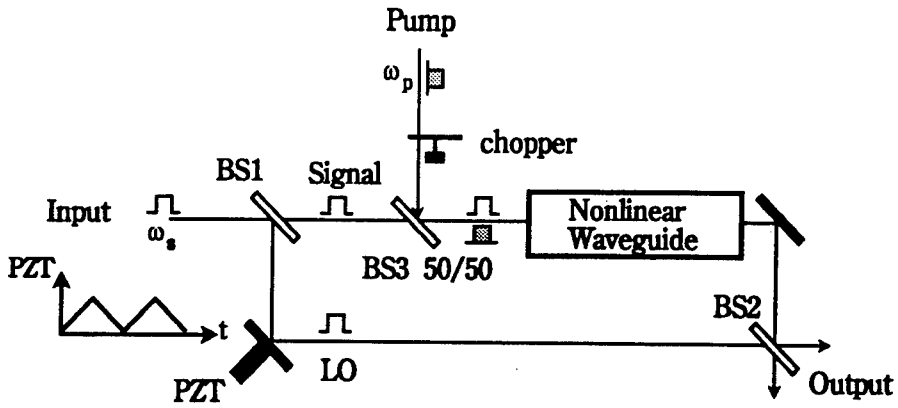


Figure 19: Schematic of the balanced Mach-Zehnder interferometer, with Signal and LO pulse at frequency  $\omega_s$ , and pump pulse at frequency  $\omega_p$ .

containing the waveguide and recombines with the LO beam at beam splitter BS2 where the signal and LO beams interfere. The interference signal has a sinusoidal time variation due to the linear phase change imposed on the LO beam via a piezo-electric transducer (PZT). If the phase of the LO beam has the form:  $\phi_{LO} = \omega_{ph}t$ , where  $\omega_{ph}$  depends on the PZT ramping rate, then the interference signal will have the form  $\cos(\omega_{ph}t)$ . We will refer to this low frequency interference signal as the DC interference signal. When a strong pump beam at frequency  $\omega_p$ , is turned on and co-propagates with the signal beam inside the nonlinear waveguide, the signal beam experiences both nonlinear phase change and nonlinear absorption (with respect to the case when the strong pump beam is off) due to the presence of the pump. As a consequence, the interference signal out of the interferometer shifts in time and its amplitude is lower, as illustrated in Fig.20(a). As the strong pump beam is turned on and off (using a mechanical chopper for example) at a rate faster than the ramping of the PZT, the interference signal out of the interferometer alternates between the pump on and pump off curves, as illustrated in Fig.20(b) (solid curve). In actual measurements, only the alternating interference signal indicated by the solid line in Fig.20(b) is detected. By fitting two sinusoidal curves to this signal, for the cases when the pump is on and off, simultaneous measurement of the nonlinear refractive index  $n^{(2)}$  and the absorption coefficient  $\alpha^{(2)}$  experienced by the signal beam can be made. The amplitude change and phase shift between these two curves are then used to determine the values of  $\alpha^{(2)}$  and  $n^{(2)}$ , respectively. The nonlinear refractive index is given by  $n^{(2)} = \lambda\phi_{nl}/(2\pi F_s^{(2)} I_{eff} L)$ , where  $\lambda$  is the free space wavelength.

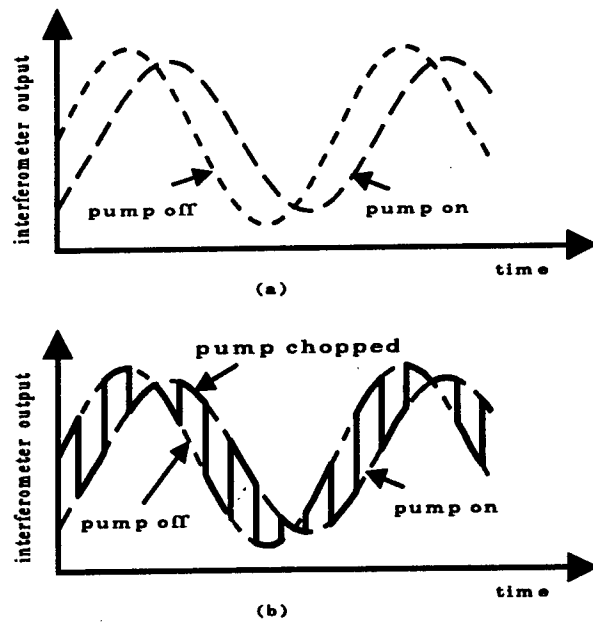


Figure 20: Illustration of Interference between Signal and LO as displayed by an oscilloscope for the cases when: (a) the pump is on (long dash) and off (tiny dash), and (b) the pump is chopped at a rate faster than the PZT ramping.

$\phi_{nl}$  is the measured nonlinear phase shift,  $I_{eff}$  is the effective peak pump intensity at the center of the transverse waveguide mode profile (it is simply the pump's peak intensity in the waveguide for the case of square pulse), and  $L$  is the length of the waveguide. The nonlinear absorption coefficient is given by  $\alpha^{(2)} = 2 \ln(A_{OFF}/A_{ON})/(F_s^{(2)} I_{eff} L)$ , where  $A_{ON}$  and  $A_{OFF}$  are the amplitudes of the fitted sinusoidal signals when the pump is on and off, respectively.

Using this scheme both the parallel and perpendicular components of  $n^{(2)}$  and  $\alpha^{(2)}$  can be measured. The parallel components  $n_{||}^{(2)}$  and  $\alpha_{||}^{(2)}$  are measured when the pump and signal beams entering the waveguide have the same polarization, while the perpendicular components  $n_{\perp}^{(2)}$  and  $\alpha_{\perp}^{(2)}$  are measured when the pump and signal beams have orthogonal polarizations. Different detection techniques are necessary to measure the parallel and perpendicular components of  $n^{(2)}$  and  $\alpha^{(2)}$ . The reason for this is the need to detect the DC interference between the signal and LO beams separately from the strong pump intensity. In the case when the pump and signal beams have orthogonal polarizations, the pump beam intensity can be easily separated from the signal and LO beams before detection with a polarization beam splitter. Measurement of  $n_{\perp}^{(2)}$  and  $\alpha_{\perp}^{(2)}$  are then obtained by detecting the

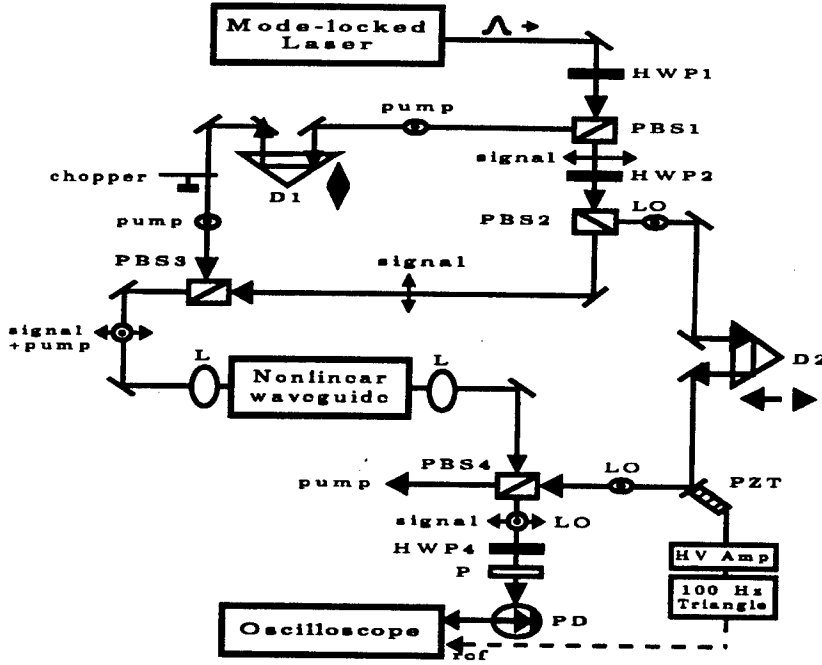


Figure 21: Schematic of the experimental set up to measure  $n^{(2)}$  and  $\alpha^{(2)}$  for the case when the pump and Signal beams have the same polarization.

DC interference between the signal and LO beams with an oscilloscope. In this case the pump and signal beams can have the same optical frequency. The measurement of  $n_{||}^{(2)}$  and  $\alpha_{||}^{(2)}$ , on the other hand, is more complicated because in this case the pump and signal beams have the same polarization and the two beams cannot be spatially separated before detection. One way to circumvent this problem is to frequency shift the pump beam, amplitude modulate the PSig beam, and select the beat signal between PSig and LO in the radio frequency domain using a RF spectrum analyser[37]. Since the RF spectrum analyzer displays the magnitude of signals, the intensity interference between the signal and LO beams would now have the form  $|\cos(\omega_{ph}t)|$  instead of  $\cos(\omega_{ph}t)$ . In the next section we describe in detail the experimental set up for measuring  $n_{\perp}^{(2)}$  and  $\alpha_{\perp}^{(2)}$  and also discuss the necessary changes in the set up for measuring  $n_{||}^{(2)}$  and  $\alpha_{||}^{(2)}$ .

Figure 21 shows a schematic of the experimental set up used for measuring  $n_{\perp}^{(2)}$  and  $\alpha_{\perp}^{(2)}$  in waveguides. The output of a mode-locked laser is split into two orthogonally polarized pump and PSig beams at the polarization beam splitter PBS1, with the pump power about

ten times higher than the PSig power (the amount of power split can be adjusted by the half-wave plate HWP1). Part of the PSig beam is split at the polarization beam splitter PBS2 and becomes the local oscillator (LO) beam. The orthogonally polarized pump and PSig beams are then spatially recombined (i.e. spatially overlapped but still orthogonally polarized) at the polarization beam splitter PBS3 and are subsequently coupled into the waveguide. After propagating through the waveguide, the pump and signal beams are recollimated and send through the polarization beamsplitter PBS4. At PBS4 the pump beam is spatially separated from the signal beam, while the signal beam and the LO beam are spatially recombined. Interference between the LO and the PSig beams is accomplished by passing the beams through the half-wave plate HWP3 and the polarizer P. As pointed before, the combination of PBS4, HWP3, and P is equivalent to the beam splitter BS2 in Fig.19. The phase of the LO beam is linearly varied at 100 Hz via a PZT and the resulting interference between the LO and PSig beams is detected by the photodiode PD and an oscilloscope. As the pump beam is chopped at a rate ( $\sim 1\text{ kHz}$ ) that is faster than the LO phase ramping (100Hz) the resulting interference signal between the PSig and LO beams alternates between the pump on and pump off states. Two sinusoidal curves are then fitted to the resulting interference trace, one for the pump on case and the other for the pump off case. As mentioned before, the amplitude change and phase difference between these two sinusoidal curves are proportional to  $\alpha_{\perp}^{(2)}$  and  $n_{\perp}^{(2)}$ , respectively. Thus, we see that by using this technique both  $n_{\perp}^{(2)}$  and  $\alpha_{\perp}^{(2)}$  can be determined simultaneously. As already discussed, the measurement of  $n_{\parallel}^{(2)}$  and  $\alpha_{\parallel}^{(2)}$  requires some modification in the experimental setup in order to frequency shif the pump beam (in the MHz range or higher) and to amplitude modulate the signal beam. The frequency shift of the pump beam is accomplished by inserting an acousto-optic modulator on the pump beam path, between PBS1 and PBS3, while the amplitude modulation of the signal beam is obtained by inserting a acousto-optical modulator in the signal beam path, between PBS2 and PBS3. The orthogonally polarized pump and signal beams are then spatially recombined at PBS3. The polarizations of the pump and PSig beams are then rotated by 45 degree using a half-wave plate and then the beams are send through a polarizer. After the polarizer, the combined pump and PSig beams have the same polarization, and are subsequently coupled into the waveguide. After going through the waveguide, the pump and PSig beams are send through PBS4, where they are spatially recombined with the orthogonally polarized LO

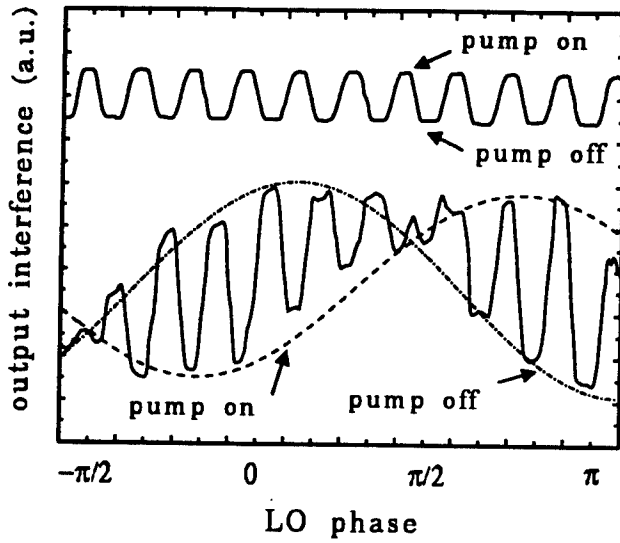


Figure 22: Nonlinear phase shift and nonlinear absorption data obtained in AlGaAs waveguide using this technique. The data is fitted with two sine envelopes for the cases where the pump is on (solid) and off (dashed). Measurement was made at an RF frequency of 200 kHz.

beam. Interference between the PSig and LO beams is accomplished by passing the beams through the half-wave plate HWP3 and the polarizer P, and it is detected by a photodiode and a spectrum analyser. We note that in this case the pump beam will also interfere with the LO beam. However, since the optical frequency of the pump beam has been shifted in the MHz range, the resulting beat signal between the pump and LO beams will also occur in the MHz range. By using a RF spectrum analyser the resulting interference signal between PSig and LO beams is then detected separately from the pump beam[37]. The signal of interest is the DC interference between the LO and PSig beams, which has two components: a slow sinusoidal component ( $\sim 100$  Hz) due to the amplitude interference between the PSig and LO beams, and a fast ( $\sim 200$  kHz) amplitude modulated component resulting from the amplitude modulation on the PSig beam. The spectrum analyzer is tuned to detect the kHz amplitude modulation component and displays the slow ( $\sim 100$  Hz) periodic interference between the PSig and LO beams. In this measurement, the pump beam is also chopped at a rate that is faster than the LO phase ramping, and two curves can be fitted to the data describing the cases when the pump is on and off. We recall that in this case the curves have the form  $|\cos|$ . The values of  $n_{\parallel}^{(2)}$  and  $\alpha_{\parallel}^{(2)}$  can then be obtained by using the same procedure as described for the perpendicular components.

We now present the results of our measurements of  $n_{\perp}^{(2)}$  and  $\alpha_{\perp}^{(2)}$  for a 1 cm long AlGaAs rib waveguide. An additive pulse mode-locked (APM) color-center laser (NaCl:OH) producing 430 fs pulses at 82 MHz repetition rate and with center wavelength at  $\lambda \sim 1.6 \mu\text{m}$ , was used in these experiments. The AlGaAs epitaxial layers were grown by molecular beam epitaxy (MBE) and consisted of a 5  $\mu\text{m}$  thick  $\text{Al}_{0.23}\text{Ga}_{0.77}\text{As}$  guiding region on top of a 2.5  $\mu\text{m}$  thick  $\text{Al}_{0.60}\text{Ga}_{0.40}\text{As}$  lower cladding layer grown on a semi-insulating GaAs substrate. The waveguides were patterned via photolithography and chemically etched using  $\text{H}_3\text{PO}_4:\text{H}_2\text{O}_2:\text{H}_2\text{O}$  (1:1:35 volume ratios). The height and width of the rib were 2  $\mu\text{m}$  and 4  $\mu\text{m}$ , respectively. The calculated fundamental mode cross-sectional area for this rib waveguide was 4.4  $\mu\text{m}$  by 2.6  $\mu\text{m}$ . Coupling of the laser pulses into and out of the waveguide was done by the end-firing coupling method and in order to minimize losses, both the front and back facets of the waveguide were antireflection coated. Figure 22 shows the interference data as displayed on an oscilloscope for the AlGaAs rib waveguide when the pump and signal have orthogonal polarizations. The solid curve corresponds to the intensity interference between PSig and LO beams and the two dashed curves are fitted sinusoidals representing the cases when the pump is on and off. The displacement between the two sinusoidal curves gives the nonlinear phase shift experienced by the signal due to the pump, and in this case it is approximately  $\phi_{nl} = 0.6 \pi$ . We also measure an 8% decrease in the amplitude of the sinusoidal curve for the pump on case, as compared to that of the pump off case. Using the relations previously described for  $n^{(2)}$  and  $\alpha^{(2)}$ , and estimating the pump power inside the waveguide to be 22 mW, we calculate a nonlinear refractive index  $n_{\perp}^{(2)} = 2.1 \pm 0.7 \times 10^{-14} \text{cm}^2/\text{W}$  and a nonlinear absorption coefficient  $\alpha_{\perp}^{(2)} = 0.06 \pm 0.02 \text{cm}/\text{GW}$ . In general, for isotropic materials like AlGaAs the effect of cross-phase modulation (XPM) is 2/3 as strong as that of self-phase modulation (SPM)[38]. Using this fact and comparing the values obtained here for  $n_{\perp}^{(2)}$  and  $\alpha_{\perp}^{(2)}$  with previously reported values[38, 39] of  $n_{\parallel}^{(2)} = 3.2 \times 10^{-14} \text{cm}^2/\text{W}$  and  $\alpha_{\parallel}^{(2)} = 0.08 \text{cm}/\text{GW}$ , respectively, we find that our results are in good agreement with them. As can be seen from Fig.23, the limit of detection for the induced phase shift is approximately  $\lambda/20$ . The accuracy of the data-fitting is approximately 10%. However, due to errors in the estimation of the pump power and mode area in the waveguide, we estimate that the overall accuracy in determining the nonlinear refractive index and absorption coefficient is probably not better than 35%.

One useful feature of this experimental technique is that it could be used for the determination of both the slow thermal component and the fast electronic component of  $n^{(2)}$ . The thermal component  $n_{thml}^{(2)}$  will be observed in the measurement of  $n^{(2)}$  if the thermal response time  $\tau_{thml}$  of the waveguide material is faster than the turn on time of the pump (*i.e.* the chopping rate of the pump beam is slower than  $1/\tau_{thml}$ ). Since the electronic component  $n_{elec}^{(2)}$  is proportional to peak power and the thermal component  $n_{thml}^{(2)}$  is proportional to the average power, it is possible to separate the effect of each other by reducing the pump's average power while keeping the pump peak power constant. By plotting the value of  $n^{(2)}$  as a function of the average pump power (peak pump power is kept constant), the value of  $n_{elec}^{(2)}$  could then be obtained from this plot in the limit where the average pump power goes to zero. In our experiment we measured the thermal response time of the AlGaAs waveguide and found that at  $\lambda \sim 1.6\mu\text{m}$ , for 430 fs pulses at 82 MHz rate,  $\tau_{thml}$  is about 2 seconds. For materials with long thermal response time like AlGaAs, it is possible to measure the electronic component  $n_{elec}^{(2)}$  by chopping the pump beam at a rate faster than the material's thermal response time. The value obtained for  $n_{\perp}^{(2)}$  actually corresponds to the electronic component of  $n_{\perp}^{(2)}$ . The sign of  $n_{elec}^{(2)}$  was determined by observing the direction of displacement of the DC interference signal when the pump was turned on, while at the same time observing the direction of the PZT expansion.

Figure 23 illustrates two traces: one is the interferometer output signal as function of time and the other is the PZT voltage as function of time. Here, the arrows indicate the direction in which the interference signal shifts as the pump is turned on for the cases of positive and negative  $n_{elec}^{(2)}$ . Using this method, we determined that for AlGaAs  $n_{elec}^{(2)}$  is positive. This is consistent with recent theoretical and experimental studies of semiconductor optical nonlinearities below the band gap energy[40].

We now describe a simpler way to measure the nonlinear absorption coefficient using the same experimental set up as shown in Fig. 21. In this case the nonlinear absorption coefficient is measured by first blocking the LO beam and detecting only the PSig using a detector and oscilloscope. In the absence of the pump beam, the oscilloscope displays the DC level of the PSig beam (*i.e.*, a straight line). When the pump is on, this DC level is reduced due to two-photon absorption of the PSig beam induced by the pump beam. As the pump beam is chopped at kHz rate, a periodic trace is obtained showing the PSig beam DC level

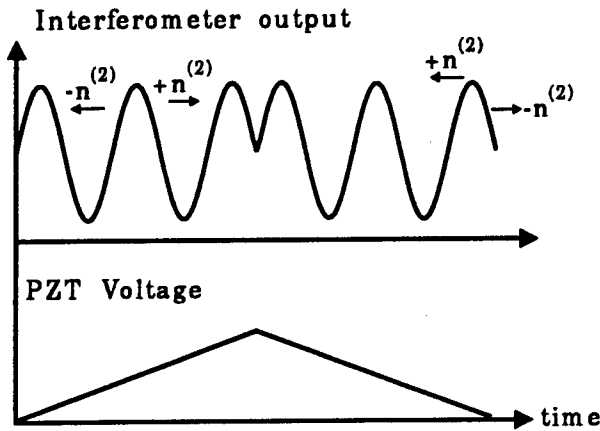


Figure 23: The upper trace show the interferometer output signal as function of time, while the lower trace indicates the PZT voltage as function of time. The arrows indicate the direction in which the interference signal shifts as the pump is turned on for the cases of positive and negative  $n_{elec}^{(2)}$ .

for the cases when the pump is on and off. Using this technique, we measured  $\alpha_{\perp}^{(2)}$  of the same AlGaAs semiconductor waveguide described before. Figure 24 shows the periodic trace resulting from two-photon absorption of the PSig beam. In this case, the nonlinear absorption coefficient is given by  $\alpha_{\perp}^{(2)} = -Ln[1 - (B_{OFF} - B_{ON})/B_{OFF}]/(F_s^{(2)} I_{eff} L)$ , where  $B_{ON}$  and  $B_{OFF}$  are the measured DC level of PSig for the cases of pump on and off, respectively. Estimating the average pump power inside the waveguide to be  $\sim 42$  mW, we calculate a nonlinear absorption coefficient  $\alpha_{\perp}^{(2)} = 0.065 \pm 0.02$  cm/GW, which is in good agreement with the value obtained before.

In a forward four-wave mixing (FWM) process a strong pump beam with frequency  $\omega_p$  interacts with a weak probe signal beam at frequency  $\omega_s$  in a  $\chi^{(3)}$  medium, generating a conjugate beam at frequency  $\omega_c = 2\omega_p - \omega_s$ . Although four-wave mixing measurements in waveguides have been reported in the literature, here we take advantage of our experimental set up used for  $n^{(2)}$  and  $\alpha^{(2)}$  measurements to also perform FWM measurements. This is quite convenient since, in the nearly-degenerate frequency region the four-wave mixing (FWM) gain coefficient  $X$  is related to  $n^{(2)}$  and  $\alpha^{(2)}$  by simple expressions. We can therefore use the results of FWM gain coefficient measurement to confirm the value of  $n^{(2)}$  or  $\alpha^{(2)}$ . The value of  $X$  can be determined from the magnitude of the conjugate and signal beams.

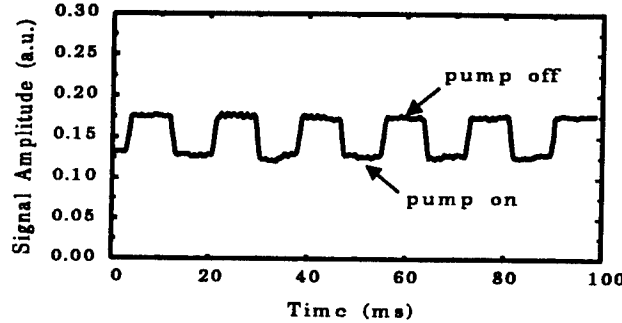


Figure 24: Trace of the direct measurement of nonlinear absorption for the case when the pump and PSig have orthogonal polarizations.

Figure 25 shows the experimental set up for FWM gain coefficient measurement. In describing this experiment we use the same nomenclature for pump, PSig and LO beams, as that for the measurement of  $n^{(2)}$  and  $\alpha^{(2)}$ . The pump, PSig and LO beams are obtained from the laser output beam in the same way as described in Fig. 21. However, in this experiment, the frequency of the PSig beam is shifted with respect to the frequency of the pump beam, so that the generated conjugate beam, PConj, will have a different optical frequency than that of the pump and PSig beams. This frequency shift is accomplished by passing the PSig beam through the acousto-optic modulator AO1. The orthogonally polarized pump and PSig beams are spatially recombined at the beamsplitter PBS3. After that the polarizations of the pump and PSig beams are rotated by 45 degrees using a half-wave plate and then the beams are sent through a polarizer P. The orientation of the polarizer is chosen so that when the pump and PSig beams are coupled into the waveguide they excite only the TM mode. The pump and PSig beams interact inside the  $\chi^{(3)}$  nonlinear waveguide, via the FWM process to generate a conjugate beam PConj. At the output of the waveguide, the pump, PSig, and PConj beams are recollimated and sent to the polarization beam splitter PBS4, where they are combined with the frequency shifted LO beam. Using a combination of a half-wave plate and polarizer P2, the pump, PSig, and PConj beams, respectively, interfere with the LO beam, generating three different RF beat signals that are detected using a photodiode and a RF spectrum analyzer (heterodyne detection of the pump, Psig, and PConj beams). We note that the frequency shift of the LO beam should be different than that of the PSig beam so that distinct RF beat signals are obtained. In addition, the amount of frequency shift is chosen so that the RF beat signals occur away from the harmonics of the mode-locked

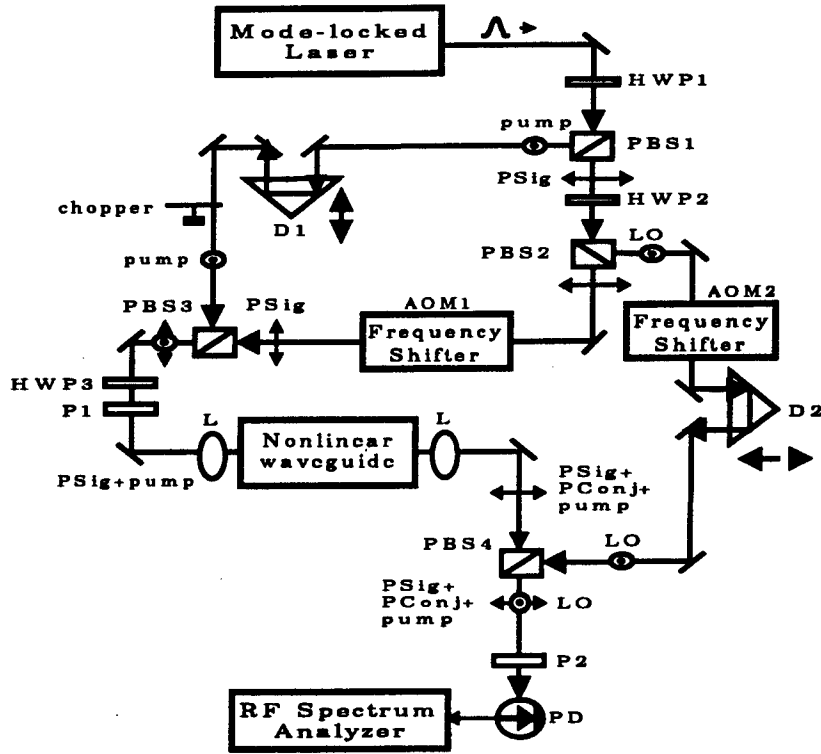


Figure 25: Schematic of the experimental setup to perform four-wave mixing measurement.

laser frequency. Figure 26(a) shows the optical frequency of the various beams involved in this experiment. Both the PSig and LO beams were frequency shifted with respect to the pump beam. PSig, at frequency  $\omega_s$ , was up-shifted by 27 MHz, and the LO beam, at  $\omega_{LO}$ , was down-shifted by 50 MHz. Through the four-wave mixing process, the conjugate beam PConj, at  $\omega_c$ , was generated at  $-27$  MHz. As indicated in the diagram a second LO signal at  $\omega'_{LO}$  arises from the pulse repetition rate of the mode-locked laser and differs in frequency from the LO at  $\omega_{LO}$  by 82 MHz.

Figure 26(b) shows the expected beat signals in the RF domain with the beating components indicated above each arrow. Basically, it shows that the 5 MHz signal corresponds to the beating between PSig at  $\omega_S$  and LO at  $\omega'_{LO}$ , the 23 MHz signal corresponds to the beating between PConj at  $\omega_C$  and LO at  $\omega_{LO}$ , and the 32 MHz signal corresponds to the beating between the pump and the second LO signal (dashed). The 27 MHz signal represents two beating signals: one between the pump and the PSig and the other between the pump

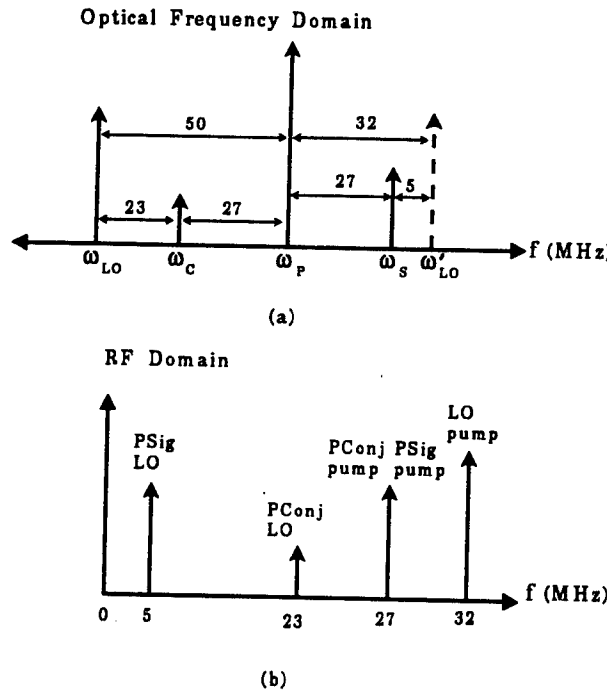


Figure 26: (a) Optical frequency spectrum of the various beams involved in the four-wave mixing experiment, indicating the frequency shift of the LO, PSIG, and PConj signals with respect to the pump beam; (b) the expected RF beat spectrum in the FWM experiment, with the beating components indicated above each arrow.

and PConj. Using the experimental set up described in Fig. 25 we measured the FWM gain coefficient  $|X|$  of the AlGaAs rib waveguide. Figure 27 shows RF the spectrum resulting from the FWM measurement for the case when the pump and PSig beams have the same polarization. The conditions for the pulse width, pulse center wavelength, and repetition rate were identical to those used for the  $n^{(2)}$  and  $\alpha^{(2)}$  measurement. As can be seen from Fig. 27, the magnitude of the PConj signal at 23 MHz is about 1/4 of the magnitude of the PSig signal at 5 MHz. As mentioned before, the FWM gain coefficient can be obtained by reading the relative magnitudes of the PSig and PConj fields from the RF spectrum analyzer. Using the estimated values of pump power = 2.4 mW, and the mode area of  $4.5 \mu\text{m}$  by  $2.7 \mu\text{m}$  we calculate the four-wave mixing gain coefficient to be  $|X| = 8.55 \times 10^{-10} \text{ cm/W}$ . Since  $X$  is directly related to  $n_{elec}^{(2)}$  and  $\alpha^{(2)}$ , it can be used to calculate independently either  $n_{elec}^{(2)}$  or  $\alpha^{(2)}$ . Using the value obtained for  $|X|$  from the FWM measurement and  $\alpha^{(2)} = 0.08 \text{ cm/GW}$  we obtain a value of  $n^{(2)} \sim 2.17 \times 10^{-14} \text{ cm}^2/\text{W}$ , which is close to the value obtained earlier

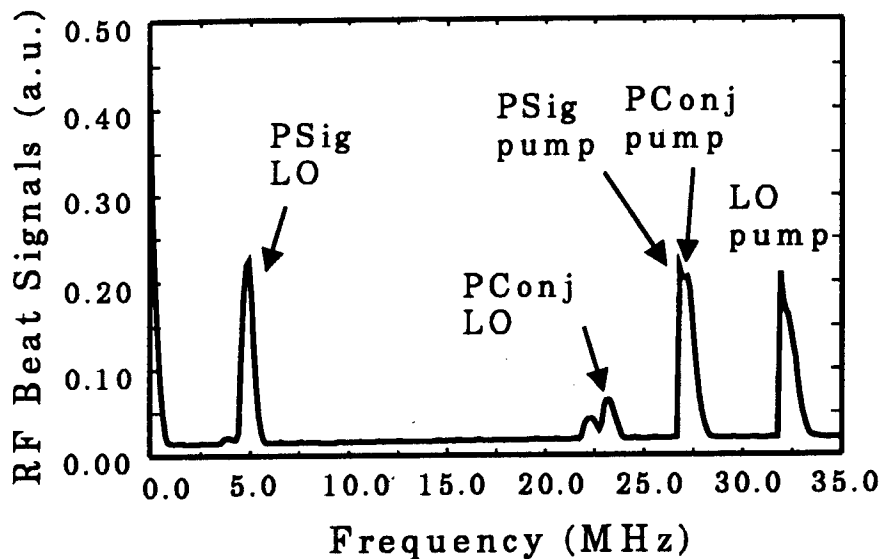


Figure 27: RF beat signal spectrum resulting from the four-wave mixing experiment in AlGaAs waveguide using 430 fs pulses at  $\lambda=1.6\mu\text{m}$ .

using the simultaneous measurement (note that in that case the pump and probe had orthogonal polarizations). We also measured the FWM gain coefficient for the case when the pump and Psig have orthogonal polarizations. In this case, however, the gain coefficient was very small, approaching zero.

### **3.B Dispersion Compensation, Stable Soliton Propagation and Regeneration, and Pulse Shaping**

The goals of this part of the research were:

1. to demonstrate the bit-rate/distance product improvement achievable with dispersion compensation,
2. to demonstrate that solitons can propagate over ultralong distances without generating dispersive radiation,
3. to demonstrate soliton regenerators as alternatives to optical amplifiers, and
4. to demonstrate optical pulse shaping for improved switching performance.

Below we describe the research performed towards achieving the above goals. Along the way we discovered some new properties of PSA's, such as their use in soliton storage rings. Details of these discoveries are also given in the following.

#### **3.B.1 Dispersion Compensation Experiments**

We proposed a novel approach to combating the pulse broadening effect of group-velocity dispersion (GVD) in a fiber-optic communication link, which relies on the use of PSA's to amplify and shape the short pulses propagating in the fiber [13].

Our initial attempt to measure the dispersion compensation property of PSA's was unsuccessful because of the excessive phase fluctuations on our Nd:YLF laser. We worked on stabilization of the Nd:YLF laser using the Pound-Drever-Hall technique. Figure 28 shows a block diagram of the setup to stabilize the laser and Fig. 29 shows the resulting error signal. With the Nd:YLF laser stabilized we were able to observe phase-sensitive gain with delayed pulses. Gain with delayed pump pulses is necessary for the dispersion compensation property to work and be useful. However, experiments to demonstrate the dispersion compensation property of PSA's were not conclusive due to the phase noise that still remained on the grating pair that was used to introduce dispersion.

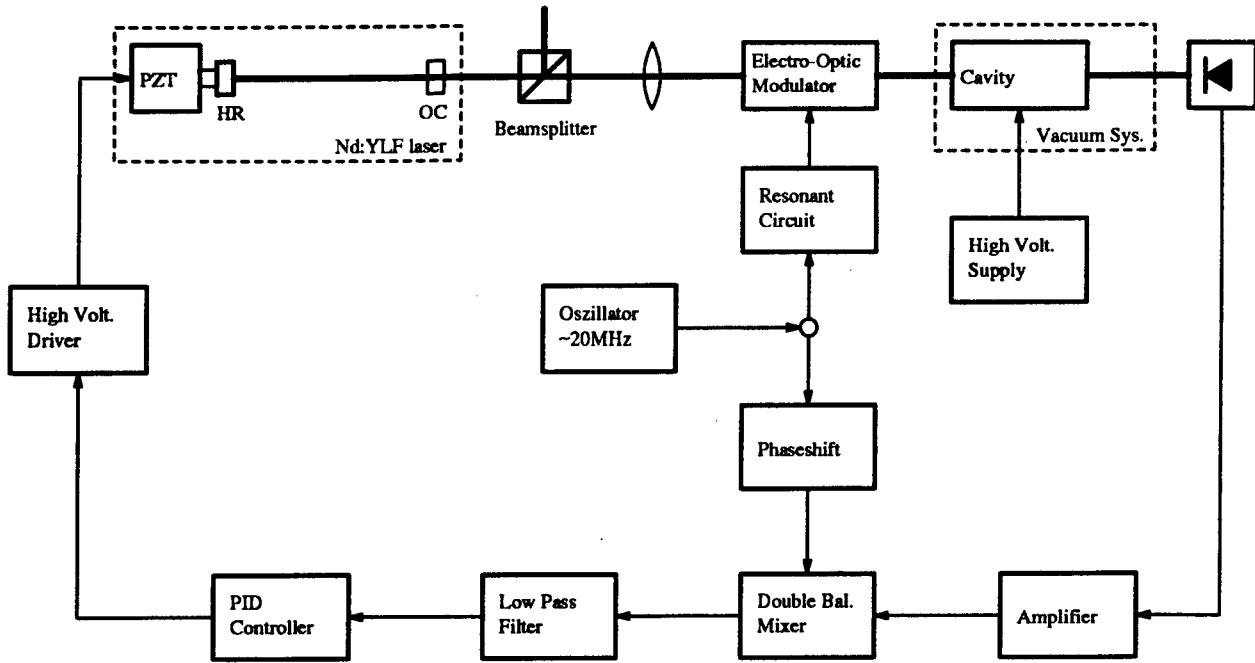


Figure 28: Block diagram of the stabilization system for the Nd:YLF laser. It differs from the Pound-Drever-Hall technique insofar as the light is transmitted through the reference cavity rather than reflected off of it.

### 3.B.2 Stable Soliton Propagation: Compensation of Soliton Self-Frequency Shift with PSA's

When short soliton pulses propagate in an optical fiber, physical effects lead to higher-order perturbations which modulate the pulses' shape, velocity and frequency. These effects include the Raman self-frequency shift, third order dispersion, and nonlinear dispersion. For typical communication and network applications, the most important of these is the Raman self-frequency shift, because it leads to a continuous downshift of the soliton frequency and a continuous deceleration of the pulse [48, 49]. The effects of the Raman downshift accumulate as the pulse propagates down the fiber, so this effect becomes progressively more important as the propagation distance increases. On the other hand, it is well known [50] that higher-order dispersion simply leads to a constant velocity change of the pulse.

Recently, PSA's have been proposed as an alternative to EDFA's in optical transmission networks [51, 52]. Such amplifiers have been shown to suppress dispersive soliton radiation [52] as well as reduce Gordon-Haus jitter [53]. During this budget period we have

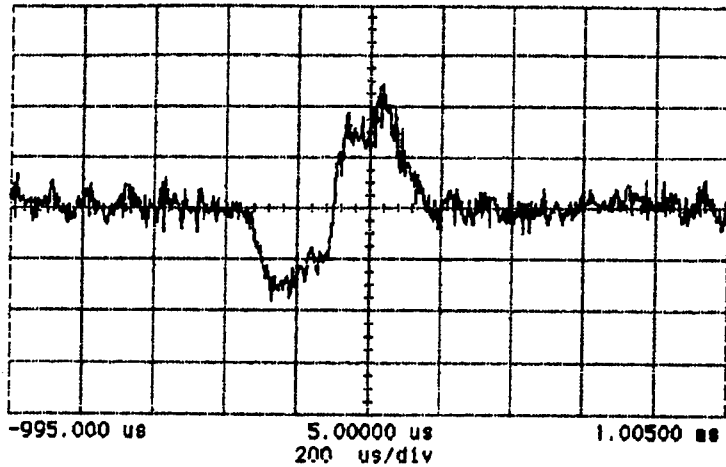


Figure 29: Amplified error signal. The cavity was scanned at a rate of approximately 40 MHz/ms and the bipolar error signal created by one laser mode observed on an oscilloscope. The symmetry point corresponds to the cavity resonance. Horizontal: 0.2 ms/div; Vertical: 0.1 V/div.

shown that the PSA's also compensate the Raman self-frequency shift [14].

The basic equation for the pulse amplitude in the slowly-varying envelope approximation is the nonlinear Schrödinger equation (NLS). Including the higher-order physical effects and periodic phase-sensitive amplification leads to the perturbed equation,

$$\begin{aligned} \frac{\partial q}{\partial Z} = & \frac{i}{2} \frac{\partial^2 q}{\partial T^2} + i|q|^2 q + \frac{1}{\epsilon} h \left( \frac{Z}{\epsilon} \right) q + \frac{1}{\epsilon} f \left( \frac{Z}{\epsilon} \right) q^* \\ & - i\sigma_r q \frac{\partial}{\partial T} |q|^2 - \beta_3 \frac{\partial^3}{\partial T^3} q - \beta_{nl} \frac{\partial}{\partial T} |q|^2 q. \end{aligned} \quad (1)$$

Here  $T$  is the physical time divided by the pulse width  $\tau$  (FWHM),  $q$  is the field envelope divided by the peak-field amplitude  $E_0$ , and  $Z$  is the physical distance divided by the dispersion length  $Z_0$ . The higher-order coefficients are given by [54]

$$\sigma_r = \frac{1.76 T_r}{\tau}, \quad \beta_3 = -\frac{1.76 k'''}{6|k''|\tau}, \quad \beta_{nl} = \frac{2 \times 1.76}{\omega_0 \tau}, \quad (2)$$

where  $T_r$  is the Raman time constant,  $k''$  and  $k'''$  are the second and third order dispersion coefficients, and  $\omega_0$  is the carrier frequency.

We considered short soliton pulses ( $\tau = 1$  ps) at a wavelength of 1.55  $\mu\text{m}$  propagating in a dispersion-shifted fiber with  $k'' = -0.1 \text{ ps}^2/\text{km}$ . This resulted in a dispersion length of only 3.228 km. The amplifier spacing was chosen 1 km; such closely spaced nodes would be suitable for local, high-speed optical networks [55]. For a typical fiber, where the loss is on

the order of 0.25 db/km, the line is essentially lossless over such short distances. Therefore, we neglected the line loss between the amplifiers and included only the lumped loss at each node.

Following Kutz *et al.* [52], we performed a multiple-scale expansion of Eq. (1) and showed that amplification with PSA's produces a stable, steady-state pulse which moves with a small constant inverse velocity in the group-velocity rest frame [14]. This inverse velocity depends linearly on the amplitude of the perturbations and is thus inversely proportional to the pulse width. We remark that this is the expected result for the third-order and nonlinear dispersion [50], so that the PSA's are effectively transparent to these terms. On the other hand, the Raman downshift has been neutralized. Instead of a continuous frequency downshift, and a corresponding deceleration of the pulse, the downshift stabilizes and the pulse propagates with a constant velocity. This is because the PSA's act as a restoring force in frequency, constraining the pulse to remain near its initial carrier frequency.

We compared these results for a PSA line with those for a line amplified with EDFA's. We chose  $k''' = 0.01 \text{ ps}^3/\text{km}$ ,  $T_r = 5 \text{ fs}$ , and assumed that half of the pulse amplitude is tapped off at each amplifier node, so that  $F = 0.5$  (25% loss). For the PSA's, we chose an overamplification of  $\Delta\alpha = 0.1$  (a small amount of overamplification, represented by  $\Delta\alpha$ , is necessary for the stability of the PSA line). For the EDFA line, the gain was chosen to exactly balance the loss.

We first examine the effects of the higher-order dispersive terms; typical pulse propagation is shown in Fig. 30. For the above parameters, our theoretical analysis predicted an inverse velocity of 7.50 fs/km, which agreed well with the result of a numerical simulation of Eq. (1) of 7.10 fs/km. By comparison, the EDFA line showed an inverse velocity of 5.74 fs/km. We next examined the effect of the Raman downshift, shown in Fig. 31. The constant inverse velocity for the PSA line is clearly evident in this figure, and the numerical value of 0.176 fs/km agrees well with the inverse velocity predicted by our theory of 0.174 fs/km. This leads to a time shift of less than 70 fs over 120 soliton periods, as opposed to a time shift of 19 ps over the same distance in a line with EDFA's.

The frequency downshift can also be measured, and it is shown in Fig. 32. After a short transient, the frequency downshift in the PSA line stabilizes at  $\delta\nu = 0.350 \text{ GHz}$ . By comparison, a 1 ps pulse travelling down the line with EDFA's undergoes a downshift of

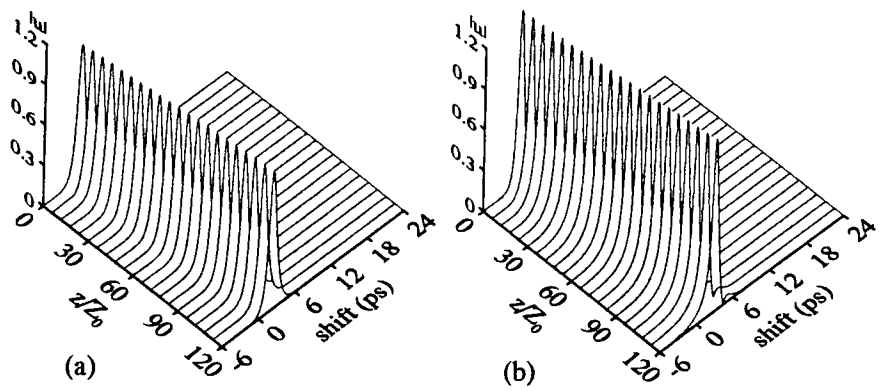


Figure 30: Propagation of a 1 ps pulse, including the effects of higher-order dispersion, in a line with periodic (a) EDFA's and (b) PSA's.

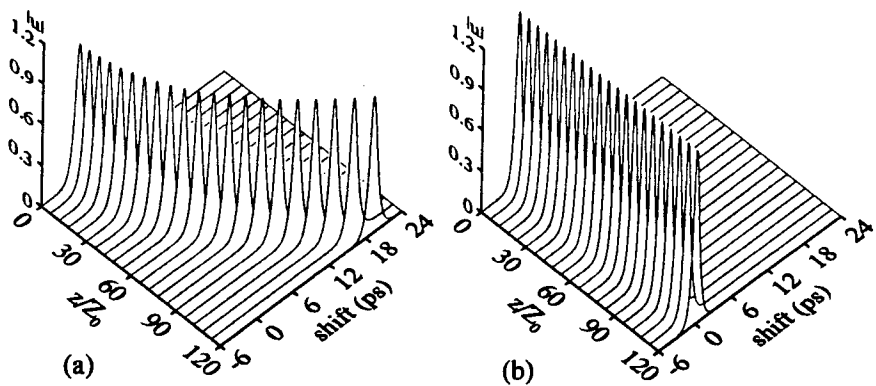


Figure 31: The effect of the Raman self-frequency shift on a 1 ps pulse in a line with periodic (a) EDFA's and (b) PSA's.

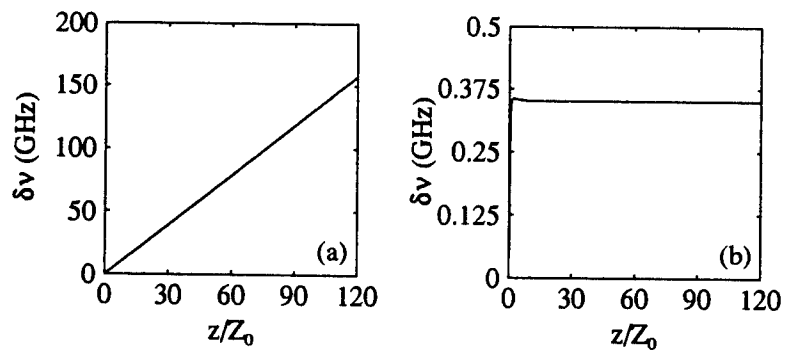


Figure 32: Frequency shift induced on a 1 ps pulse with periodically spaced (a) EDFA's and (b) PSA's.

0.407 GHz/km, for a total shift of 157 GHz after 120 dispersion lengths. Thus the total frequency downshift using PSA's is less than the downshift per kilometer in the EDFA line.

### 3.B.3 Stable Soliton Propagation: Periodic Amplification and Conjugation of Solitons

The use of optical phase conjugation for the compensation of the effects of chromatic dispersion on a linear pulse was first proposed by Yariv *et al.* [56], who showed that a single phase conjugation at the fiber midpoint can reverse any accumulated dispersive effects during the subsequent pulse propagation. Similarly, self-phase modulation is compensated by midpoint optical conjugation [57]. These results can be easily understood in terms of the NLS equation for the pulse envelope, for which phase conjugation corresponds to reversing the direction of propagation.

It has recently been shown that midpoint optical phase conjugation is also effective in optical soliton transmission systems to compensate for soliton-soliton interactions [58], Gordon-Haus jitter [59], and the Raman self-frequency shift [60]. If the pulse is frequently amplified to balance the linear fiber loss, propagation will occur in the guiding-center soliton regime [50], and the propagation-reversing property of optical conjugation for NLS solitons can be used to show that distortion of the pulse is compensated by a single conjugation.

During this budget period, we have proposed periodic phase conjugation with amplification of optical solitons [15]. Pulses amplified via four-wave mixing with gain, as recently demonstrated by Zhou *et al.* [61], are simultaneously amplified, phase-conjugated, and frequency converted. We considered periodic lumped amplification and conjugation of a pulse with carrier frequency  $\omega_0$ . At an amplifier, a frequency component at  $\omega_0 + \delta\omega$  is converted to  $\omega_0 - \delta\omega$ ; it is then converted back at the next amplifier. Unlike midpoint conjugation, the periodic conjugation occurs on a lengthscale which is short compared to the loss length, and pulse propagation no longer occurs in the guiding-center regime.

We concentrated on short pulses, for which third-order dispersion, nonlinear dispersion (self-steepening) and Raman scattering become important. For such pulses, the basic envelope evolution equation is

$$\frac{\partial q}{\partial Z} = \frac{i}{2} \frac{\partial^2 q}{\partial T^2} + i|q|^2 q - i\sigma_r q \frac{\partial}{\partial T} |q|^2$$

$$-\gamma q - \beta_3 \frac{\partial^3}{\partial T^3} q - \beta_{\text{nl}} \frac{\partial}{\partial T} |q|^2 q. \quad (3)$$

Here  $\gamma$  is the linear fiber-loss coefficient and the remaining variables and the parameters are the same as those in Eq. (1). We considered short pulses ( $\tau = 0.5$  ps) at a wavelength of  $1.55 \mu\text{m}$ . Since the pulse is periodically conjugated, we also considered the conjugate equation,

$$\begin{aligned} -\frac{\partial q^*}{\partial Z} = & \frac{i}{2} \frac{\partial^2 q^*}{\partial T^2} + i|q|^2 q^* - i\sigma_r q^* \frac{\partial}{\partial T} |q|^2 \\ & + \gamma q^* + \beta_3 \frac{\partial^3}{\partial T^3} q^* + \beta_{\text{nl}} \frac{\partial}{\partial T} |q|^2 q^*. \end{aligned} \quad (4)$$

With  $\gamma = 0$ ,  $\beta_3 = 0$ , and  $\beta_{\text{nl}} = 0$ , Eq. (4) is identical to Eq. (3) with  $q \rightarrow q^*$  and  $Z \rightarrow -Z$ , so the conjugation reverses the direction of propagation of the pulse. Any pulse evolution due to self-phase modulation, second-order dispersion and Raman scattering which occurs between one pair of amplifiers will be reversed as the pulse travels between the next pair. The effects of these terms can accumulate at most over a single amplifier spacing, not over the entire propagation distance, so they are compensated by the periodic conjugation.

Periodic conjugation also compensates for the Gordon-Haus jitter, which is the largest source of timing jitter when EDFA's are used. Amplifier-induced frequency noise causes a mean-square velocity shift in the solitons that is converted to timing jitter as the pulse propagates. If this shift is uncompensated, the timing jitter accumulates over the total propagation length,  $L$ , and the mean-squared timing jitter is proportional to the cube of the propagation length [62],

$$\langle \delta t^2 \rangle = \frac{L^3}{3z_a} \langle \delta \Omega^2 \rangle, \quad (5)$$

where  $z_a$  is the amplifier spacing and  $\langle \delta \Omega^2 \rangle$  is the noise-induced mean-square velocity shift. This sets a limit on the propagation length, since large timing shifts will lead to bit errors when a pulse leaves its timing window.

With periodic phase conjugation, however, the most the shift can accumulate is a single amplifier spacing, so the mean-square timing shift from the Gordon-Haus jitter increases linearly with the propagation length:

$$\langle \delta t^2 \rangle = \frac{Lz_a}{2} \langle \delta \Omega^2 \rangle. \quad (6)$$

Thus, in the absence of other effects, periodic phase conjugation greatly reduces the Gordon-Haus jitter; this result is similar to that for sliding-guiding filters [63] or PSA's [64]. By

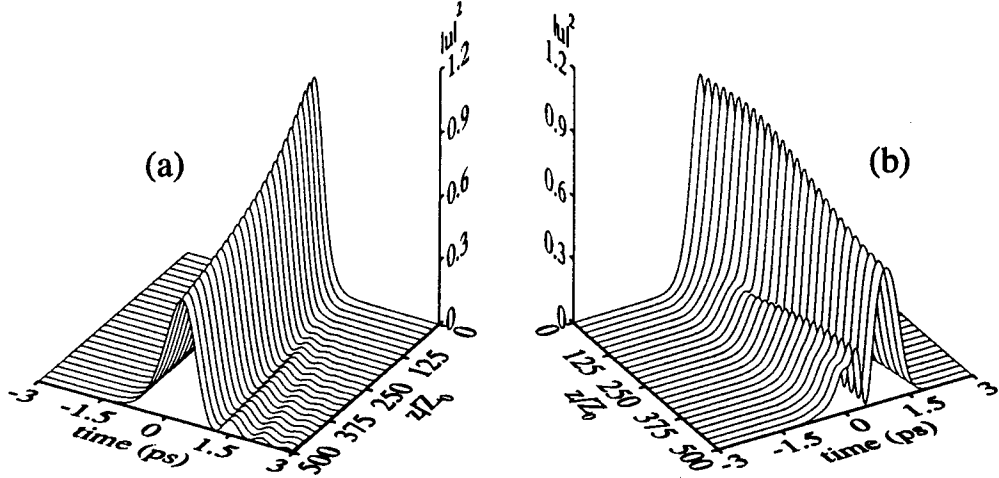


Figure 33: Propagation of a 0.5 ps pulse, including the effects of Raman scattering, in a lossless line with periodic phase-conjugating amplifiers showing the effect of (a) third-order dispersion and (b) nonlinear dispersion.

comparison, a single optical conjugation reduces the Gordon-Haus jitter by a factor of two or three, depending on whether the conjugation is done at the midpoint or the two-thirds point of the fiber [59].

To illustrate the effects of the higher-order dispersions and the linear fiber loss, we present numerical simulations of the evolution of a hyperbolic secant initial pulse with  $\tau = 0.5$  ps over 500 dispersion lengths. We chose low dispersion fiber,  $k'' = -0.1$  ps<sup>2</sup>/km, so that the dispersion length is  $Z_0 = 0.807$  km, and we included the Raman term with  $T_r = 5$  fs. All figures were generated by integrating Eq. (3) with periodic phase-conjugating amplifiers with the amplifier spacing equal to the dispersion length.

We first assumed a lossless line,  $\gamma = 0$ , and considered the third-order and nonlinear dispersions separately. Figure 33(a) shows the pulse evolution with  $\beta_3 = -2.89 \times 10^{-3}$  (corresponding to  $k''' = 4.93 \times 10^{-4}$  ps<sup>3</sup>/km) and  $\beta_{nl} = 0$ . Since the second-order dispersion and self-phase modulation are compensated by the periodic conjugation, the evolution is nearly identical to a solution of the linear, third-order dispersion equation

$$\frac{\partial q}{\partial Z} = -\beta_3 \frac{\partial^3}{\partial T^3} q. \quad (7)$$

Without the nonlinearity or second-order dispersion, third-order dispersion dominates the evolution, and the pulse continuously loses energy to dispersive radiation.

Inclusion of the nonlinear dispersion yields similar results. If we take  $\beta_3 = 0$  and  $\beta_{nl} =$

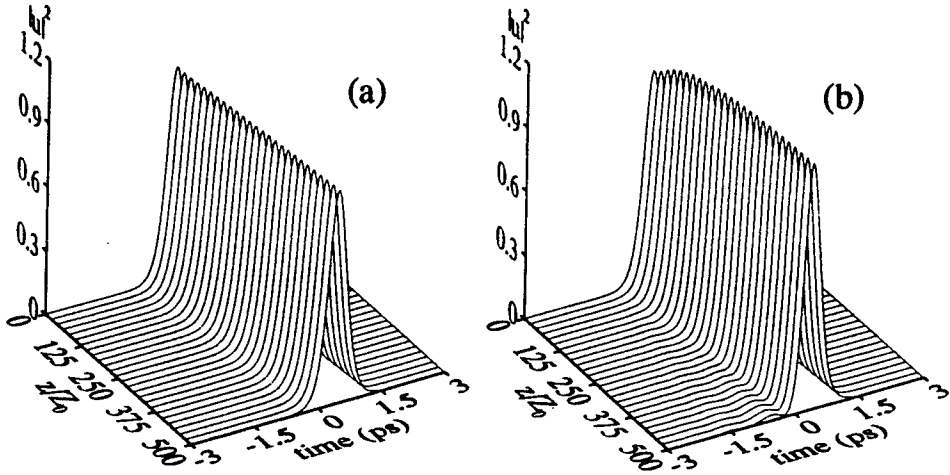


Figure 34: Propagation of a 0.5 ps pulse, including the effects of higher-order dispersion and Raman scattering, in a line with periodic phase-conjugating amplifiers. The third-order and nonlinear dispersion have been balanced so that  $\beta_{nl} = 2\beta_3$ . (a) Lossless line. (b) Linear loss of 0.15 dB/km.

$5.79 \times 10^{-3}$  (corresponding to  $\omega_0 = 1.22 \times 10^{15} \text{ s}^{-1}$ ), the pulse evolution, shown in Fig. 33(b), is nearly identical to a solution of the nonlinear equation

$$\frac{\partial q}{\partial Z} = -\beta_{nl} \frac{\partial}{\partial T} |q|^2 q. \quad (18)$$

In this case the self-steepening dominates, causing the pulse to split as it evolves down the fiber.

These two examples show that the periodic conjugation neutralizes the effects of the second-order dispersion, the self-phase modulation, and the Raman scattering. The compensation is not exact, however, since the higher-order terms perturb the shape of the pulse. This interaction is minimized in this example because the initial condition is an NLS soliton, and the second-order dispersion and self-phase modulation balance between the amplifiers. A different initial condition would have a varying profile between amplifiers, enhancing the interaction between the higher-order terms and the second-order dispersion and self-phase modulation. Choosing an NLS soliton as the initial condition allowed the second-order dispersion and self-phase modulation to be compensated on average.

Consideration of Eqs. (7) and (8) shows that the third-order and nonlinear dispersion can be balanced to give higher-order soliton solutions if one chooses  $\beta_{nl} = 2\beta_3$ . This requires  $k''' < 0$ ; such materials have been recently studied [65]. Fig. 34(a) illustrates how this balance restores the solitary wave propagation. It should be noted that the parameters in Fig. 34(a)

are the same as those used in Fig. 33 with the exceptions that the third-order and nonlinear dispersions are both included and the sign of the third-order dispersion is reversed.

This parameter balance is necessary to preserve the amplitude/width ratio of the original soliton solution. It is important to remember that the second-order dispersion and self-phase modulation are still present, and are only compensated in an averaged sense. These terms interact with the higher-order terms during pulse propagation. It is necessary to choose the amplitude so that the second-order dispersion and self-phase modulation balance during the propagation between amplifiers, or the interaction with the higher-order terms will destroy the average compensation.

The last remaining term is the linear fiber loss. Using a loss of 0.15 dB/km results in a loss length of 57.9 km and  $\gamma = 0.0139$ . The pulse is amplified frequently over one loss length, so the effect of the loss is minimal, as seen in Fig. 34(b). Work to understand the perturbations induced by the loss and to incorporate the effects of amplifier noise is underway.

### **3.B.4 Long-Term Storage of a Soliton Bit Stream using PSA's: Effects of Soliton-Soliton Interactions and Quantum Noise**

Recently we have shown that stable soliton-like pulse propagation over ultra-long distances is possible in a nonlinear fiber line in which linear loss is balanced by periodic phase-sensitive (parametric) amplification [51, 52]. In such a line the length scale over which pulse evolution occurs is significantly increased beyond a soliton period because the amplifiers attenuate phase variations across a pulse's profile. Through analytical and numerical studies we showed that in the stable parameter region the pulse evolution occurs on length scales that are much longer than the soliton period. Numerical results indicated that with a proper choice of parameters pulses could propagate over physical distances that are over  $10^5$  kilometers long [51, 52]. In fact, in principle, within the stability region pulses can travel an infinite distance. Equivalently, in a re-circulating loop pulses can be stored indefinitely [64]. Such a loop can then serve as a memory element for use in ultra-high-speed optical networks [66]. This conclusion, however, is based on an analysis which ignored the effects of soliton-soliton interactions, the quantum fluctuations introduced by the loss in the line (note that the parametric amplifiers do not add any noise), and the effects of guided acoustic-wave Brillouin scattering (GAWBS) [67, 68].

During this budget period we have included such pulse interaction and noise effects in the context of a storage ring for a bit stream of soliton-like pulses [16]. We showed that the PSA significantly enhances the stability properties of the fiber storage ring, as compared to the case when a PIA (such as an EDFA) is used. The one's (the soliton pulses) have asymptotically stable intensity while the noise on the zero's of the bit stream (where the solitons are absent) is bounded. Moreover, we demonstrated that the effects of soliton-soliton interactions and noise-induced pulse timing jitter are substantially reduced by the PSA. This is similar to the reduction of the soliton self-frequency downshift by PSA's that was shown in Sec. 3.B.2 [14]. We also showed that the residual effects due to soliton-soliton interactions and quantum noise can be eliminated by using a pulsed pump (gain modulation) to drive the PSA.

As an example we considered a 3 km long loop made out of a dispersion-shifted fiber having  $|\beta''| = 0.2 \text{ ps}^2/\text{km}$  and  $\gamma = 0.017 \text{ km}^{-1}$  (0.15 dB power loss per km). If such a ring is used to store streams of bits with a period of 10 ps [bit rate of 100 gigabits/s with one's represented by 3.5 ps (FWHM) pulses (or, hyperbolic secant width  $\tau \approx 2 \text{ ps}$ ) and zero's by the absence of pulses], then the dispersion and loss lengths,  $z_0 \equiv \tau^2/|\beta''| = 20 \text{ km}$  and  $z_\gamma \equiv 1/2\gamma = 29.4 \text{ km}$ , respectively, are much longer than the loop length, thus satisfying the distributed amplification condition. For these parameters the ring would have a storage capacity of 1.5 megabits and can be built using a fiber PSA [69] as shown in more detail in Fig. 35.

We point out here that the fiber/PSA storage ring shown in Fig. 35 can be optically loaded. Moreover, this can be accomplished in a manner that is independent of the phase of the arriving pulse stream, thereby alleviating the need for phase coherence between the arriving and stored pulses. In our scheme, the signal pulses are loaded into the storage loop by imbalancing the Sagnac loop of the PSA with the phase shift caused by cross-phase modulation (XPM) of the pump pulses with the arriving signal pulses. Since the XPM interaction is phase insensitive, the signal pulses do not need to be in phase with the pump pulses as they are loaded; rather an in-phase copy of each signal pulse is made from the pump pulse as the latter enters the fiber PSA. When a zero arrives, no XPM occurs and no pulse is injected into the ring. As a result, this device is compatible with WDM networks.

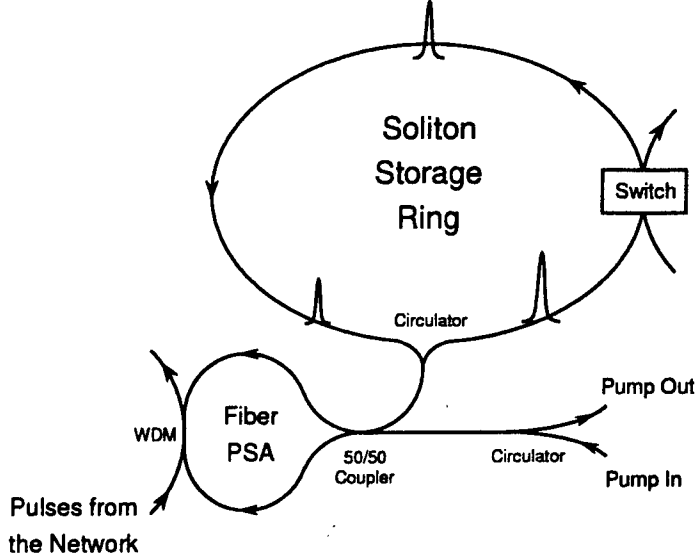


Figure 35: A physically realizable optical storage ring using a fiber PSA [69], WDM = wavelength-dependent coupler.

**Soliton-Soliton Interactions:** We used soliton perturbation theory along with numerical simulations of the NLS equation to analyze the soliton-soliton interactions [16]. Our analysis showed that the use of PSA's automatically controls the soliton-soliton interaction effects. Moreover, by inserting additional lumped loss during each round-trip cycle, e.g., by tapping off a portion of the signal just before it enters the PSA, the interaction effects are substantially reduced. Figure 36 gives the results of numerical computations showing the reduction of the interaction effects. The figure also includes the result for the case when gain modulation is added to the system. In this case it is seen that all of the residual soliton interaction effects have been eliminated.

**Pulse Propagation in the Presence of Noise:** We used soliton perturbation theory along with numerical simulations of the NLS equation to analyze the effects of quantum noise introduced by the loss in the fiber (the PSA's are noiseless). The main effects of the noise are the soliton timing jitter (Gordon-Haus effect) and the photon-number fluctuations.

The effect on the timing jitter is shown in Fig. 37(left) for different values of  $\theta_0$ , the phase of the soliton relative to that of the amplifier. These plots were generated by numerically solving the NLS equation, along with the noise terms due to loss, repeatedly with identical initial conditions. The timing variance was obtained from the pulse position data of 400

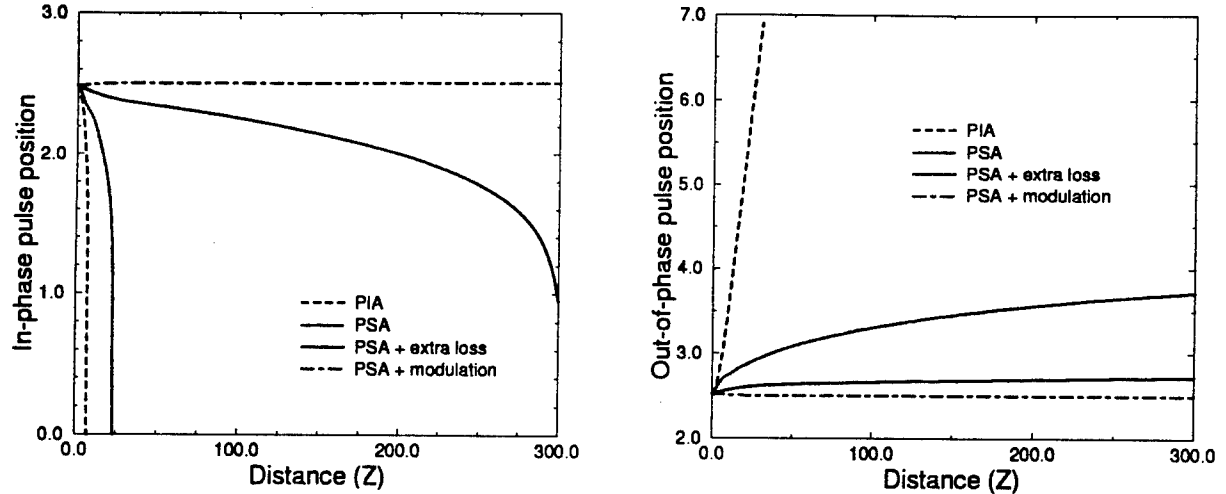


Figure 36: Numerical solution of the two-soliton interaction for different amplifier configurations, showing the normalized position of one of the two solitons as a function of distance (measured in dispersion lengths). The results are given for PIA's, PSA's, PSA's + added lumped loss, and PSA's + lumped loss and gain modulation. The initial pulsewidth was  $\tau_0 = 2$  ps. For the PIA case the gain was chosen to exactly compensate the loss. For PSA's + added loss, the field was attenuated by  $\exp(-0.5)$  before each amplifier. For PSA's + gain modulation, the same extra loss factor was used, but the gain was modulated sinusoidally (10 ps period, 10% modulation). The left (right) plot is for in-phase (out-of-phase) interaction.

runs resulting in a relative statistical uncertainty of approximately 7%.

Note that the variance in Fig. 37(left) is clearly growing linearly with distance, in contrast to the case with PIA's wherein the noise grows cubically with distance [62]. The computed variances are also in good quantitative agreement with the theoretical results: for  $\theta_0 = 5^\circ$ , after 2800 km, theory gave a renormalized variance of  $2.7 \times 10^{-4}$  (i.e., renormalized with respect to the initial pulse width  $\tau_0 = 2$  ps), while the numerical solution gave  $2.5 \times 10^{-4}$ ; for  $\theta_0 = 10^\circ$  these numbers were  $2.2 \times 10^{-4}$  and  $1.9 \times 10^{-4}$ , and for  $\theta_0 = 22^\circ$  they were  $1.4 \times 10^{-4}$  and  $1.2 \times 10^{-4}$ . Recall that for this choice of distance the normalized timing variance when PIA's are used should be unity. Thus phase-sensitive amplification is seen to significantly reduce the timing jitter. Note also that although the discrepancy between the theoretical and the numerical results is small (it increases with increasing  $\theta_0$ ), we think it to be due to the higher-order terms which were neglected in our derivation of the evolution equations for the soliton parameters.

From the above numerical simulations, the photon-number variance was also computed as a function of distance. The results are plotted in Fig. 37(right) where, for comparison, the

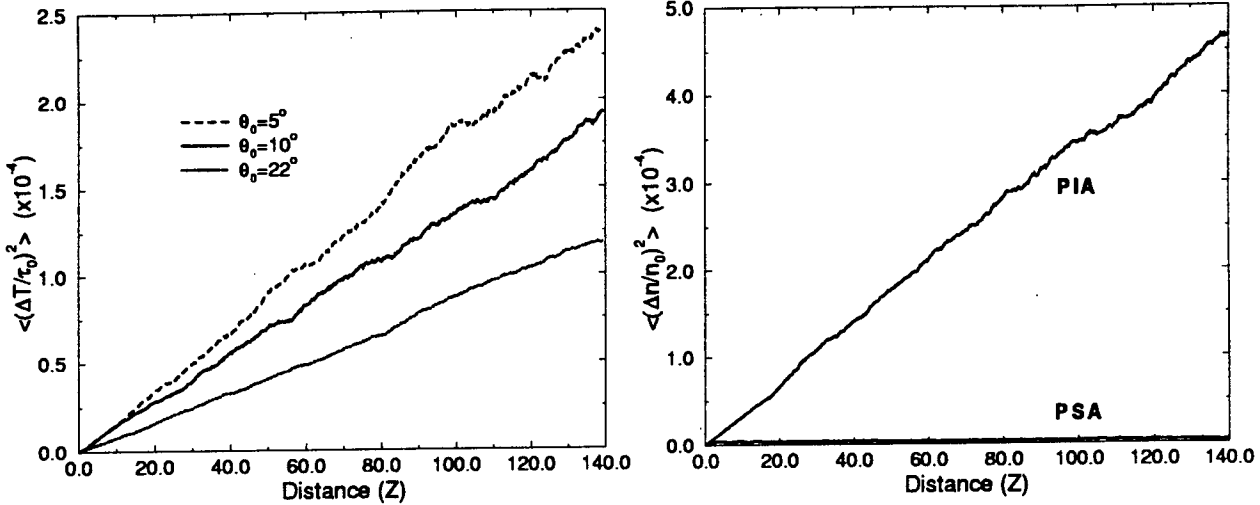


Figure 37: Left — Graph showing the pulse timing-jitter variance as a function of distance (in units of dispersion lengths) obtained by numerically solving the NLS equation with lumped PSA's and with added noise. The timing variance has been scaled in the computations by the initial pulse width  $\tau_0$  (here = 2 ps). Right — Graph showing the pulse photon-number variance as a function of distance (in units of dispersion lengths) obtained by numerically solving the NLS equation with either PIA's or PSA's. The photon-number variance is scaled in the computations by the reference photon number  $n_0$  ( $= 4.2 \times 10^5$ ).

case in which the PSA is replaced by a PIA is also shown. A value of  $\theta_0 = 10^\circ$  was chosen for the PSA runs. Note that the growth of photon-number fluctuations saturates with distance, in contrast to the unlimited growth that occurs when  $\theta_0 = 0$  [70].

**Effect of GAWBS Phase Noise:** Figure 38 shows a numerical computation of the photon-number variance, with the GAWBS noise included, as a function of distance for  $\theta_0 = 10^\circ$ . Our theory with  $\tau = \tau_0$  predicted a steady-state photon-number variance of  $2.2 \times 10^{-3}$ , which is in reasonable agreement with the numerically found value of approximately  $3 \times 10^{-3}$ . Part of the reason for the relatively large photon-number fluctuations in Fig. 38 [as compared to those in Fig. 37(right), in which the GAWBS noise was ignored] is the tendency for the system to oscillate in some parameter ranges, much like an underdamped laser oscillator. The oscillations can be significantly reduced by adding extra lumped loss in the fiber ring, so that the PSA gain can be increased. The decrease in fluctuations occurs due to the extra gain reducing the effective  $\theta_0$ , which decreases the amount of interaction between the phase and the photon-number fluctuations.

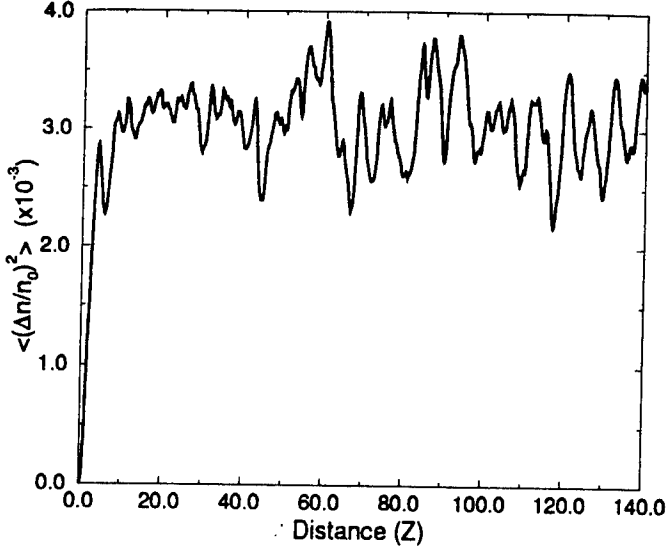


Figure 38: Graph showing the saturation of the pulse photon-number variance with distance when GAWBS phase noise is included. The GAWBS noise parameter was taken from the published data of Shelby *et al.* [67] and the random phase fluctuation was introduced just before each amplification.

**Stability of Zeros:** The issue of noise on the zero's of the stored bit stream must also be addressed, since for an optical loop memory it is required that this noise be bounded. We showed that there are no frequencies at which unbounded growth of the field fluctuations occurs if

$$\frac{|k''|}{2r^2} > 2\gamma \tan(2\theta_0). \quad (9)$$

Thus the PSA soliton ring, like Mollenauer's sliding filter line [63], is thus transparent only to solitons and opaque to noise.

In the presence of gain modulation, in analogy with loops with PIA's [71, 72], simple physical arguments allowed us to conclude that the zero's become even more stable with modulated gain. The noise on the zero's is fed by dispersive radiation. As this radiation disperses away from the center of the modulation profile (where it is generated by a soliton) into neighboring regions, the gain it encounters decreases due to the modulation and therefore it experiences a net loss.

As an example, in Fig. 39 we show the stability of an eight-bit pattern '11101100' both initially (dotted line) and after approximately 3000 km of propagation (i.e., after 15 ms of storage time) in a storage-ring with a modulated pump. The input stream was purposely seeded with pulses that had variations in their initial soliton parameters (photon number,

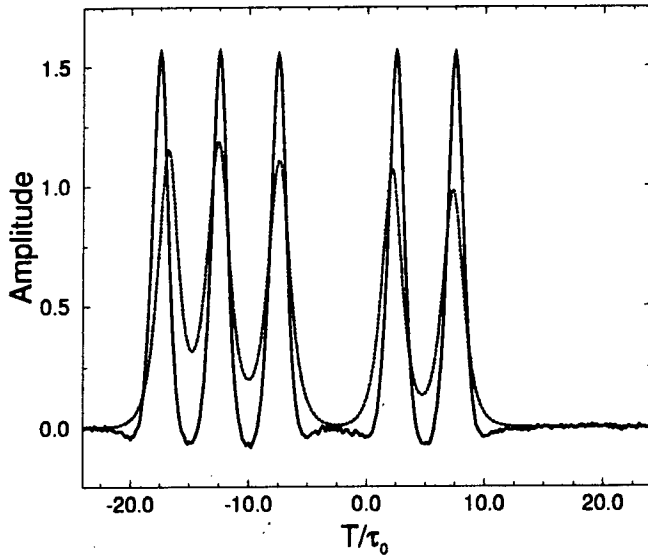


Figure 39: Plot of the input (dotted line) and output (solid line) in-phase quadrature for a single computational run of a 3.5 ps soliton bit stream at 100 Gb/s forming the eight-bit pattern ‘11101100’ in a fiber storage ring. The input pulses have been purposely seeded with random variations in their soliton parameters to show the stability of one’s and zero’s, and the output stream is shown after approximately 3000 km of propagation.

frequency, position, and phase). Both the pulses and the zero’s between them are seen to be stable. Moreover, the output pulses are significantly more uniform.

### 3.B.5 Stable Soliton Propagation: Storage Experiments

Optical storage buffers are an essential component of ultra-high-speed TDM optical networks. They can be used for queuing packets while transmitters await access to the network, for enabling receivers to handle data at rates faster than can be processed, and for rate-conversion in conjunction with optical switches. Such devices will be required to store packets with lengths on the order of 10 kbits and storage times approaching hundreds of microseconds [73]. Previous experiments using fiber logic gates [74, 75, 76] have demonstrated long-term storage at 100 MHz for packets with several hundreds of bits. Storage loops capable of up to 20 GHz bit rates have been demonstrated, requiring direct amplitude modulation [73] or indirect optical modulation via cross-gain saturation [77] to maintain the bit timing. Existing designs make use of Erbium-doped fiber amplifiers.

We have proposed the use of phase-sensitive amplification as a means of providing stability to the stored bitstream while regenerating the bit pattern, as well as simplifying the

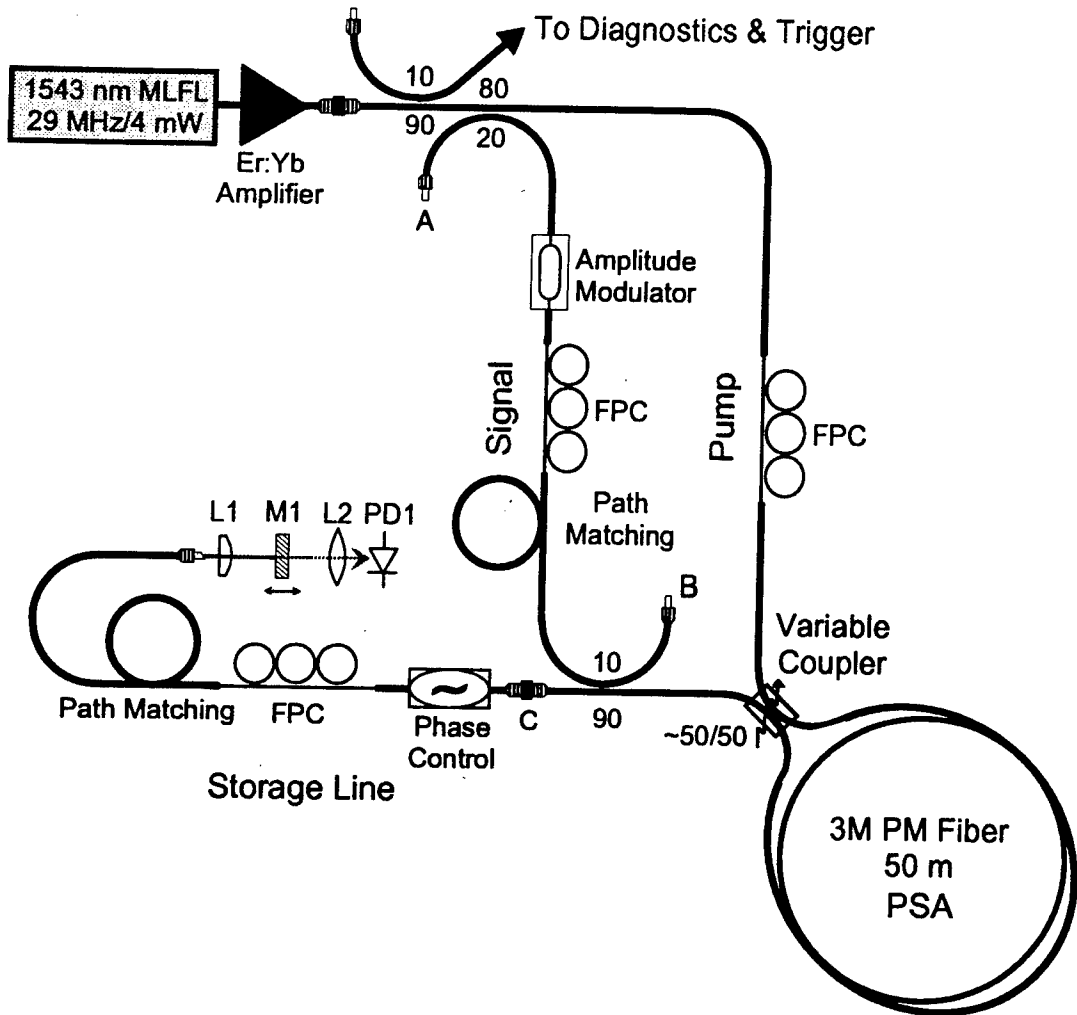


Figure 40: Experimental configuration of a linear storage line using a PSA to compensate for the linear loss. The storage line plus the PSA fiber can store 32-bits at 29 MHz.

existing storage loop designs. Our theoretical analysis indicated that stable long-distance pulse propagation in a nonlinear fiber loop using a PSA to compensate for the linear loss is possible [64]. Such a system has been shown to be self-stabilizing and robust against noise [16]. To demonstrate the use of PSA's in a storage buffer, we have loaded and stored a 32-bit data pattern for up to 0.4 ms.

The layout of our storage experiment is shown in Fig. 40. A saturable absorber modelocked Er:Yb fiber laser was used to generate 3.2 ps FWHM pulses at 1543 nm with a repetition rate of 29 MHz. An Er:Yb fiber amplifier increased the average power of the laser output to 7 mW, 10% of which was used to synchronize the electronics. An additional

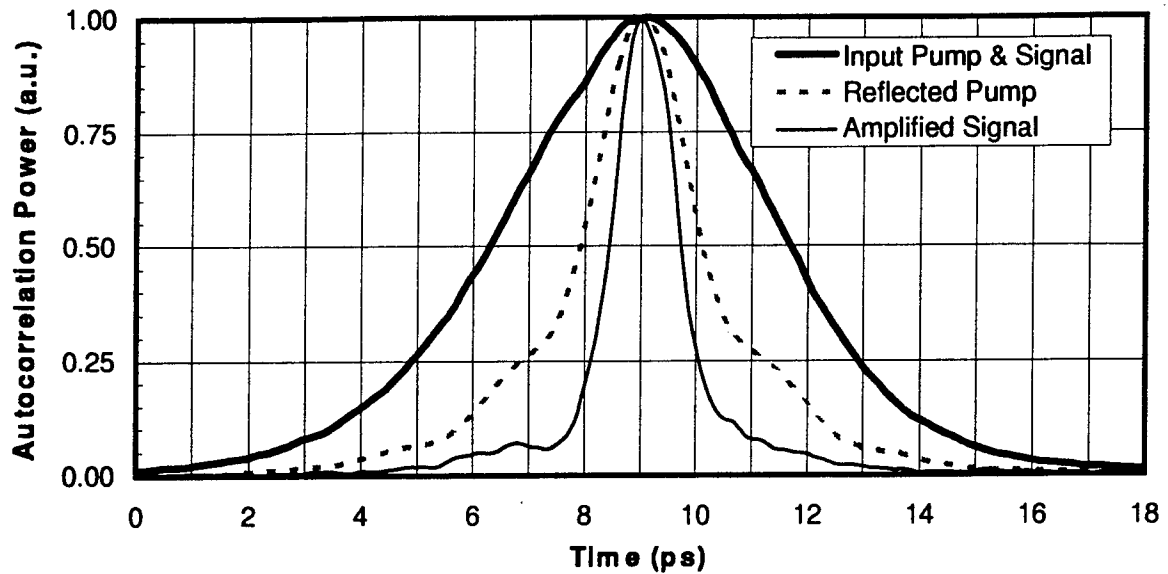


Figure 41: Autocorrelation traces of the input pump and signal pulses, the reflected pump pulse, and the output signal pulse from the fiber PSA. SPM induced pulse narrowing of the pump pulse (with no input signal pulse) during passage through the PSA fiber accounted for most of the pulse narrowing of the amplified signal pulse. Further narrowing of the signal pulse was a result of intensity dependent gain.

20% was tapped off to form the injected packets, with the remaining 5 mW used to pump the PSA [69]. The fiber PSA consisted of a tunable 50/50 fiber coupler with the outputs spliced to the ends of 50 m of standard polarization maintaining (PM) fiber. The variable 50/50 coupler was optimized to limit pump leakage into the storage line to about 0.4% of the incident pump power. The second input of the 50/50 coupler was connected to a 32-bit storage line made out of standard SMF-28 fiber. The storage line and PSA combination had a total length of 226.74 m. The storage line contained a fiber-stretching phase controller, fiber polarization controller (FPC) paddles, a collimating lens, and a translatable mirror M1 ( $T = 18.2\%$ ) to tune the length of the storage line to an exact multiple of the laser repetition period. The length adjustment was required to ensure that the stored pulses after one round trip overlapped with the pump pulses in the PSA. A line configuration for storage minimized losses, as the fiber circulator required to complete a storage loop had excessive loss (3 dB). The storage line had a round trip loss of nearly 7 dB. The signal arm was used to inject bit patterns, which were created using an amplitude modulator (AM) and timing circuitry synchronized to the laser pulses.

We first tested the PSA by disconnecting the storage line (at C) from the rest of the setup. Phase-sensitive gain for different pump and signal powers was measured by injecting the pump and signal pulses into the PSA and observing the amplified output signal pulses at port C. Extra fiber was inserted in the signal arm to delay the signal pulses by exactly one pulse period compared to pulses in the pump arm. By heating this extra length of fiber to vary its optical path, we ensured that the pump and signal pulses overlapped spatially within the PSA. The FPC's were used to align the pump and signal polarizations with the fast axis of the PM fiber to ensure interaction of the pump and signal pulses within the PSA. Figure 41 shows the autocorrelation traces of the input pump (signal) pulses (thick solid line), the reflected pump with no signal input pulses (dashed line) , and the amplified signal pulses (thin solid line). The input pump and signal to the PSA had FWHM pulse widths of 3.2 ps, the returning pump pulse from the PSA had a FWHM pulse width of 1.5 ps, and the amplified signal for the 13 dB gain case had a FWHM pulse width of 1.0 ps. The intense pump pulses undergo SPM that results in narrowing upon propagation in the anomalous dispersion PM fiber. Most of the pulse narrowing of the signal was due to the pump pulse narrowing, since the PSA gain is proportional to the peak pump power. The pump then acted as an intensity filter for the signal, narrowing the signal pulse and recentering it in the time slot, an effect that is beneficial for an optical storage device.

The PSA gain data, taken by changing the pump and signal average powers, is shown in Fig. 42, where we have plotted the theoretical curves for maximum gain, according to [78] (solid lines), and the experimental results (symbols) versus the pump average power for four signal powers. There was good agreement between the experimental and theoretical gain curves, with gains approaching 13 dB. The PSA gain had to be large enough to overcome the round-trip loss in the storage line.

With the signal path disconnected and the storage line reconnected, we misaligned the variable 50/50 coupler to allow more of the pump power to leak into the storage line. In this case the system acted as a bistable degenerate optical parametric oscillator (DOPO). When the total accumulated phase, both linear and nonlinear, of a leakage pulse in the storage line was optimum for amplification by the PSA, the leakage pulse was amplified over successive roundtrips in the storage line until the PSA was saturated, and oscillation occurred. This required that the pump input polarization and the storage line polarizations be aligned with

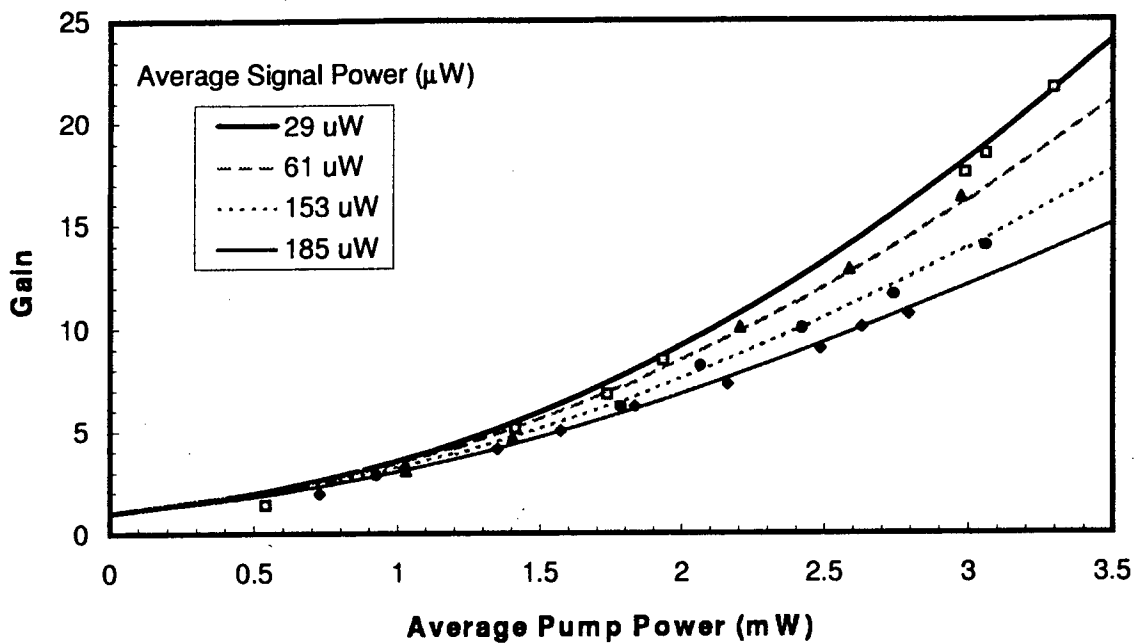


Figure 42: Experimental (symbols) and theoretical gain data (solid curves) plotted versus pump average power for four signal average powers.

the fast axis of the PM fiber, ensuring maximum amplification by the PSA. The leakage pump pulses were required to turn the bistable DOPO on; reduction of the pump leakage by balancing the variable 50/50 coupler eliminated oscillations in the storage line. Figure 43 shows autocorrelation traces of the reflected pump for the case where the DOPO was active (dotted line) and inactive (dashed line), as well as the output DOPO signal. Note that the reflected pump narrowed from 1.5 ps to 1.2 ps due to pump depletion caused by build up of the DOPO signal. The output DOPO signal had the same width as the depleted pump, as expected. The total power of the pulses in the storage line reached nearly 2.0 mW. We were able to stabilize the DOPO output using feedback to the phase controller for periods of up to 1 hour.

To demonstrate storage of a bit pattern in the storage line, we turned the bistable DOPO on with pulses injected along the signal path. This was done by balancing the variable coupler to reduce the pump leakage into the storage line to less than 0.4 % and loading the desired bit pattern by injecting 32-bit packets from the signal arm into the PSA. The packets were created using an amplitude modulator (AM) in the signal arm. The AM was synchronized to the laser pulses, and was used to create 32-bit packets of 8 *ones* and 24 *zeros*, where a

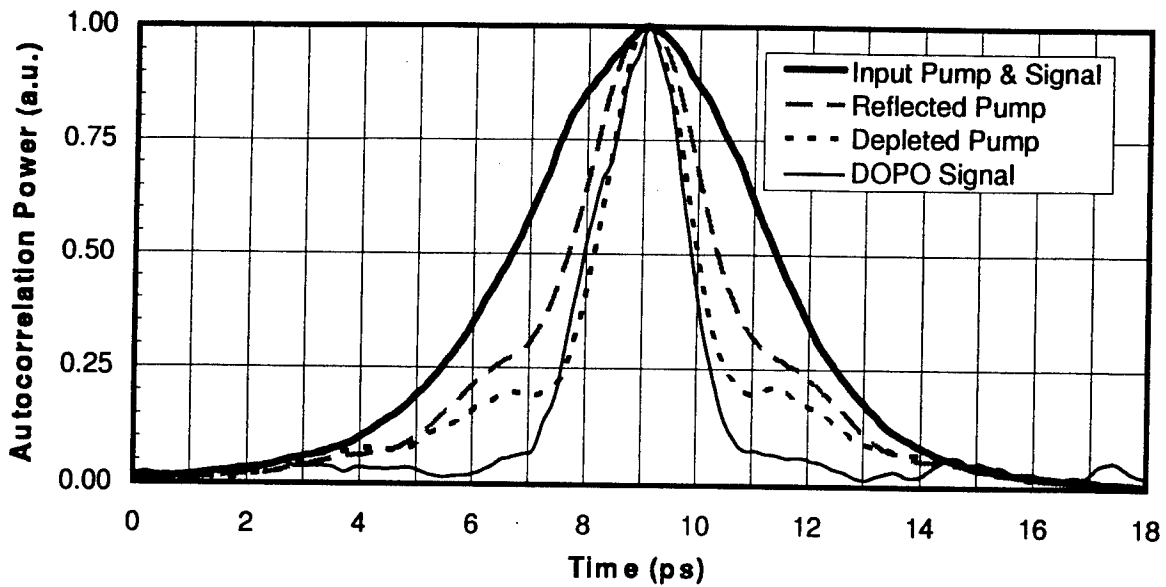


Figure 43: Autocorrelation traces of the reflected pump pulses from the PSA with (dotted line) and without (dashed line) DOPO action. Note that the reflected pump narrowed to 1.1 ps from 1.5 ps when the DOPO was oscillating, due to depletion of the pump. The autocorrelation trace of the DOPO pulse (solid line) has the same width as the depleted pump pulse, as expected.

one was represented by the presence of a pulse and a zero by the absence of a pulse. 10% of the signal ( $\approx 20 \mu\text{W}$ ) was injected into the PSA through the storage line using a 10/90 coupler, again taking care to align the polarization of the input signal pulses with the fast axis of the PM fiber. We loaded several signal packets until the power in the storage line was sufficient to maintain storage. The bistability of the DOPO ensured that ones did not build up where there were zeroes in the signal packet. We hope to increase the signal power so that one packet will be sufficient to load the storage line in future experiments. We monitored the contents of the storage line by detecting the light transmitted through mirror M1 ( $T = 18.5\%$ ) with an InGaAs photodiode and a digital oscilloscope.

Figure 44(a) shows the input signal used to load the storage line as well as the output of the storage line. The top trace shows the input signal. Each large spike contains the 8 one bits while the valleys correspond to the 24 zero bits, the combination creating the 32-bit packet described before. Active phase-stabilization of the storage line was not implemented in this experiment. We loaded the same packet 8 times until the phase was optimal for storage, at which point we observed buildup of the signal in the storage line. We then

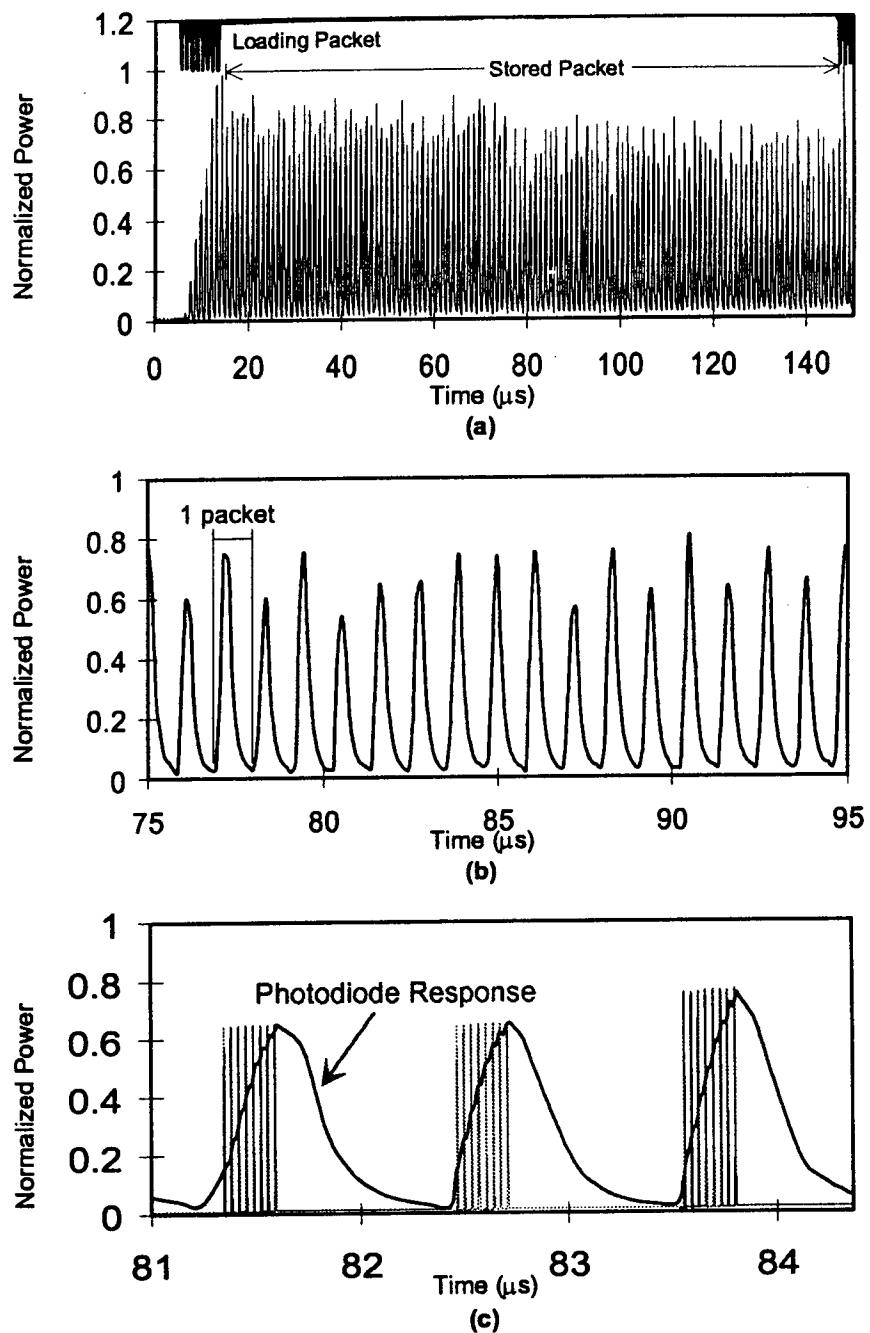


Figure 44: Output of the storage line. The top trace in (a) shows the input packet (loaded 8 times to ensure buildup in the storage line); the bottom trace shows storage for 128 round trips of the loaded packet. The trace in (b) shows a close-up view from 75 to 95  $\mu$ s of the data in (a). A single packet is noted. Trace (c) shows the photodiode response recovered by looking at 3 packets in (a). For comparison an 8 one/24 zero packet has been overlaid onto the photodiode response. Note that the evidence for the presence of bits matches well with the overlaid packets.

switched off the loading for 128 round trips. The bottom trace shows the circulating signal. From 5 to 13  $\mu$ s the signal packet is being loaded into the storage line, gradually building up to storage threshold. From 13 to 145  $\mu$ s the packets were maintained in the storage line by the PSA until the next set of 8 packets were loaded. Figure 44(b) shows a closer view of the stored packets from 75 to 95  $\mu$ s. Examination of the packets from 81 to 84  $\mu$ s, as in Fig. 44(c), shows the photodiode response more clearly. The 8 *ones* charged the photodiode, with a slight downward glitch before the arrival of the next pulse. During the 24 *zeroes* the photodiode slowly discharged, until the packet arrived on the next round trip in the storage line. Using this technique allowed us to store long data streams within the limits of our oscilloscope. The packets were stored for 132  $\mu$ s before the next loading session. Experimentally, we have observed packet storage for up to 0.4 ms, or 360 round trips in the storage line. Active stabilization of the phase in the storage loop should increase the storage time significantly.

In summary, we have demonstrated optical pulse storage of a 32-bit pattern at 29 MHz using regenerative phase-sensitive amplification. To the best of our knowledge this is the first demonstration of optical storage using a fiber PSA. We have also shown an all-optical technique for loading a bit pattern into the storage line. Long term phase stabilization of the storage line was shown for the case where pump leakage was used to load the buffer. With a higher repetition rate laser and enhanced phase stabilization, long term storage of 10 kbit packets should be possible, making this device a potential buffer in ultra-high-speed optical networks.

### 3.B.6 Soliton Regeneration

Since soliton regeneration experiments using PSA's require pulsed laser sources with extreme stability, we have, in collaboration with ATx Telecom Systems, Inc. of Naperville, Illinois, developed a highly-stable soliton source by compressing the sinusoidal modulation in the output of a short-cavity Er/Yb bulk phosphate-glass laser operating simultaneously at two frequencies. The 58.55 GHz modulation was converted into a train of 3.2 ps pulses by means of soliton pulse compression in a comb-like dispersion-tailored fiber. By spectrum analysis of the direct-detection photocurrent, the short-term stability of the repetition rate was shown to be less than 10 kHz. A patent disclosure, jointly with ATx, on this invention has been

filed.

Soliton pulse compression of the beat modulation between two optical carriers is an attractive method for generating high-repetition-rate pulse trains for application in time-division-multiplexed (TDM) optical communication systems [79, 80]. Several such sources have recently been demonstrated [81, 82, 83, 84, 85, 86]. In one approach one starts from two distributed-feedback (DFB) lasers to obtain the beat modulation [81, 82, 83]. Although this scheme allows for tunability of the repetition period, the resulting pulse-train period is not very stable because of the large free-running DFB laser linewidth. In another approach, one starts from a single DFB laser (which can be an external cavity laser with a narrow linewidth) and imparts the modulation externally with use of a stable frequency source [84, 85]. This technique yields a very stable repetition period, but at the expense of system complexity; thus leading to a very-high cost source because of the need for a stable external frequency driver. A low-cost technique involves the use of a dual-frequency coupled-cavity erbium-doped fiber laser formed with the use of intra-core fiber-grating reflectors [86]. Although this approach can potentially be of very low cost, the stability is sacrificed because of the use of a relatively long coupled-cavity length that is required to obtain two frequency operation. In Ref. [86] the stability of the 59.1 GHz pulse train was in the MHz range.

In this paper we demonstrate a highly-stable, potentially very-low cost, simple and reliable, soliton source for ultra-high speed TDM network applications. The pulse train is produced by compressing the sinusoidal modulation in the output of a two frequency Er/Yb bulk-glass laser. Since the two frequencies are generated from two different longitudinal modes of a short laser cavity, their beat frequency is highly stable. In our experiment, a 58.55 GHz pulse train is produced with a short term frequency stability of 10 kHz. This stability of  $2 \times 10^{-7}$  is obtained without active stabilization of the laser frequency or the cavity temperature; only the laser is allowed to warm up to an equilibrium temperature.

Our source is a short-cavity Er/Yb bulk phosphate-glass laser which is pumped by a Nd:YLF laser, which in turn is pumped by a semiconductor-diode laser [87]. Although the Er/Yb glass laser is designed to normally operate in a single longitudinal mode, by adjusting the laser temperature it can be made to stably lase simultaneously on two cavity modes that are five free-spectral ranges apart. The resulting wavelength separation is  $\simeq 0.5$  nm with the center frequency nominally around 1542 nm. The laser output is fiber pigtailed and typically

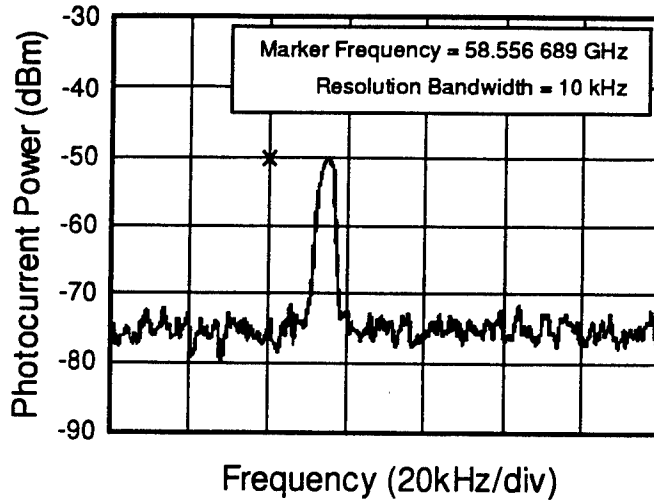


Figure 45: Photocurrent spectrum in the vicinity of the beat frequency that results when the laser output is direct detected with a fast photodetector.

90 mW of power is emitted from the fiber end.

Figure 45 shows a portion of photocurrent spectrum in the vicinity of the beat frequency that typically results when the laser output is direct detected with a fast photodetector. Note the  $< 10$  kHz beatwidth (full width at the  $-3$  dB point) whose position moves over a range of 100 kHz on the time scale of minutes as the laser temperature drifts. The short-term linewidth is expected to be even narrower. The width in Fig. 45 is limited by the 10 kHz resolution bandwidth of the spectrum analyzer and by the fact that the beat frequency was slowly drifting while the trace was being swept. In addition the beat-frequency spectrum stayed indistinguishable from that shown in Fig. 45 when the two-frequency laser output was propagated through a 11 km span of dispersion-shifted fiber (DSF) before photodetection.

In Fig. 46(Left) we display the optical spectrum of the laser output which shows the two lasing modes spaced by 0.5 nm. Figure 46(Right) shows a background-free autocorrelation trace of the laser output. Note the 17 ps periodicity and the  $\approx 3:1$  contrast of the autocorrelation signal in the central region of the trace, which are consistent with those for a two-frequency input to the autocorrelator. Near the edges of the trace, the contrast is degraded due to misalignments that occur in the autocorrelator when it sweeps over such a wide time range.

The output of the two-frequency laser was launched into a comb-like dispersion-tailored fiber (DTF), as shown in Fig. 47, after passing it through a phase modulator, which was

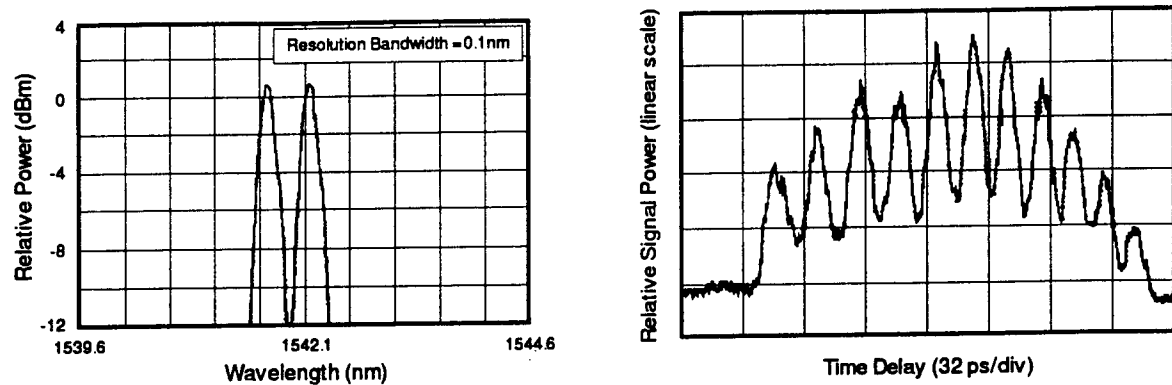


Figure 46: Optical spectrum (Left) and autocorrelation trace (Right) of the dual-frequency Er/Yb glass laser.

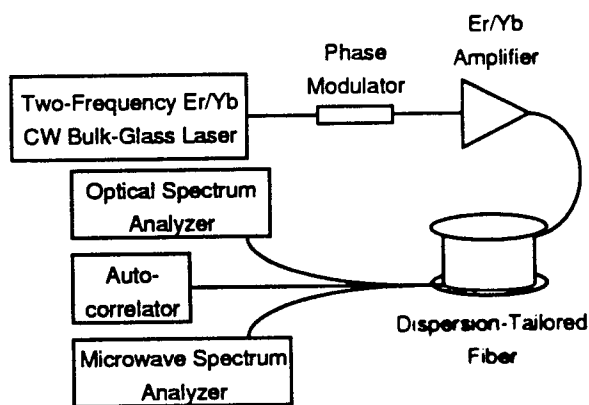


Figure 47: Experimental setup. The phase modulator was driven at 100 MHz.

driven at 100 MHz to spectrally broaden the two frequencies. Without phase modulation, a significant portion of the launched power was reflected back due to stimulated Brillouin scattering. The phase modulator introduced significant power loss requiring the use of an Er/Yb co-doped fiber amplifier to boost the power entering the DTF to 120 mW. The comb-like DTF was constructed following the designs in Refs. [86] and [85] and consisted of 3 sets of alternate segments of DSF (Corning SMF/DS) and standard telecommunication fiber (STF, Corning SMF-28 CPCS). The design of the DTF is indicated in Fig. 48, which shows the distance dependence of the dispersion coefficient  $\beta_2$  and the nonlinear coefficient  $\gamma = n_2\omega_0/cA_{\text{eff}}$  along the DTF. Here  $n_2$  is the nonlinear index,  $\omega_0$  is the optical carrier frequency in radians/s,  $c$  is the speed of light in vacuum, and  $A_{\text{eff}}$  is the effective core area of the fiber. The values of  $\beta_2$  and  $\gamma$  for the DSF and the STF were estimated by comparing the distance dependence of the optical spectrum and the pulse autocorrelation with numerical simulations of the pulse propagation.

A typical optical spectrum of the pulses at the output of the DTF is shown in Fig. 49(Left). As compared to the optical spectrum of the laser output in Fig. 46(Left), the spectrum in Fig. 49(Left) is considerably broadened as new peaks have appeared due to self phase modulation. The resulting autocorrelation of the pulse train is shown by the solid trace in Fig. 49(Right). [Note the logarithmic scale in Fig. 49(Right) when comparing with the central region of the autocorrelation trace in Fig. 46(Right).] The measured autocorrelation FWHM is 5.6 ps, which gives a pulselwidth of 3.2 ps, assuming a  $\text{sech}^2$  pulse-intensity shape for the evolved pulse. Since the repetition period is 17.1 ps, a mark-to-space ratio of  $> 5$  is obtained. The mark-to-space ratio can be further increased by elongating the DTF with use of a larger number of paired segments (DSF followed by STF of appropriate length) in the DTF, as was the case in Refs. [86] and [85]. Similarly, increasing the power launched into the DTF beyond the 120 mW used in our experiment by employing a higher-power optical amplifier would result in a larger mark-to-space ratio.

To compare the results of our experiment with the theory, we simulated the pulse propagation in the DTF by numerically solving the nonlinear Schrödinger equation including loss. The dashed curve in Fig. 49(Right) is the theoretically predicted autocorrelation trace for the parameters in our experiment. The agreement with the experimentally observed autocorrelation is quite good, although discrepancies exist in the wings of the pulse profile below

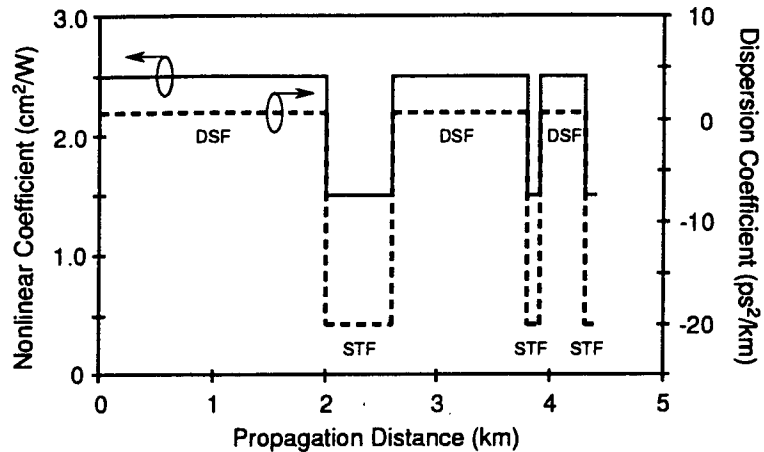


Figure 48: Comb-like DTF design showing the distance dependence of the dispersion and nonlinear coefficients. The lengths of the DSF segments were 2, 1.2, and 0.4 km, respectively; and those of the STF segments were 0.6, 0.1, and 0.1 km, respectively.

–15 dB. These discrepancies are probably due to errors in our estimates of the various fiber parameters and the losses at the various fiber splices.

In conclusion, we have demonstrated a highly-stable, potentially very-low cost, simple and reliable, 58.55 GHz soliton source for ultra-high speed TDM network applications. The repetition period exhibits stability of  $2 \times 10^{-7}$  because of the intrinsic stability of the axial mode spacing in the short-cavity diode-pumped solid-state laser. Such solid-state lasers can be manufactured with precise tolerances to obtain pre-determined fixed repetition-rate soliton sources that can be locked to each other at remote locations with minimal electronics. Such soliton sources would thus be analogous to quartz crystal oscillators that are commonly employed in the telecommunication networks of today.

### 3.B.7 Pulse Shaping with PSA's

We investigated two simple methods for producing the non-uniform phase chirp and the resulting pulse-shaping when amplified with a PSA. The self-phase modulation method due to the  $\chi^{(3)}$  nonlinearity of an optical fiber was found to be more efficient than the method of imparting linear dispersion with an optical fiber [47].

Nonlinear directional couplers use the interaction between two closely-spaced nonlinear optical waveguides to switch pulses from one waveguide to the other. Because this interaction is nonlinear, the large-amplitude pulse center is switched more easily than the small-

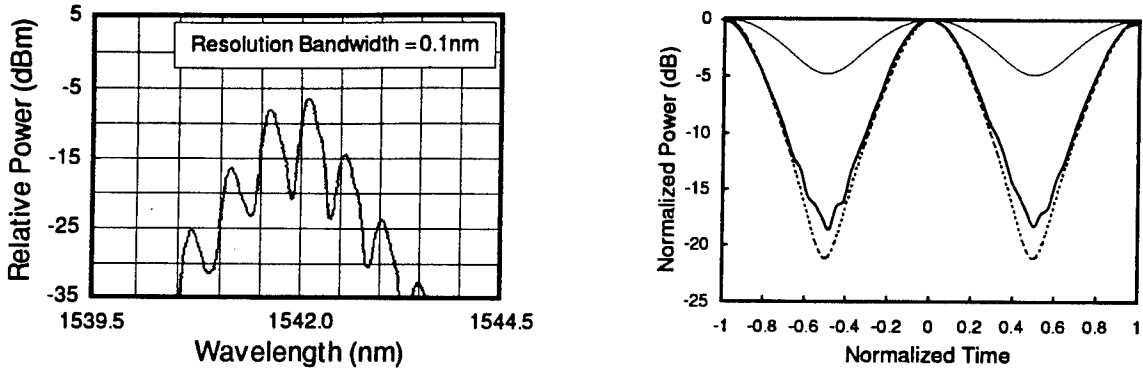


Figure 49: Optical spectrum (Left) and autocorrelation trace (Right) of the pulse train at the output of the DTF. In (b), the dashed curve is a theoretical fit and the time scale on the abscissa is normalized to the pulse repetition period of 17.1 ps. Also in (b) the thin solid curve is the theoretical autocorrelation trace for a two-frequency laser source.

amplitude pulse tails, even to the extent that these two parts of the pulse can be directed to different output ports [88]. This pulse break-up leads to reduced efficiency of such optical switching devices. It has been observed that squaring-up the optical pulses improves the switching efficiency [88], since a sharper pulse has less energy in its tails.

One method for accomplishing this optical pulse shaping is by modifying its amplitude and phase in the frequency domain, such as with a liquid crystal modulator [89]. Here we show that PSA's can also be used to accomplish this pulse shaping. Recently we have shown that PSA's can be used to compensate fiber dispersion [90]. The essential idea here is to produce a non-uniform phase chirp across the pulse, and then to convert these phase variations into amplitude variations using a phase-sensitive amplifier. Two simple methods for producing the non-uniform phase chirp and the resulting pulse-shaping are self-phase modulation due to the  $\chi^{(3)}$  nonlinearity of an optical fiber, and linear dispersion; here only the results of using self-phase modulation are described.

The response of a phase-sensitive amplifier is given by

$$u_{\text{out}} = \cosh \gamma u_{\text{in}} + e^{i\phi} \sinh \gamma u_{\text{in}}^* \quad (10)$$

where  $G = e^{2\gamma}$  is the amplifier's maximum intensity gain and  $\phi$  is its phase. Alternatively, expressed in terms of  $v = ue^{-i\phi/2}$ , this is

$$v_{\text{out}} = \sqrt{G} \operatorname{Re} v_{\text{in}} + \frac{i}{\sqrt{G}} \operatorname{Im} v_{\text{in}}. \quad (11)$$

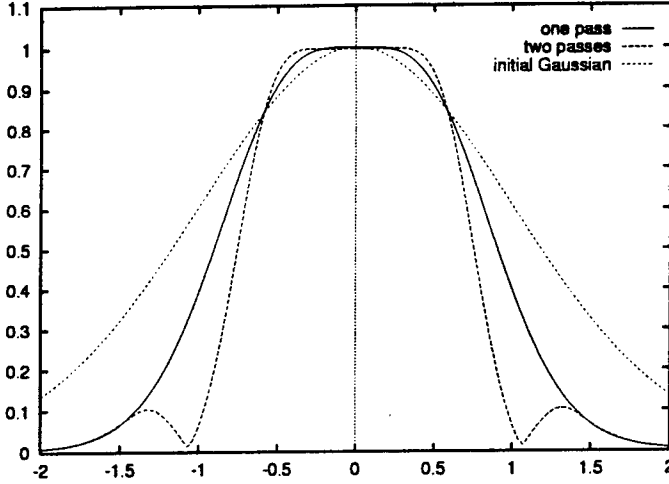


Figure 50: Pulse magnitude after one and two passes through the self-phase modulator and amplifier combination for an initial Gaussian profile. Here  $\beta = 1.836$  and  $G = 5.0$ .

This expression clearly shows the attenuation of the out-of-phase components of the pulse.

For the case of self-phase modulation, we assume for simplicity that an initial profile  $v_0(x)$  has evolved to

$$v_{\text{in}} = v_0(x) e^{i\pi/2 - i\beta|v_0(x)|^2} \quad (12)$$

at the input to the amplifier [54]. The phase change at zero amplitude is assumed to be adjusted to  $\pi/2$ , so that the tails of the pulse will be attenuated, while the phase change due to the nonlinear self-phase modulation is parameterized by  $\beta$ . In addition, the inclusion of the parameter  $\beta$  allows us to scale  $v_0(x)$  to have a maximum amplitude of unity.

In the limit of large gain,  $G \gg 1$ , and a real initial profile  $v_0$  the above two expressions simplify to

$$v_{\text{out}}(x) = \sqrt{G} \sin(\beta v_0(x)^2) v_0(x). \quad (13)$$

If additional attenuation is present after the amplifier to reduce the overall gain, it is possible for a unit input amplitude to produce a unit output amplitude, i.e.,

$$v_{\text{out}}(x) = \frac{\sin(\beta v_0(x)^2)}{\sin \beta} v_0(x). \quad (14)$$

With this added attenuation the more general case, Eq. (11), becomes

$$v_{\text{out}} = [\text{Re } v_{\text{in}} + \frac{i}{G} \text{Im } v_{\text{in}}] / \sin \beta, \quad (15)$$

where  $v_{\text{in}}$  is given as in Eq. (12).

It is also possible to consider multiple passes through the self-phase modulator and parametric amplifier combination. To do so, one merely takes the result  $v_{\text{out}}$  and treats it as a new  $v_0$ . In the case of large gain, as described in Eq. (14), this produces a functional iteration which has maximum convergence rate to the fixed point at  $v = 1$  when  $\beta \approx 1.836$ .

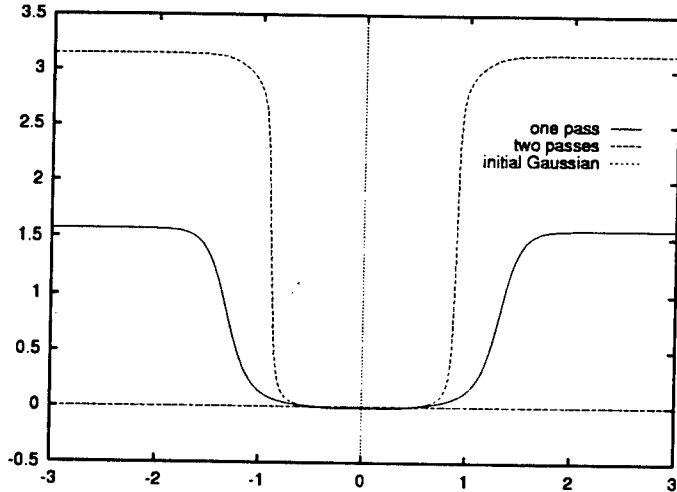


Figure 51: Pulse phase after one and two passes through the self-phase modulator and amplifier combination. Parameters are as in Fig. 1.

In Figs. 50 and 51 we show the numerical solution for the magnitude and phase of  $v$ , calculated from Eqs. (11) and (15), when  $\beta = 1.836$  and  $G = 5.0$  after one and two passes through the self-phase modulator and amplifier combination. The solution clearly shows significant flattening and sharpening of the pulse profiles.

### 3.C Analysis of Device and System Performance

The goals of this part of the research were:

1. To determine the ultimate quantum limit on optical switching by utilizing the quantum state space approach similar in spirit to the suggestion of PNA.

The following was accomplished:

- We investigated a squeezed light homodyne detection scheme which, with present-day technology, leads to more than two orders of magnitude data rate improvement over other current experimental systems for moderate loss.

Below we describe in detail the results obtained.

#### 3.C.1 Analysis of Device and System Performance

Quantum cryptography has emerged as a potentially promising method of secure key distribution in optical networks. [91] As a part of our investigation into the role of novel quantum devices in high-speed optical networks, we have studied the use of photon-number amplifiers (PNA) and photon-number duplicators (PND) in optical cryptographic systems. Specifically, we have developed several methods for eavesdropping on the standard four coherent state quantum cryptosystem [91] together with a possible countermeasure. We found a limit on the tolerable energy disadvantage of the user as compared to the eavesdropper of such systems, beyond which the eavesdropping cannot be detected even while the eavesdropper is obtaining perfect information. In this work we found that the PNA and PND play a significant role not only for eavesdropping but also for enhancing the security of quantum cryptosystems.

Several new quantum cryptosystems utilizing different kinds of nonclassical lights are proposed which can accommodate high intensity field and high data rate. However, they are all sensitive to loss and both the high rate and the strong-signal character rapidly disappear. A squeezed-light homodyne detection scheme is proposed which, with present-day technology, leads to more than two orders of magnitude data rate improvement over the four coherent state system for moderate loss.

Two publications [92][93] have resulted from this work.

We have introduced the concept of an all-optical repeater which is essentially a photon-number switch. It is different from the usual optical switch in that it works on individual photon numbers as a quantum device. Specifically, for 00K and binary PPM signals the switch transforms the quantum state as follows: 00K

$$|0\rangle \rightarrow |0\rangle \quad (16)$$

$$|1\rangle \rightarrow |S\rangle \quad (17)$$

$$|n\rangle \rightarrow |S\rangle \quad (18)$$

$$\vdots \quad (19)$$

bPPM

$$|n_1, N_2\rangle \xrightarrow{n_1 > n_2} |S, 0\rangle \quad (20)$$

$$|n_1, N_2\rangle \xrightarrow{n_1 < N_2} |0, S\rangle \quad (21)$$

In eqn (1),  $|n\rangle$  is a photon-number eigenstate and  $|SS\rangle$  is a coherent state of average photon number  $S$ . In eqn (2),  $|n_1, n_2\rangle$  are the photon-number eigenstates of the two separate time durations while  $|S, 0\rangle$  are coherent states. The possible concrete realizations of (1) and (2), which are possible in principle because they can be extended to a unitary transformation with an auxiliary mode, are still being pursued. However, their performance advantage can already be studied from the representations (1) and (2). In particular, for (1) the error exponent  $E_{ns}^{-1} \log P_e$  where  $N_s$  is the signal photon number, is readily found.

$$E = -\frac{1}{N_s} \log [1 - (1 - e^{-N_s})^N] \quad (22)$$

where  $N$  is the total number of such equally spaced repeaters in the line. This exponent depends on  $N_s$  in contrast to the PNA and the PIA lines. In fig. 1, the gain  $G = 2$  and  $G = 10$  PNA line and the gain independent PIA line are plotted together with the all-optical repeater line with  $N_s = 10$  and  $N_s = 20$ . It is evident that the all-optical repeater line is already more than  $10dB$  better than even the PNA line for almost all values of  $N$ , for the not very high level for  $N_s = 10$ .

Similar performance improvement is obtained for the bPPM repeater. Realistic system imperfections are being included in a further elaboration of this work.

## 4 Conclusions

This project is a continuation of a joint theoretical-experimental research program which was undertaken to initiate the development of novel quantum devices for greatly improved optical communications and switching in both local network and long haul applications. In this final report we present the results obtained in the various efforts undertaken by each of the principal investigators. Specifically, we describe the demonstration of the first photonic-wire semiconductor laser and the lasers with directional light output and the investigation of novel microcavity semiconductor laser structure; we also present the results of our investigation on the implementation of nondegenerate parametric amplifier in fiber lines that support communication rates of ten's of gigabits per second, together with the results of our modeling and experimental efforts for our proposed long-term storage of soliton bit streams in fiber/PSA rings. We also present the progress on the theoretical investigation to determine the ultimate quantum limit on optical switching.

## References

- [1] H. P. Yuen and M. Ozawa, "Ultimate Information Carrying Limits of Quantum Systems," *Phys. Rev. Lett.* **70**, 363-366 (1993).
- [2] H. P. Yuen, "Nonclassical Light," in *Photons and Quantum Fluctuations*, ed. by E. R. Pike and H. Walther, Adam Hilger, pp. 1-9, 1988.
- [3] H. P. Yuen, "Reduction of quantum fluctuation and suppression of Gordon-Haus effect in phase-sensitive linear amplifiers," *Opt. Lett.* **17**, 73-75 (1992).
- [4] O. Aytür and P. Kumar, "Pulsed Twin Beams of Light," *Phys. Rev. Lett.*, **65**, 1551-1554 (1990).
- [5] G. Bartolini, R.-D. Li, P. Kumar, W. Riha and K. V. Reddy, "1.5  $\mu\text{m}$  phase-sensitive amplifier for ultra-high speed communications," presented at OFC '94.
- [6] N. A. Olsson, P. A. Andrekson, J. R. Simpson, T. Tanbun-Ek, R. A. Logan, and K. W. Wecht, "Two-Channel Soliton Pulse Propagation over 9,000 km with  $10^{-9}$  Bit-Error-Rate," *Optics and Photonics News*, vol. 2, no. 5, pp. 52 (1991).
- [7] J. P. Gordon and L. F. Mollenauer, "Effects of Fiber Nonlinearities and Amplifier Spacing on Ultra-Long Distance Transmission," *Journal of Lightwave Technology*, vol. 9, pp. 170-173 (1991).
- [8] J. P. Gordon and H. A Haus, "Random Walk of Coherently Amplified Solutions in Optical Fiber Transmission", *Opt. Lett.*, **11**, 665-667 (1986).
- [9] S. H. Lee, "Ultra long distance optical communication using phase sensitive linear amplifier chains," Ph.D. dissertation, Dept. of Electrical Engineering and Computer Science, Northwestern University, December 1992.
- [10] J. N. Kutz, W. L. Kath, R.-D. Li, and P. Kumar, "Long-distance pulse propagation in nonlinear optical fibers using periodically-spaced parametric amplifiers," *Opt. Lett.* **18**, 802-804 (1993).
- [11] H. P. Yuen, "Generation, Detection and Application of High-Intensity Photo-Number-Eigenstate Fields," *Phys. Rev. Lett.*, **56**, 2176-2179 (1986).
- [12] S. S. Wagner, "Optical Amplifier Applications in Fiber Optic Local Networks," *IEEE Transactions on Communications*, **COM-35**, , 419-426 (1987).
- [13] H. P. Yuen, "Design of Transparent Optical Networks by Using Novel Quantum Amplifiers and Sources," *Opt. Lett.*, **12**, 789-791 (1987).
- [14] H. P. Yuen, "Photon Number Duplication and Quantum Nondemolition Detection," submitted to *Journal of Quantum Optics*.
- [15] V. Mizrahi, K. W. DeLong, G. I. Stegeman, M. A. Saifi and M. J. Andrejco, "Two-photon absorption as a limitation to all-optical switching," *Opt. Lett.*, **14**, 1140-1142 (1989).

[16] M. N. Islam, C. E. Soccilich, C. J. Chen, K. S. Kim, J. R. Simpson, and U. C. Paek, "All-optical inverter with 1 pJ Switching Energy," Conference on Lasers and Electro-Optics, 1991 Technical Digest Series Volume 10, CMB3, pp. 18.

[17] Daniel Y. Chu and Seng-Tiong Ho, 9<sup>th</sup> Interdisciplinary Laser Sci. Conf. Tech. Dig., MT5, Oct. 93.

[18] Y. Yamamoto, *Coherence, Amplification, and Quantum Effects in Semiconductor Lasers*, (John Wiley & Sons, New York, 1991).

[19] S. T. Ho, S. L. McCall, and R. E. Slusher, Opt. Lett. **18**, 909 (1993).

[20] D. Y. Chu and S. T. Ho, J. Opt. Soc. Am. B **10**, 381 (1993).

[21] R. E. Slusher, A. F. J. Levi, U. Mohideen, S. L. McCall, S. J. Pearton, and R. A. Logan, Appl. Phys. Lett. **63**, 1310 (1993).

[22] M. K. Chin, D. Y. Chu, and S. T. Ho, J. Appl. Phys. **75**, 3302 (1993).

[23] E. Yablonovitch, Phys. Rev. Lett., Vol. 58, pp.2059-2062, 1987.

[24] D. Y. Chu and S. T. Ho, Optical Society of America Annual Meeting Technical Digests (San Jose, California), MT5, Oct. 1991.

[25] B. Meade and J. D. Joannopoulos, Optical Society of America Annual Meeting Technical Digests (San Jose, California), MT1, Oct. 1991; P. R. Villeneuve, S. Fan, J. D. Joannopoulos, K. Y. Lim, G. S. Petrich, L. A. Kolodziejski, and R. Reif, Appl. Phys. Lett., Vol.67, No.2, pp.167-169, 1995.

[26] C.E.Reuter, R.M.Joseph, E.T.Thiele, D.S.Katz, A.Taflove, IEEE Microwave and Guided Wave Lett., Vol. 4, No. 10, pp. 344-346, 1994.

[27] A. Villeneuve, C. C. Yang, P. G. Wigley, G. I. Stegeman, J. S. Aitchison, and C. N. Ironside, "Ultrafast all-optical switching in semiconductor nonlinear directional-couplers at half the band-gap," Appl. Phys. Lett., vol. 61, pp. 147-149, 1992.

[28] K. Al-hemyari, J. S. Aitchison, C. N. Ironside, G. T. Kennedy, R. S. Grant, and W. Sibbett, "Ultrafast all-optical switching in GaAlAs integrated interferometer in 1.55  $\mu\text{m}$  spectral region," Electron. Lett., vol. 28, pp. 1090-1092, 1992.

[29] M. N. Islam, C. E. Soccilich, R. E. Slusher, A. F. J. Levi, W. S. Hobson, and M. G. Young, "Nonlinear spectroscopy near half-gap in bulk and quantum-well GaAs/AlGaAs wave-guides," J. Appl. Phys., vol. 71, pp. 1927-1935, 1992.

[30] S. T. Ho, C. E. Soccilich, M. N. Islam, W. S. Hobson, A. F. J. Levi, and R. E. Slusher, "Large nonlinear phase-shifts in low-loss  $\text{Al}_x\text{Ga}_{1-x}\text{As}$  wave-guides near 1/2-gap," Appl. Phys. Lett., vol. 59, pp. 2558-2560, 1991.

[31] K. Al-hemyari, A. Villeneuve, J. U. Kang, J. S. Aitchison, C. N. Ironside, and G. I. Stegeman, "Ultrafast all-optical switching in GaAlAs directional-couplers at 1.55  $\mu\text{m}$  without multiphoton absorption," Appl. Phys. Lett., vol. 63, pp. 3562-3564, 1994.

[32] M. Sheik-Bahae, A. A. Said, T.-H. Wei, D. J. Hagan, and E. W. Van Stryland, IEEE J. Quantum. Electron. **26**, 760 (1990).

[33] D. Cotter, C. N. Ironside, B. J. Ainslie, and H. P. Girdlestone, Opt. Lett. **14**, 317 (1989).

[34] M. C. Gabriel, N. A. Whitaker, Jr., C. W. Dirk, M. G. Kuzyk, and M. Thakur, Opt. Lett. **16**, 1334 (1991).

[35] K. B. Rochford, Raymond Zanoni, George I. Stegeman, W. Jrug E. Miao, and M. W. Beranek, IEEE J. Quant. Elect. **28**, 2044 (1992).

[36] M. J. LaGasse, K. K. Anderson, H. A. Haus, and J. G. Fujimoto, Appl. Phys. Lett. **54**, 2068 (1989).

[37] K. L. Hall, G. Lenz, E. P. Ippen, and G. Raybon, Opt. Lett. **17**, 874 (1992).

[38] S. T. Ho, C. E. Soccilich, M. N. Islam, W. S. Hobson, A. F. J. Levi, and R. E. Slusher, Appl. Phys. Lett. **59**, 2558 (1991).

[39] A. Villenueve, C. C. Yang, G. I. Stegeman, C.-H. Lin, and H.-H. Lin, Appl. Phys. Lett. **62**, 2465 (1993).

[40] M. Sheik-Bahae, D. J. Hagan, and E. W. Van Stryland, Phys. Rev. Lett. **65**, 96 (1990).

[41] R.-D. Li, P. Kumar and W. L. Kath, "Dispersion compensation with phase-sensitive amplifiers", J. of Lightwave Technol. **12**, 541-549 (1994).

[42] C. G. Goedde, W. L. Kath, and P. Kumar, "Compensation of the soliton self-frequency shift with phase-sensitive amplifiers," Opt. Lett. **19**, 2077-2079 (1994).

[43] C. G. Goedde, W. L. Kath, and P. Kumar, "Periodic amplification and conjugation of optical solitons," Opt. Lett. **20**, 1365-1367 (1995).

[44] W. L. Kath, A. Mecozzi, P. Kumar, and C. G. Goedde, "Long-term storage of a soliton bit stream using phase-sensitive amplification: Effects of soliton-soliton interactions and quantum noise," submitted to *Optics Communications*.

[45] G. D. Bartolini, D. K. Serkland, W. L. Kath, and P. Kumar "A Highly-Stable 60 GHz Soliton Source at 1550 nm," submitted to Photonics Technology Letters.

[46] G. D. Bartolini, D. K. Serkland, P. Kumar, and W. L. Kath "All-optical storage of a picosecond-pulse packet using phase-sensitive amplification," to be submitted to Photonics Technology Letters.

[47] W. L. Kath, P. Kumar, and J. E. Oleksy, "Optical pulse shaping using phase-sensitive amplification," in *IPR'94 Technical Digest, Vol. 3*, (Optical Society of America, Washington, DC 1994), pp. 319-321.

[48] F. M. Mitschke and L. F. Mollenauer, "Discovery of the soliton self-frequency shift," Opt. Lett. **11**, 659 (1986).

[49] J. P. Gordon, "Theory of the soliton self-frequency shift," Opt. Lett. **11**, 662 (1986).

[50] A. Hasegawa and Y. Kodama, "Guiding-center soliton in optical fibers," *Opt. Lett.* **15**, 1443 (1990); "Guiding-center soliton," *Phys. Rev. Lett.* **66**, 161 (1991); Y. Kodama and A. Hasegawa, "Theoretical foundations of optical-soliton concept in fibers," in *Progress in Optics XXX*, E. Wolf, ed., (Elsevier, Amsterdam, 1992).

[51] J. N. Kutz, W. L. Kath, R.-D. Li, and P. Kumar, "Long-distance pulse propagation in nonlinear optical fibers using periodically-spaced parametric amplifiers," *Opt. Lett.* **18**, 802–804 (1993).

[52] J. N. Kutz, C. V. Hile, W. L. Kath, R.-D. Li, and P. Kumar, "Pulse propagation in nonlinear optical fiber-lines that employ phase-sensitive parametric amplifiers," *J. Opt. Soc. Am. B* **11**, 2112–2123 (1994).

[53] H. P. Yuen, "Reduction of quantum fluctuation and suppression of the Gordon-Haus effect with phase-sensitive linear amplifiers," *Opt. Lett.* **17**, 73–75 (1992).

[54] G. P. Agrawal, *Nonlinear Fiber Optics*, (Academic, New York, 1989).

[55] J. R. Sauer, M. N. Islam and S. P. Dijaili, "A soliton ring network," *J. Lightwave Technol.* **11**, 2182 (1993).

[56] A. Yariv, D. Fekete, and D. M. Pepper, "Compensation for channel dispersion by nonlinear optical phase conjugation," *Opt. Lett.* **4**, 52 (1979).

[57] R. A. Fisher, B. R. Suydam, and D. Yevick, "Optical Phase Conjugation for Time-Domain Undoing of Dispersive Self-Phase-Modulation Effects," *Opt. Lett.* **8**, 611 (1983).

[58] W. Forysiak and N. J. Doran, "Conjugate Solitons in Amplified Optical Fibre Transmission Systems," *Electron. Lett.* **30**, 154 (1994).

[59] W. Forysiak and N. J. Doran, "Phase Conjugation for Jitter and Soliton-Soliton Compensation in Soliton Communications," in *Conference on Lasers and Electro-Optics Technical Digest* (Optical Society of America, Washington, 1994), pp. 367–368.

[60] S. Chi and S. Wen, "Recovery of the Soliton Self-Frequency Shift by Optical Phase Conjugation," *Opt. Lett.* **19**, 1705 (1994).

[61] J. Zhou, N. Park, K. J. Vahala, M. A. Newkirk, and B. I. Miller, "Conjugate Solitons in Amplified Optical Fibre Transmission Systems," *Electron. Lett.* **30**, 859 (1994).

[62] J. P. Gordon and H. A. Haus, "Random Walk of Coherently Amplified Solitons in Optical Fiber Transmission," *Opt. Lett.* **11**, 665–667 (1986).

[63] L. F. Mollenauer, J. P. Gordon, and S. G. Evangelides, "The Sliding-Frequency Guiding Filter: an Improved Form of Soliton Jitter Control," *Opt. Lett.* **17**, 1575–1577 (1992).

[64] A. Mecozzi, W. L. Kath, P. Kumar, and C. G. Goedde, "Long-term Storage of a Soliton Bit Stream by Use of Phase-Sensitive Amplification," *Opt. Lett.* **19**, 2050–2052 (1994).

[65] M. Yu and C. J. McKinstrie, "Modulational Instability in Dispersion-Flattened Fibers," in *OSA Annual Meeting Program* (Optical Society of America, Washington, 1994), p. 56.

[66] J. D. Moores, W. S. Wong, and H. A. Haus, "Stability and timing maintenance in soliton transmission and storage rings," *Opt. Commun.* **113**, 153–175 (1994).

[67] R. M. Shelby, M. D. Levenson, and P. W. Bayer, "Guided acoustic-wave forward Brillouin scattering," *Phys. Rev. B* **31**, 5244–5252 (1985).

[68] K. Bergman, H. A. Haus, and M. Shirasaki, "Analysis and Measurement of GAWBS Spectrum in a Nonlinear Fiber Ring," *Appl. Phys. B* **55**, 242–249 (1992).

[69] G. Bartolini, R.-D. Li, P. Kumar, W. Riha, and K. V. Reddy, "1.5  $\mu\text{m}$  phase-sensitive amplifier for ultra-high speed communications," In *OFC'94 Technical Digest*, **4**, 202–203 (Optical Society of America, 1994).

[70] I. H. Deutsch and I. Abram, "Reduction of Quantum Noise in Soliton Propagation by using Phase Sensitive Amplification," *J. Opt. Soc. Am. B* **11**, 2303–2313 (1994).

[71] H. A. Haus and A. Mecozzi, "Long-Term Storage of a Bit Stream of Solitons," *Opt. Lett.* **17**, 1500–1502 (1992).

[72] C. R. Doerr, W. S. Wong, H. A. Haus, and E. P. Ippen, "Additive-pulse mode-locking/limiting storage ring," *Opt. Lett.* **19**, 1747–1749 (1994).

[73] J. D. Moores, K. L. Hall, S. M. LePage, K. A. Rauschenbach, W. Wong, H. A. Haus, and E. P. Ippen, "20-GHz Optical Storage Loop/Laser Using Amplitude Modulation, Filtering, and Artificial Fast Saturable Absorption," *IEEE Photonics Technology Letters* **7**, 1096–1098 (1995).

[74] V. I. Belotitskii, E. A. Kuzin, M. P. Petrov, and V. V. Spirin, "Demonstration of over 100 million round trips in recirculating fibre loop with all-optical regeneration," *Electronic Letters* **29**, 49–50 (1993).

[75] J. N. A. Whitaker, M. C. Gabriel, H. Avramopoulos, and A. Huang, "All-optical, all-fiber circulating shift register with an inverter," *Optics Letters* **16**, 1999–2001 (1991).

[76] H. Avramopoulos and J. N. A. Whitaker, "Addressable fiber-loop memory," *Optics Letters* **18**, 22–24 (1993).

[77] K. L. Hall, J. D. Moores, K. A. Rauschenbach, W. Wong, E. P. Pippen, and H. A. Haus, "All-Optical Storage of a 1.25 kb Packet at 10 Gb/s," *IEEE Photonics Technology Letters* **7**, 1093–1095 (1995).

[78] M. E. Marhic, C. H. Hsia, and J.-M. Jeong, "Optical Amplification in a Nonlinear Fibre Interferometer," *Electronic Letters* **27**, 210–211 (1991).

[79] E. M. Dianov, P. V. Mamyshev, A. M. Prokhorov, and S. V. Chernikov, "Generation of a train of fundamental solitons at a high repetition rate in optical fibers," *Opt. Lett.* **14**, 1008–1010 (1989).

[80] P. V. Mamyshev, S. V. Chernikov, and E. M. Dianov, "Generation of fundamental soliton trains for high-bit-rate optical fiber communication lines," *IEEE J. Quant. Electron.* **27**, 2347–2355 (1991).

- [81] S. V. Chernikov, J. R. Taylor, P. V. Mamyshev, and E. M. Dianov, "Generation of soliton pulse train in optical fiber using two CW singlemode diode lasers," *Electron. Lett.* **28**, 931–932 (1992).
- [82] S. V. Chernikov, D. J. Richardson, R. I. Laming, E. M. Dianov, and D. N. Payne, "70 Gbit/s fiber based source of fundamental solitons at 1550 nm," *Electron. Lett.* **28**, 1210–1212 (1992).
- [83] E. A. Swanson and S. R. Chinn, "23-GHz and 123 GHz soliton pulse generation using two CW lasers and standard single-mode fiber," *IEEE Photon. Technol. Lett.*, vol. 6, no. 7, pp. 796–798, 1994.
- [84] E. A. Swanson, S. R. Chinn, K. Hall, K. A. Rauschenbach, R. S. Bondurant, and J. W. Miller, "100-GHz soliton pulse train generation using soliton compression of two phase side bands from a single DFB laser," *IEEE Photon. Technol. Lett.*, vol. 6, no. 10, pp. 1194–1196, 1994.
- [85] E. A. Swanson and S. R. Chinn, "40-GHz pulse train generation using soliton compression of a Mach-Zehnder modulator output," *IEEE Photon. Technol. Lett.*, vol. 7, no. 1, pp. 114–116, 1995.
- [86] S. V. Chernikov, J. R. Taylor, and R. Kashyap, "Integrated all optical fiber source of multi-gigahertz soliton pulse train," *Electron. Lett.* **29**, 1788–1789 (1993).
- [87] D. W. Anthon and T. J. Pier, "Diode-pumped erbium glass lasers," SPIE Vol. 1627 *Solid State Lasers III*, (1992).
- [88] A. M. Weiner *et al.*, *IEEE J. Quant. Elect.*, **25**, pp. 2648–2654, 1989.
- [89] A. M. Weiner *et al.*, *IEEE J. Quant. Elect.*, **28**, pp. 908–919, 1989.
- [90] R.-D. Li *et al.*, *IEEE Photon. Technol. Lett.*, **5**, pp. 669–672, 1993.
- [91] P.D. Townsend, *Electron. Lett.* **30**, 809 (1994).
- [92] H. P. Yuen, Proceedings of the Fourth International Conference on Squeezed States and Uncertainty Relations, NASA Conference Publication 3322, pp. 363- 368, 1996.
- [93] H.P. Yuen, "Quantum amplifiers, quantum duplicators, and quantum cryptography," to be published, *Journal of European Optical Society*, 1996.

## 6 List of Publications Resulting from this contract

1. J. P. Zhang, D. Y. Chu, S. L. Wu, S. T. Ho, W. G. Bi, C. Tu and R. Tiberio, 'Directional light output from micro-cavity semiconductor lasers', to be published in *IEEE Photonics Technology Lett.* in the issue of Aug. 1996.
2. J. P. Zhang, D. Y. Chu, S. L. Wu, S. T. Ho, R. Joseph, W. G. Bi, C. Tu and R. Tiberio, 'Nanofabrication of 1-D photonic-bandgap structure along photonic wire', *IEEE Photonics Technology Lett.* Vol. 8, No.4, pp.491-493, 1996.
3. S. T. Ho, D. Y. Chu, J. P. Zhang, S. L. Wu and M. K. Chin, 'Dielectric photonic wells and wires and spontaneous emission coupling factor of microdisk and photonic-wire semiconductor lasers', invited book chapter, published by World Scientific Publisher as Vol. 3 in the Advanced Serise in Applied Physics titled '*Optical Processes in Microcavities*', edited by Richard K. Chang and Anthony J. Campillo, Spring 1996.
4. J. P. Zhang, D. Y. Chu, S. L. Wu, S. T. Ho, W. G. Bi, C. Tu and R. Tiberio, 'Photonic-wire microcavity ring lasers' (invited article), *IEEE/LEOS Newsletter*, Vol.9, No.6, pp.7-8, Dec., 1995.
5. R. P. Espindola, M. K. Udo, D. Y. Chu, S. L. Wu, R. C. Tiberio, P. F. Chapman, D. Cohen, and S. T. Ho, "All-Optical Switching with Low-Peak Power in Microfabricated AlGaAs Waveguides," *IEEE Photon. Technol. Lett.*, vol. 7, 1995, pp. 641-643.
6. J. P. Zhang, D. Y. Chu, S. L. Wu, S. T. Ho, W. G. Bi, C. W. Tu, R. C. Tiberio, 'Photonic-wire lasers', To be published in *Phys. Rev. Lett.* Vol.75, No.14, pp.2678-2681, Oct. 1995.
7. R. P. Espindola, M. K. Udo, and S. T. Ho, "Nearly-Degenerate Frequency Technique for Simultaneous Measurement  $n^{(2)}$  and  $\alpha^{(2)}$ , and Four-Wave Mixing Gain Coefficients in Waveguides," *Opt. Comm.*, vol. 119, 1995, pp.682-692.
8. J. P. Zhang, D. Y. Chu, S. L. Wu, S. T. Ho, W. G. Bi, C. Tu and R. Tiberio, (Post deadline paper), *CLEO /QELS'95*, Bltimore, May 21-26, 1995.

9. M. G. Wang, J. P. Zhang, L. W. Wang, S. T. Ho, "Polarization-selective emission from quantum wells in a photonic wire with rectangular cross section", CLEO/QELS'96, QTHF7, Anaheim, California, June, 1996.
10. J. P. Zhang, D. Y. Chu, S. L. Wu, S. T. Ho, R. M. Joseph, A. Taflove, W. G. Bi, C. Tu and R. Tiberio, "1-D photonic bandgap structure along photonic wire", CLEO /QELS'96, CTHJ4, Anaheim, California, June, 1996.
11. H. P. Yuen, "High-rate strong-signal quantum cryptography," Proceedings of the Fourth International Conference on Squeezed States and Uncertainty Relations, NASA Conference Publication 3322, pp. 363- 368, 1996.
12. H.P. Yuen, "Quantum amplifiers, quantum duplicators, and quantum cryptography," to be published, Journal of European Optical Society, 1996.
13. R.-D. Li, P. Kumar and W. L. Kath, "Dispersion compensation with phase-sensitive amplifiers", J. of Lightwave Technol. **12**, 541-549 (1994).
14. C. G. Goedde, W. L. Kath, and P. Kumar, "Compensation of the soliton self-frequency shift with phase-sensitive amplifiers," Opt. Lett. **19**, 2077-2079 (1994).
15. C. G. Goedde, W. L. Kath, and P. Kumar, "Periodic amplification and conjugation of optical solitons," Opt. Lett. **20**, 1365-1367 (1995).
16. W. L. Kath, A. Mecozzi, P. Kumar, and C. G. Goedde, "Long-term storage of a soliton bit stream using phase-sensitive amplification: Effects of soliton-soliton interaction and quantum noise," submitted to *Optics Communications*.
17. G. D. Bartolini, D. K. Serkland, W. L. Kath, and P. Kumar "A Highly-Stable 60 GHz Soliton Source at 1550 nm," submitted to Photonics Technology Letters.
18. G. D. Bartolini, D. K. Serkland, P. Kumar, and W. L. Kath "All-optical storage of a picosecond-pulse packet using phase-sensitive amplification," to be submitted to Photonics Technology Letters.

## 7 List of Abbreviations

APM: Additive pulse mode-locked

CAIBE: Chemical assisted ion beam etching

DOPO: Degenerate optical parametric oscillator

EDFA: Erbium-doped fiber amplifier

GAWBS: Guided acoustic-wave Brillouin scattering

GVD: Group-velocity dispersion

LO: Local oscillator

OPO: Optical parametric oscillator

PECVD: Plasma enhanced chemical vapor deposition

PIA: Phase-insensitive amplifier

PNA: Photon-number amplifiers

PND: Photon-number duplicators

PMT: Photon multiplier tube

PSA: Phase-sensitive amplifiers

PZT: Piezo-electric transducer

RIE: Reactive ion etching

SEM: Scanning electron microscope

SPM: Self-phase modulation

TDM: Time-division multiplexing

WDM: Wave-division multiplexing

XPM: Cross-phase modulation

DISTRIBUTION LIST

addresses	number of copies
ROME LABORATORY/C3BC ATTN: ROBERT KAMINSKI 525 BROOKS ROAD ROME NEW YORK 13441-4505	5
DEPT OF ELEC & COMPUTER ENGINEERING NORTHWESTERN UNIVERSITY 2145 SHERIDAN ROAD EVANSTON, IL 60208	5
ROME LABORATORY/SUL TECHNICAL LIBRARY 26 ELECTRONIC PKY ROME NY 13441-4514	1
ATTENTION: DTIC-OGC DEFENSE TECHNICAL INFO CENTER 8725 JOHN J. KINGMAN ROAD, STE 0944 FT. BELVOIR, VA 22060-5218	2
ADVANCED RESEARCH PROJECTS AGENCY 3701 NORTH FAIRFAX DRIVE ARLINGTON VA 22203-1714	1
ATTN: RAYMOND TADROS GIDEP P.O. BOX 8000 CORONA CA 91718-8000	1
AFIT ACADEMIC LIBRARY/LDRE 2950 P STREET AREA B, BLDG 642 WRIGHT-PATTERSON AFB OH 45433-7765	1

ATTN: R.L. DENISON  
WRIGHT LABORATORY/MLPO, BLDG. 651  
3005 P STREET, STE 6  
WRIGHT-PATTERSON AFB OH 45433-7707

1

WRIGHT LABORATORY/MTM, BLDG 653  
2977 P STREET, STE 6  
WRIGHT-PATTERSON AFB OH 45433-7739

1

ATTN: GILBERT G. KUPERMAN  
AL/CFHI, BLDG. 248  
2255 H STREET  
WRIGHT-PATTERSON AFB OH 45433-7022

1

DL AL HSC/HRG, BLDG. 190  
2698 G STREET  
WRIGHT-PATTERSON AFB OH 45433-7604

1

AUL/LSAD  
600 CHENNAULT CIRCLE, BLDG. 1405  
MAXWELL AFB AL 36112-6424

1

US ARMY STRATEGIC DEFENSE COMMAND  
CSSD-IM-PA  
P.O. BOX 1500  
HUNTSVILLE AL 35807-3801

1

COMMANDING OFFICER  
NCCOSC RDT&E DIVISION  
ATTN: TECHNICAL LIBRARY, CODE 0274  
53560 HULL STREET  
SAN DIEGO CA 92152-5001

1

COMMANDER, TECHNICAL LIBRARY  
4747000/C0223  
NAVAIRWARCENWPNDIV  
1 ADMINISTRATION CIRCLE  
CHINA LAKE CA 93555-6001

1

SPACE & NAVAL WARFARE SYSTEMS  
COMMAND, EXECUTIVE DIRECTOR (CPD13A)  
ATTN: MR. CARL ANDRIANI  
2451 CRYSTAL DRIVE  
ARLINGTON VA 22245-5200

1

COMMANDER, SPACE & NAVAL WARFARE  
SYSTEMS COMMAND (CODE 32)  
2451 CRYSTAL DRIVE  
ARLINGTON VA 22245-5200

1

CDR, US ARMY MISSILE COMMAND  
RSIC, BLDG. 4484  
AMSMI-RD-CS-R, DOCS  
REDSTONE ARSENAL AL 35898-5241

2

ADVISORY GROUP ON ELECTRON DEVICES  
SUITE 500  
1745 JEFFERSON DAVIS HIGHWAY  
ARLINGTON VA 22202

1

REPORT COLLECTION, CIC-14  
MS P364  
LOS ALAMOS NATIONAL LABORATORY  
LOS ALAMOS NM 87545

1

AEDC LIBRARY  
TECHNICAL REPORTS FILE  
100 KINDEL DRIVE, SUITE C211  
ARNOLD AFB TN 37389-3211

1

COMMANDER  
USAISC  
ASHC-IMD-L, BLDG 61801  
FT HUACHUCA AZ 85613-5000

1

US DEPT OF TRANSPORTATION LIBRARY  
FB10A, M-457, RM 930  
800 INDEPENDENCE AVE, SW  
WASH DC 22591

1

AFIWC/MSO  
102 HALL BLVD, STE 315  
SAN ANTONIO TX 78243-7016

1

NSA/CSS  
K1  
FT MEADE MD 20755-6000

1

PHILLIPS LABORATORY  
PL/TL (LIBRARY)  
5 WRIGHT STREET  
HANSOM AFB MA 01731-3004

1

THE MITRE CORPORATION  
ATTN: E. LADURE  
D460  
202 BURLINGTON RD  
BEDFORD MA 01732

1

OUSD(CP)/DTSA/DUTD  
ATTN: PATRICK G. SULLIVAN, JR.  
400 ARMY NAVY DRIVE  
SUITE 300  
ARLINGTON VA 22202

2

**MISSION  
OF  
ROME LABORATORY**

**Mission.** The mission of Rome Laboratory is to advance the science and technologies of command, control, communications and intelligence and to transition them into systems to meet customer needs. To achieve this, Rome Lab:

- a. Conducts vigorous research, development and test programs in all applicable technologies;
- b. Transitions technology to current and future systems to improve operational capability, readiness, and supportability;
- c. Provides a full range of technical support to Air Force Material Command product centers and other Air Force organizations;
- d. Promotes transfer of technology to the private sector;
- e. Maintains leading edge technological expertise in the areas of surveillance, communications, command and control, intelligence, reliability science, electro-magnetic technology, photonics, signal processing, and computational science.

The thrust areas of technical competence include: Surveillance, Communications, Command and Control, Intelligence, Signal Processing, Computer Science and Technology, Electromagnetic Technology, Photonics and Reliability Sciences.